Mechanotransduction and Ion Transport of the Endothelial Glycocalyx: A Large-Scale Molecular Dynamics Study

Xizhuo Jiang

Department of Mechanical Engineering

Supervised by

Professor Kai Luo

Professor Yiannis Ventikos

A dissertation submitted in partial fulfilment

of the requirements for the degree of

Doctor of Philosophy

of

University College London

2018

Declaration

I, Xizhuo Jiang, confirm that the work presented in this thesis is my own. Where information has been derived from other sources, I confirm that this has been indicated in the work.

Signature:

Date:

Acknowledgements

I would like to show my gratitude to my dearest supervisor, Prof. Kai Luo, a fantastic advisor I could ever wish for, for his wisdom, support, enthusiasm and inspiration. I would have never made even a small step of progress in my research without his motivation and guidance. It has been a fabulous and amazing time to work together with him, from whom I get insights about science and life.

I also sincerely thank Prof. Yiannis Ventikos, the greatest supervisor, for his intelligence, passion and patience in conducting my research. The past three years witnesses how I grew up from a green hand in research to a PhD candidate under his supervision. It is really an honour to be a student of him.

My special thanks are to Prof. Haipeng Gong, who welcomed me to his research group in Tsinghua University, China. Without the invaluable visiting experience, I would not be capable of harnessing my “monster” system. I also appreciate helpful discussions and valuable input from Dr. Eduardo R. Cruz-Chu of ETH, Zurich, Dr Shunzhou Wan of University College London, and Dr. Wenzhi Mao, Dr. Meng Ke and Dr. Rui-Ning Sun of Tsinghua University.

Finally, I would like to acknowledge full support from a Dean’s Prize Scholarship from the Faculty of Engineering Sciences, University College London. The thesis was supported by the UK Engineering and Physical Sciences Research Council under the project UK Consortium on Mesoscale Engineering Sciences (UKCOMES) (Grants No. EP/L00030X/1 and No. EP/R029598/1).

Abstract

In our vessels, the endothelial glycocalyx is the first and foremost barrier directly exposed to the blood in the lumen. The functions of the normal endothelial glycocalyx under physiological conditions are widely accepted as a physical barrier to prevent the abnormal transportation of blood components (e.g. ions, proteins, albumin and etc.) and a mechanosensor and mechanotransducer to sense and transmit mechanical signals from the blood flow to cytoplasm.

In this study, a series of large-scale molecular dynamics simulations were undertaken to study atomic events of the endothelial glycocalyx layers interacting with flow. This research is a pioneer study in which flow in the physiologically relevant range is accomplished based on an atomistic model of the glycocalyx with the to-date and detailed structural information. The coupled dynamics of flow and endothelial glycocalyx show that the glycocalyx constituents swing and swirl when the flow passes by. The active motion of the glycocalyx, as a result, disturbs the flow by modifying the velocity distributions. The glycocalyx also controls the emergence of strong shear stresses. Moreover, flow regime on complex surface was proposed based on results from a series of cases with varying surface configurations and flow velocities.

Based on the dynamics of subdomains of the glycocalyx core protein, mechanism for mechanotransduction of the endothelial glycocalyx was established. The force from blood flow shear stress is

transmitted via a scissor-like motion alongside the bending of the core protein with an order of magnitude of 10~ 100 pN.

Finally, the mechanism of flow impact on ion transport was investigated and improved Starling principle was proposed. The flow modifies sugar chain conformations and transfers momentum to ions. The conformational changes of sugar chains then affect the Na^+/sugar-chain interactions. The effects of flow velocity on the interactions are non-linear. An estimation in accordance to the improved Starling principle suggests that a physiological flow changes the osmotic part of Na^+ transport by 8% compared with stationary transport.

Impact Statement

The study is interdisciplinary in nature, at the interfaces of engineering, life science and physics. It is of direct relevance to large research communities working on fluid dynamics, biofluids, soft matter, biomolecular surfaces, biomechanics, biophysics and healthcare technologies. Fluid dynamicists will would benefit from knowledge about flow behaviours over surfaces grafted with complex biomolecules, which will fill a gap in fluid mechanics. Biomedical scientists will benefit from insight into the detailed dynamic interactions between physiological flow and the endothelial glycocalyx, which is currently unavailable. Findings about the flow effects on ion transport and the dynamic response of the EG constituents would inspire clinicians and engineers to design therapeutic strategies and devices for a range of related diseases.

In the meantime, this study also has a significant importance to the nation. According to the latest statistics, cardiovascular disease, which endothelial glycocalyx is intimately related to, causes more than a quarter of all deaths — over 150,000 deaths in the UK each year (https://www.bhf.org.uk/statistics). Alzheimer's disease is also reported to be linked with the malfunction of the endothelial glycocalyx. The situation will become more critical as the UK enters deeper into an aging society. Accordingly, the Department of Health has given the highest priority to prevention and treatment of cardiovascular diseases in a recent national policy (NHS Outcomes Framework 2016-2017). The study in this thesis indeed contributes to such an effort.

As is known, new health products and services are a major component of the UK Industrial Strategy. The UK is recognised as a world leader in life and medical sciences and the sector contributes more than £50 billion to the economy. About 176,000 people are employed in over 5,000 companies. The therapeutic strategies and devices inspired from this study will proactively keep the UK staying in the leading position. Also, this research has the potential to benefit the sector within the 10-50 year timescale.

Table of Contents

Chapter 1

1 Introduction

1.1 Endothelial Glycocalyx (EG)

Material exchange between tissues and circulating blood plays an essential role in human metabolism. The exchange process mainly occurs across the endothelium, which is a delicate layer of endothelial cells (ECs) positioned in the vessel luminal surface exposed to the blood. The ECs constitute the skeleton of human vascular network, from capillaries with the smallest dimensions to the wide arteries of heart [1]. On the blood side of vascular EC surface, a network of proteoglycans and glycoproteins bound with the cell membranes serves as the primary and foremost barrier directly contacting with the flowing blood. The network is known as the glycocalyx [2, 3]. It has been proved that the endothelial glycocalyx layer (EGL) is responsible for a variety of illness and particularly renal and cardiovascular diseases, such as atherosclerosis [4, 5], ischemia/reperfusion [6], and diabetes [7]. For example, as shown in Figure 1-1, compared with the common arteries (shown in Figure 1-1a), the internal carotid arteries (shown in Figure 1-1b) are more likely to suffer atherosclerosis due to the reduction in endothelial glycocalyx thickness which facilitates the transport of protein to the subendothelial space [8, 9].

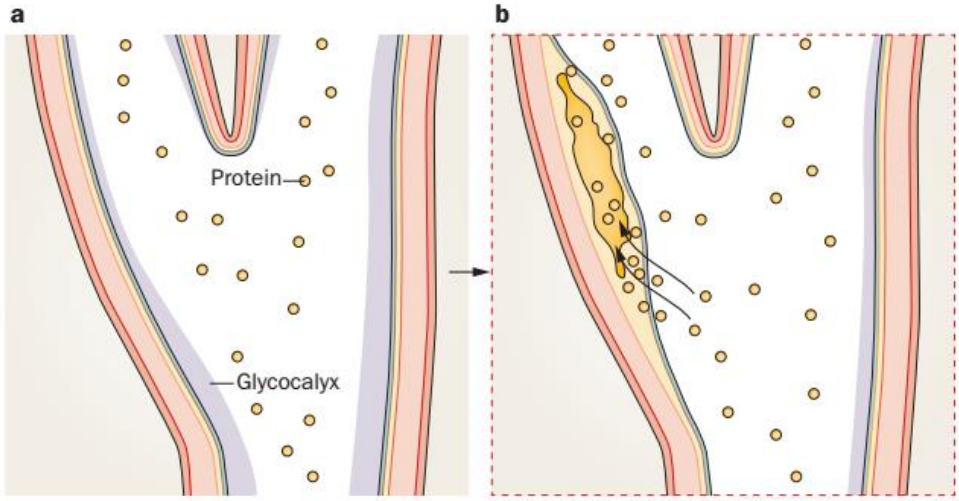

Figure 1-1 Schematic for the formation of atherosclerotic lesions due to the reduction in the endothelial glycocalyx thickness. a. In normal conditions, the endothelium (in blue) is coated with the glycocalyx, preventing the movement of proteins into the region beneath the EGL. b. After the shedding of the glycocalyx, proteins and other biomolecules can cross the EGL and enter the space beneath the EGL. The corresponding recruitment of inflammatory cells encourages the development of atherosclerotic lesions. [10]

Two key functions are attributed to the EGL: sieving materials [11-13] from the blood, and mechanotransduction [14-16] for the flow shear stress. It is considered a permeability modulator in the trans-capillary exchange of water and ions, creating local osmotic potential that is very different to the bulk of plasma in the capillary. Evidence also indicates that the EGL participates in regulating red and white blood cell interaction with the vascular lumen [17-19], most notably during inflammatory response. Finally, the EGL is also proposed to dominate the mechanism of flow shear stress sensing by the ECs. Initial mechanosensing by the primary sensory structure is followed by

signal transduction to the cytoskeleton of the cell, inducing biochemical responses as part of its self-regulation process [20].

The present of work mainly focuses on the understanding of the roles of endothelial glycocalyx as a vascular barrier for ion transport as well as a mechanotransducer.

1.2 Literature Review

Functions of biomolecules are determined by their structures or conformations. Therefore, structure and components of endothelial glycocalyx will be first reviewed as fundamentals. Based on the structural information, key functions of endothelial glycocalyx layers (i.e. mechanotransduction and sieving as vascular barrier) will then be summarised. Since computational methods will be employed in this research, multiscale modellings of endothelial glycocalyx layers will also be reviewed, followed by a brief introduction of molecular dynamics simulation which is the principle method used for this study.

1.2.1 Structures and Functions of EG

1.2.1.1 EG Constituents and Structures

In this section, the constituents of the glycocalyx will be outlined, and observation of the glycocalyx structure will be presented.

a. Glycocalyx Constituents

The endothelial glycocalyx, the layer rich in carbohydrate and locating on the vascular endothelium, is linked to the endothelium with the aid of its “backbone” molecules — proteoglycans.

Proteoglycans

Proteoglycans, comprising a core protein and at least one glycosaminoglycan (GAG) chain linked to the core protein, are widely accepted as the crucial “backbone” molecules of the glycocalyx. Proteoglycan core proteins vary in accordance to different aspects, such as size, the quantity of attached GAG chains, and their physical relationship with cell membranes (say, whether they are connected with the cell membrane or not). Syndecan is a typical core protein group. In its naming convention, a digital after the “Syndecan” indicates the numbers of heparan sulfate proteoglycans. However, the naming of such type of GAG is somewhat misleading, since the percentage of the sugar chains may vary with circumstances and stimuli [21]. For instance, according to the naming convention, the proteoglycan syndecan-1 is generally deemed to be connected with one GAG-chain (e.g. heparan sulfate). However in reality, both heparan sulfate and chondroitin sulfate chains with similar quantity can be observed in Syndecan-1 [22].

The GAG chains can be categorised into five types which individually have been extensively reviewed and investigated. The five types include heparan sulfate [23], dermatan sulfate, chondroitin sulfate [24], keratan sulfate [25], together with hyaluronic acid (or hyaluronan) [26]. The five types of GAG chains are polymers of disaccharides in linear forms, each consisted of a hexosamine and a uronic acid of variable lengths which can be modified by (de)acetylation and/or sulfation to a changeable extent. Therefore,

classification of the GAGs is determined by two factors: hexosamine or uronic acid incorporated and the sulfation pattern [4].

Heparan Sulfate

Heparan Sulfate (HS), an important member of the GAG family, consists of a variably sulphated duplicated disaccharide as shown in Figure 1-2. Some important features relevant to the biological activities of HS are listed in the following: (1) HS together with other sulfated GAGs are natural biopolymers featuring the highly negative charges, and enormous polydispersity in nature can be attributed to the diversity in the number and the chain lengths. (2) In some situations, only one GAG chain can be spotted in some proteoglycans (e.g. CD44), whereas others may have three to five chains attached (e.g., Syndecan). Some proteoglycans (e.g. syndecan-1), comprise both chondroitin/ dermatan sulfate (DS) and HS chains. (3) Both the number of the chains and sulfation state can change as response to the changing growth conditions and growth factors. (4) The sequence of the sulfate groups with negative charges and the orientation of the carboxyl groups determine where ligand-binding sites are located. In addition, the sulfated residues are usually in regionally clustered state along the chain with the mixed glucuronic acid and iduronic acid (i.e. NS domain in Figure 1-2), the chain is also interspersed with nonsulfated domains containing sufficient glucuronic acid (i.e. NA domain in Figure 1-2) to separate the sulfated residues. [27]

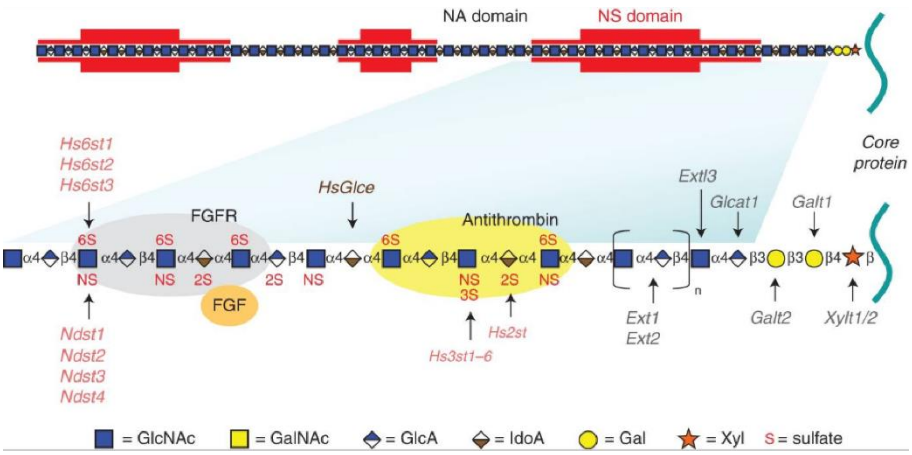

Figure 1-2 Heparan sulfate (HS) structure. [27, 28]

Syndecan-4

As multifunctional molecules, syndecans react to the extracellular matrix and signalling molecules with the aid of the GAG chains in the ectodomain [29]. The core protein syndecan family comprises four members: Syndecans 1 to 4. The expression of Syndecan-1 is predominantly on myeloma cells and epithelial cells, while both mesenchymal and endothelial cells facilitate the expression of syndecan-2. Syndecan-3 has been confirmed to be expressed in neural crest cells. By contrast, syndecan-4 is ubiquitously distributed [30].

Syndecan-4 (Syn-4), can serve as a collaborator with fibroblast growth factor receptors and participate in a variety of cellular processes as a key unit of the signalling pathways. It can also work as an independent unit activating signalling pathways upon ligand binding, thereby affecting migration, mechanotransduction, cellular proliferation and endocytosis [31]. Syndecan-4, due to the ubiquity in human body, will be further studied in this research and the signalling

pathways are summarised in Figure 1-3. Experiments also witness the indispensable role of Syn-4 in the alignment of ECs in the flow direction, as shown in Figure 1-4 [32].

b. Observation of Glycocalyx Structure

The high content in polysaccharide brings the endothelial glycocalyx a poor interaction with stains, like the widely adopted postfixation stains. Therefore, to visualise the glycocalyx in transmission electron microscopy (TEM), enhanced staining or improved preservation is necessary [33]. Luft used ruthenium red, or ammoniated ruthenium oxychloride to stain the aldehyde-fixed mucopolysaccharides and generated an electron-dense stain with the aid of osmium tetroxide [34]. In the realm electron microscopy, this is the first achievement in staining the glycocalyx.

Thereafter, the endothelial glycocalyx in the lumen has been subsequently observed via TEM based on numerous methods of staining and preservation. An effective approach is to colour the negatively charged sulfated GAGs. After colouring the GAGs, sharp electron-dense contrast with osmium tetroxide is produced, which facilitates the visualization [35-37]. A good stabilization of the carbohydrate structures usually means an impressive visualization of the glycocalyx. For instance, van den Berg *et al*. [38] used the alcian blue 8GX for staining. Their success in better stabilizing the anionic GAG structures in myocardial capillaries brings them an astounding image of endothelial glycocalyx with a thickness of up to 500 nm. Recently, Dane *et al.* [39, 40] used cupromeronic blue to visualise the renal glomerulus endothelial glycocalyx. On top of those, cationic

ferritin is also used in staining the negatively charged constituents of the EG. Figure 1-5 illustrates the examples of the widely used staining methods in the visualization of the endothelial glycocalyx.

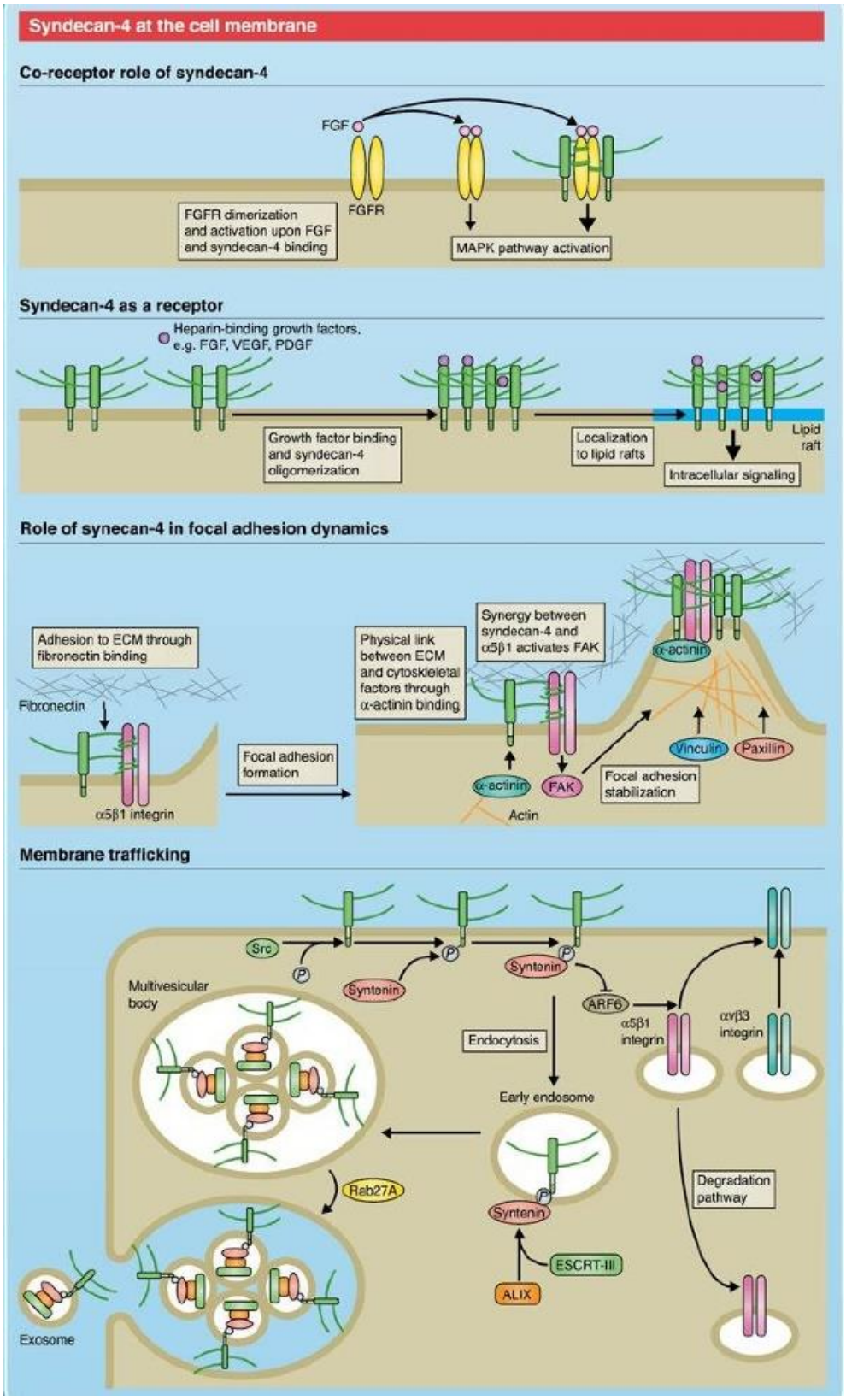

Figure 1-3 Summary of Syndecan-4 Signalling at the cell membrane[31].

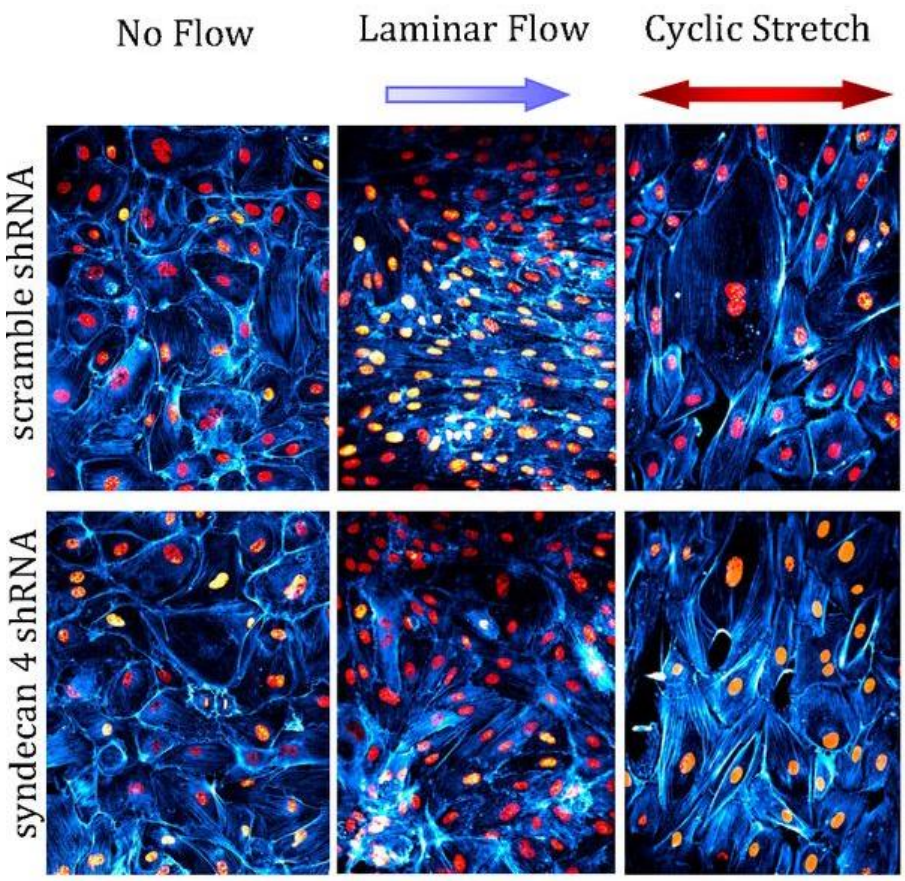

Figure 1-4 Syndecan-4 is an indispensable part in the endothelial cell polarity under flow shear stress. In the Syndecan-4 shRNA group, Syn-4 level is decreased by 65-80%, and cells failed to form the alignment in the flow direction. Cells were fixed and labelled in red and cyan colours [32]. (Please note that scale bars are not available from the original publication, but the figure can still support its conclusion.)

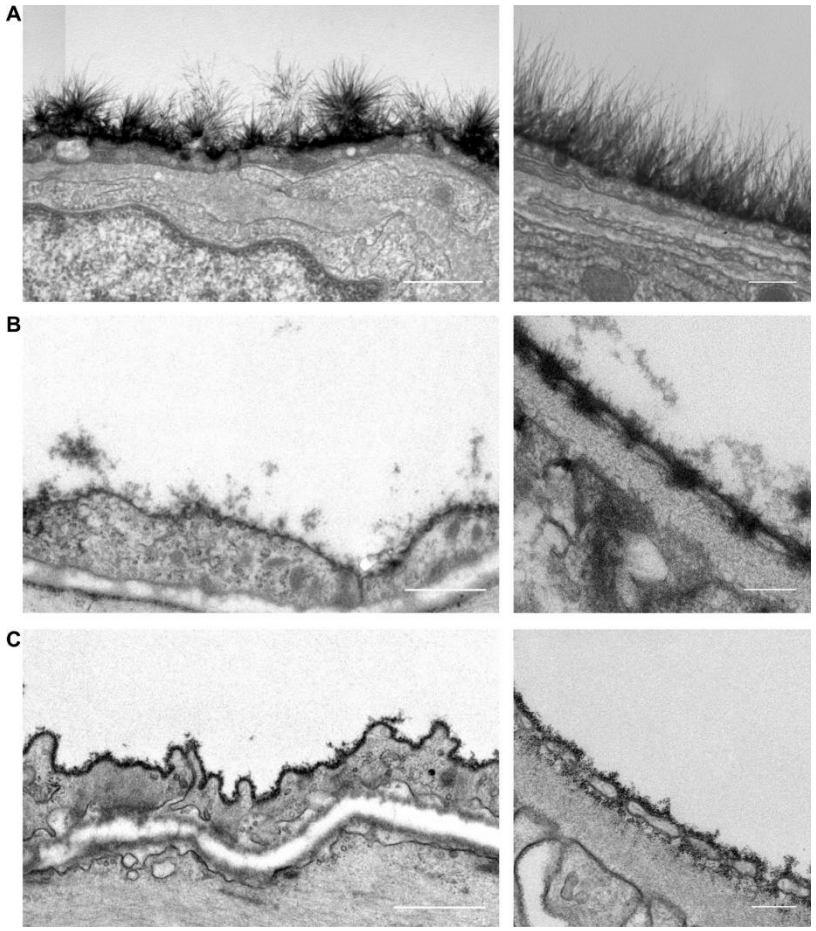

Figure 1-5 Three different stabilizing and staining methods in the visualisation of EG via electron microscopy. A. Left: Alcian blue 8GX is used to stain the acidic polysaccharides in the artery. Right: Locally enlarged image of a myocardial capillary stained by alcian blue 8GX. B. Left: Cupromeronic blue is used to stain the sulfated proteoglycans in vein. Right: Locally enlarged image of a capillary in glomerulus. C. Left: Cationic ferritin is used to stain the negatively charged constituents of the EG in vein. Right: Locally enlarged image of a capillary in glomerulus. Scale bars of the left and right panels are 500 nm and 200 nm, respectively. [40]

1.2.1.2 EG and Mechanotransduction

Mechanotransduction, defined as the modulation of biological fates by physical forces, has been ubiquitously found in every corner of the biological realm and with an extremely rich and diverse set of mechanisms [41-44]. A wide range of studies in the past decades has witnessed the emergence of several molecular participants that contribute to cellular mechanotransduction as summarised in Figure 1-6 [45].

Mechanism study of the endothelial glycocalyx mechanotransduction can be traced back to the beginning of the 21st century. The famous “bumper-car” model (in Figure 1-7) proposed two distinct cellular signalling pathways of the EG under fluid shear stress: the force from the flow shear stress load is conveyed by the core protein of glycocalyx via a torque acting on both the dense peripheral actin bands (DPAB) and the actin cortical web (ACW); the force can also stem from focal adhesions and stress fibres at the both the apical and basal sides of the cell membranes [46, 47]. Retrospect of early studies on mechanotransduction can be found in Tarbell’s review [48].

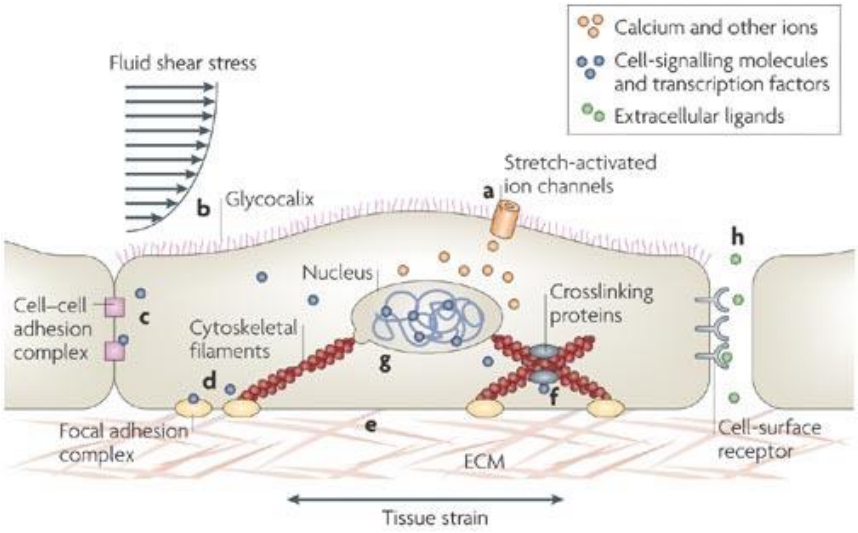

Figure 1-6 Cellular mechanotransduction [45]. a. Strain from membrane opens the stretch-activated ion channels in the lipid membrane, allowing the intake of Ca^{+} ions and other related ions [45]. b. In ECs, mechanotransduction signalling is modulated by the glycocalyx exposed to the fluid shear stress [45]. c. and d. Extracellular matrix–cell focal adhesions or intercellular junctional receptors facilitate cells to explore their surroundings [45]. e. Mechanotransduction signalling outside the cell can be stimulated by the unfolding of extracellular matrix proteins (e.g. fibronectin) by force [45]. f. Changes in conformations of crosslinkers, filaments, motor proteins and other cytoskeletal elements, caused by intracellular strain can change binding interplays with specific molecules and activate signalling pathways [45]. g. The nucleus per se is deemed to serve as a mechanosensor [45]. Intracellular deformations can lead to conformational changes in chromatin and control the access to transcriptional machinery or transcription factors [45]. However, further evidence for such a mechanism is still required [45]. h. Effective concentrations of paracrine and autocrine signalling molecules can be modified by the compression of the intercellular space [45].

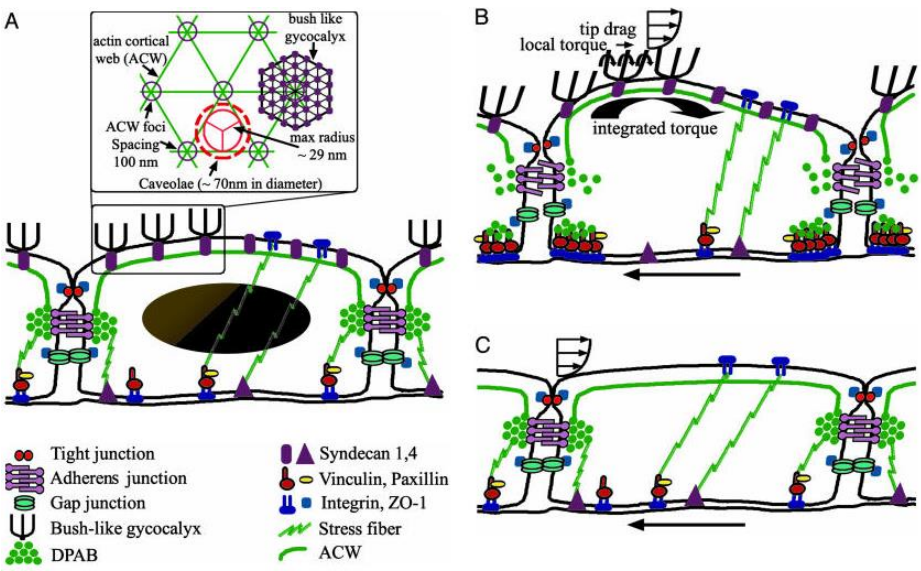

Figure 1-7 Schematic for the structural arrangement of the EC as a result to fluid shear stress load based on the bumper-car model. A. In the confluent stationary state, ECs have an intact DPAB residing in the adherens junction. The ACW is the supporting cortical scaffold for the overall apical cell surface. B. The intact endothelial glycocalyx of confluent ECs under fluid shear stress. C. The endothelial glycocalyx of confluent ECs compromised to fluid shear stress. [47]

The contributions of the EG constituents to mechanotransduction come into focus of the follow-on research. Most of the studies use enzyme degradation to remove a specific component (say HS) of the bio-macromolecule and determine the function of the component in mechanotransduction and related gene expression and signalling transmission [49-51]. For example, Dragovich *et al.* experimentally demonstrate the role of EGL as a sensor and transducer of vertical mechanical stretch in the production of nitric oxide (NO). Comparisons of NO production between cases those with intact EG structures and

those with the removal of HS and/or HA chains suggest that the existence of both HS and HA chains in EGL accelerates the production of NO. The generation of NO also relies on the influx of Ca^{2+} ions through endothelial channels [52]. To identify the importance of EGL in the adhesive affiliation between white blood cells and endothelial cells of human umbilical veins under resting or inflammatory conditions, the researchers used a direct method — a single-cell adhesion assay based on atomic force microscopy — to gauge the detachment force and work vertical to the cell membrane. Results demonstrate that the EGL layer serves a dual function: preventing adhesion of white blood cells on resting endothelium; and participating in interactions of the endothelial white blood cells with molecules (e.g. selectins) under inflammatory conditions [53]. The latter function is also proved in endothelial cells of human abdominal arteries under steady flow shear stress [54].

1.2.1.3 EG and Vascular Barrier

An intact EGL transduces fluid shear stress into the synthesis of endothelial NO, assists the endothelial barrier to fluid and protein, and regulates leukocyte-endothelial adhesion. The endothelial glycocalyx hinders the transcapillary leakage of macromolecules and water, serving as an integral and indispensable part of the multi-layered “fence” on microvessel walls [11].

Multilevel studies with respect to vascular permeability have been conducted. The aim of cellular-level studies is to articulate the mechanisms of common ECs for permeability, and to propose strategies for the restoration and maintenance of permeability in

inflammation or injury situations. Remarkable progress towards this aim has been made, especially regarding to the modulation of the paracellular pathway. The biomolecular constituents controlling channels of solutes, pathways of water molecules, and passage of inflammatory cells through the in-between junctions of the ECs have also been identified [55]. Figure 1-8a schematically summarises the major transport pathways in association with the endothelium with consideration of the connected tight junctions, vesicles, even breakings in the tight junctions, leaky junctions, and the glycocalyx as well. In Figure 1-8a, the glycocalyx is supposed to affect the permeability of water and solutes with sizes up to that of albumin via the breaks in the tight junctions by providing a transport hindrance to the entrance of the channels. For some big openings of the junctions, glycocalyx is unable to cover the leakage, thus, the additional resistance from the glycocalyx to this pathway is neglected. For small solutes which can pass through tight junctions, they are usually even smaller than the spaces between fibres in the EG; consequently, weak additional hindrance to transport is provided by the glycocalyx [56]. A model for transport barrier based on the known pathways highlighting the trans-vascular filtration of molecules by the endothelial layer is shown in Figure 1-8b [57].

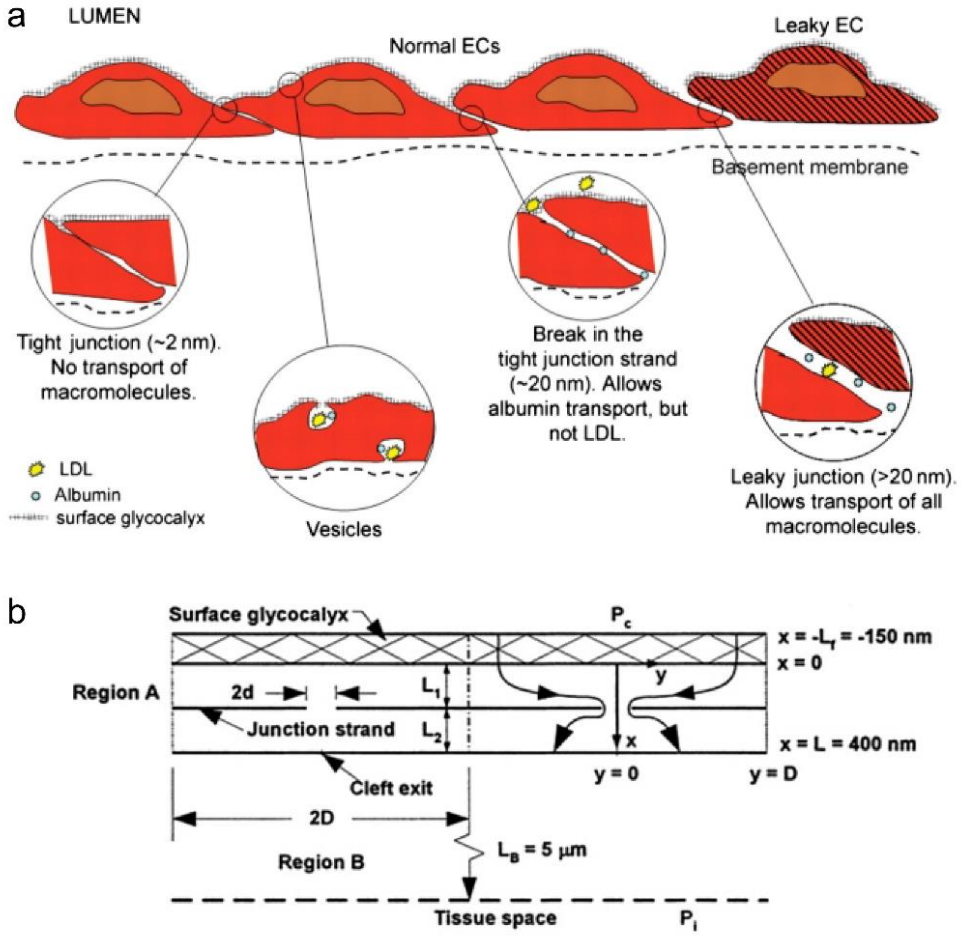

Figure 1-8 Pathways of transport across the endothelium and a model used for transport barrier. a. Major pathways of transport across the endothelium include the tight junctions, vesicles, breaks in between tight junctions, and leaky junctions. The glycocalyx covers the channel surface entrances can be covered by the glycocalyx, but not leaky junctions. [56] b. A model used for transport barrier considering junctions [57].

Starling Equation and Revision

Theoretically, the vascular barrier can be quantified by classic or revised Starling principle. The classic and revised Starling models are compared in Figure 1-9 [58]. Classic Starling model is illustrated in Figure 1-9A and follows the principle described in Eq. (1-1)

$$\frac{J_v}{A} = L_P\{\Delta P - \sigma\Delta\Pi\} \quad (1\text{-}1)$$

where J_v is the volume filtration rate per unit endothelial area A, L_P is the membrane hydraulic conductivity, σ is the osmotic reflection coefficient, ΔP is hydrostatic pressure difference, and $\Delta\Pi$ is osmotic pressure difference across the membrane [58]. A variety of solutes are contained in plasma and interstitial fluid. Thus, the movement of fluid acrossing the intervening capillary wall based on Eq. (1-1) can be further written as:

$$\frac{J_v}{A} = L_P\{\Delta P - \sum \sigma_n \Delta\Pi_n\} \quad (1\text{-}2)$$

where n is the varieties of solute species, and $\Sigma\sigma_n\Delta\Pi_n$ is the aggregated osmotic pressure differences across the vessel walls from all the solutes in plasma and interstitial fluid [58]. In most microvascular situations, osmotic reflection coefficients (σ) for small solutes are no larger than 0.1, and usually the macromolecular solutes have significant concentration differences. Therefore, under these circumstances, Eq. (1-2) can be further refined as Eq. (1-3).

$$\frac{J_v}{A} = L_P\left[(P_c - P_i) - \sigma(\Pi_P - \Pi_i)\right] \quad (1\text{-}3)$$

where ΔP in Eqs. (1-1) and (1-2) is calculated by the difference between the blood pressure P_c and interstitial fluid hydrostatic pressure P_i, and the osmotic term in Eq. (1-1) or (1-2) is simplified using the difference between the effective osmotic pressure from macromolecules in plasma (Π_P) and interstitial fluid (Π_i).

However, as reviewed in Ref. [58], the conventional model illustrated in Figure 1-9A fails to predict fluid exchange in actual microcirculation situations, due to the following reasons: a) The changes in J_v will result in the variations of both P_i and Π_i change in Eq. (1-3); and b) a different composition to bulk interstitial fluid is generated due to the structure of the semipermeable membrane (the sub-glycocalyx fluid). In this context, a revised Starling principle was proposed as in Figure 1-9B. Particularly, the filtration force (FF) has been revised as:

$$\mathrm{FF} = \Delta P - \sigma(\Pi_p - \Pi_g) \tag{1-4}$$

In Eq. (1-4), the osmotic part of the filtration force is calculated by the differences in osmotic pressures between both sides of the EGL.

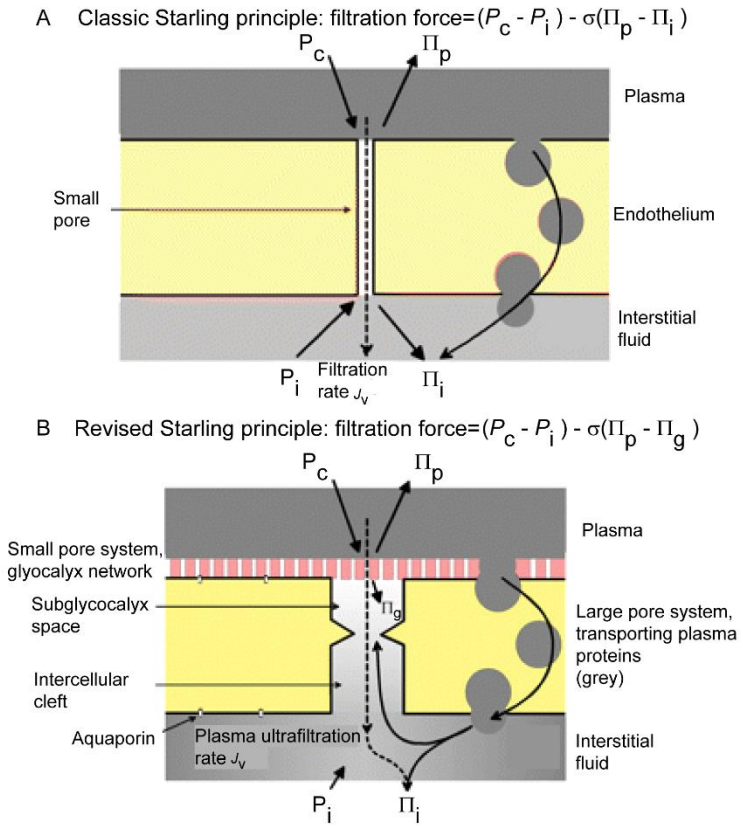

Figure 1-9 Comparison between classical and revised perspectives of semipermeability of the endothelial membrane and the corresponding filtration forces. (A) Continuous endothelium as a semipermeable membrane in the view of classical Starling principle. (B) In the revised perspective, glycocalyx is identified as a semipermeable layer in the glycocalyx–cleft model. [58]

The revised Starling principle serves as an effective method to estimate the permeability of the EGL and provides a unique view to understand solute behaviour under the EGL [59-61]. However, when the microvascular environment is changed (e.g. changing blood velocity or changes in sugar chain configurations), even this revised principle seems to be incapable of predicting the response of solute

transport. Therefore, further efforts are still needed to improve the Starling principle.

It is also worthwhile to mention some additional models alongside experimental data for a complete view of the solute transport theory. For example, theoretically, Ogston's 1958 equation [62] quantified the distribution of permeation into gels in relation with molecular size in a random network of straight fibres situation. And a typical scenario of this situation is proteins within the glycocalyx. Experimentally, the sodium permeability can be altered by the introduction of external substance, like herb. Peters *et al*. investigated the influence of a type of herbal remedy — the hawthorn extract WS 1442 — on the permeability of Na^+ on endothelial cell monolayer. Despite the pertinent mechanism is still unclear, the data indicate that the endothelial surface layer accounts for around 11% of the overall endothelial barrier hindrance for Na^+; beside, WS 1442 fortifies the EGL hindrance for Na^+ by approximately 45% [63].

Macromolecular permeation into the basement membrane of renal glomerulus is also experimentally studied. Lawrence *et al*. concluded the success of macromolecules in reaching in urine can be attributed to two aspects: a) size-based permeation both into the glomerular basement membrane and into a gel-like coat covering the slits; and b) tubular reabsorption in saturable states. Their findings challenge a conventional view that the primary filtration of protein is low as fluid departing the glomerulus travels through slits spanned by a diaphragm serving as a molecular sieve with a low-porosity [64].

1.2.2 Multiscale Modellings of EG

Multiscale modelling studies, from continuum of the macroscale via dissipative particle dynamics (DPD) or coarse-graining method of the mesoscale/microscale to molecular dynamics (MD) of microscale/nanoscale, of endothelial glycocalyx have been conducted to theoretically or numerically predict the biomolecular behaviour in past decades. In this research, a few representative studies related to EGL are reviewed.

1.2.2.1 Continuum Models

In the early theoretical models, the glycocalyx and membrane were assumed to be rigid and immobile [46, 47], a hypothesis that is clearly too restrictive for this system. However, some new insights can still be obtained from the simple models. For example, Tarbell and Shi developed a simplified fluid model in which the glycocalyx layer implanted in an extracellular matrix is regarded as a uniform region with certain fluid properties. To estimate the force transmitted from the fluid to the cell surface, flow profiles of the extracellular matrix and the glycocalyx layer were calculated by the Brinkman equations. They also determined the solid mechanical stress via the glycocalyx stemming from the loading of fluid flow shear stress. Results have shown that the solid cell surface stress is about 10 to 100 times larger than the fluid shear stress in terms of order of magnitude. The significantly enhanced stress of the cell surface suggests that the cell surface glycocalyx can sense the flow shear stress, which provides theoretical support for plenty of relevant experimental observations about the

function of the glycocalyx as a mechanotransducer of the flow shear stress [65].

Follow-on studies incorporate more complicated models which emphasize the rheology of the cytoskeleton network [66-68]. For example, Dahagh *et al*. [68] developed a multi-component, multi-scale, and three-dimensional viscoelastic model of focally adhered endothelial cells, and applied oscillatory wall shear stress in the parallel direction as the mainstream flow, or multi-directional oscillatory wall shear stress with reversing transverse and axial components over the endothelial surfaces (Figure 1-10 a and b). The computational model contains the glycocalyx layer, stress fibres, adherens junctions, focal adhesions, actin cortical layer, cytoskeleton, and nucleus. Results indicate that stresses and strains can be weakened by the reversing flow (Figure 1-10 c to f), and forces on integrins and adherens junctions related to mechanotransduction are also predicted.

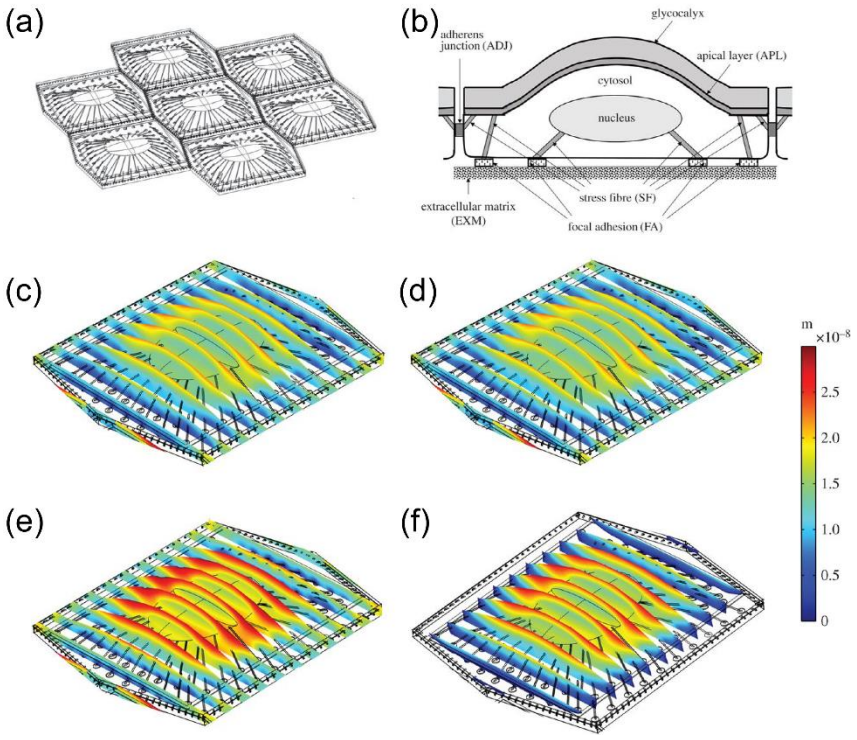

Figure 1-10 Comprehensive model of endothelial cells by Dahagh *et al*. [68] and computational results. (a) Geometric arrangement of inter-/intracellular organelles and EC monolayer. (b) Side view of EC, with surrounding cells and pertinent subcellular structures in the neighbourhood. (c)-(f). Displacement of the EC monolayer under different set-ups of flow shear stresses. (c) EC exposed to disturbed flow in multi-directions. (d) EC exposed to pulsatile and reversal flow. (e) EC exposed to pulsatile but no-reversal flow. (f) EC exposed to steady flow.

1.2.2.2 Coarse-Grained Models

Among coarse-grained methods, dissipative particle dynamics (DPD) method aims to tackle complex fluids problems at mesoscale (e.g. blood [69-71]) and soft matter (e.g. polymer [72-75]). In DPD method, the system is treated as an ensemble of coarse-grained portions (i.e. DPD particles). Therefore, DPD models allow longer and

larger-scale simulations compared with microscopic simulations [76], such as atomistic models which will be mentioned later.

Deng *et al.* [77] conducted DPD simulations to investigate both glycocalyx filaments and polymer brushes in response to shear flow. In their simulation, mean-field theory was practised to analyse the scaling variables. Results showed that the glycocalyx fibres, whose flexural rigidity was assumed finite when simulated by a semi-flexible polymer model, provide stronger resistance to the flow than their polymer counterparts, whose flexural rigidity was assumed zero when mimicked by a flexible polymer model. Additionally, they simulated the scenario where blood flows through a small tube with a diameter of 10 microns and the tube surface is coated with a layer of glycocalyx fibres. The authors calculated the Newtonian fluid dynamics of neutrally buoyant, monodisperse, deformable red blood cells (RBCs), which are key component of the blood. Results suggest a cell free layer was formed as the RCBs migrated towards the tube centre (as shown in Figure 1-11) and there was no direct contact between the RCB and the EGL.

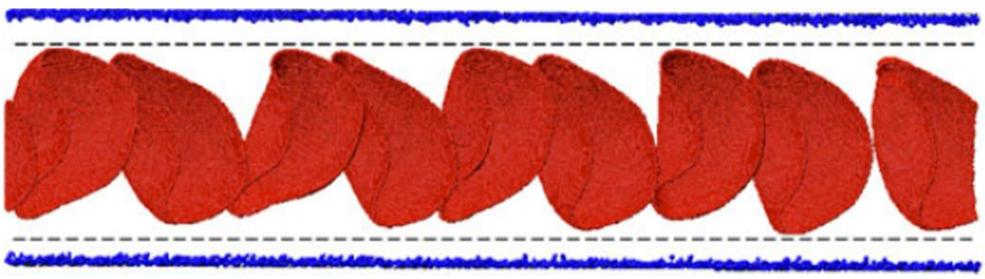

Figure 1-11 Modelling of the scenario where blood flows through a tube using the DPD method by Deng *et al.* Red blood cells (shown in red) are deformable. The glycocalyx fibres are illustrated in blue; the border of the cell-free layer is represented by dashed lines [77].

Coarse-grained models are also used in microsecond-scale simulations of sugar chains. Sattelle *et al.* performed a series of dynamics simulations of eleven heparanome oligosaccharides at time scale of microsecond to discuss the impact of residue sequence on spatial structure. These results provide statistical support for a coarse-grained model (containing 800 residues, shown in Figure 1-12) that is in consistency with experimental findings about the atomic dynamics in water at a long-time scale. The authors also indicate that, 3D-shape of polymers, puckering, and bioactivity are intimately connected in the heparanome [78].

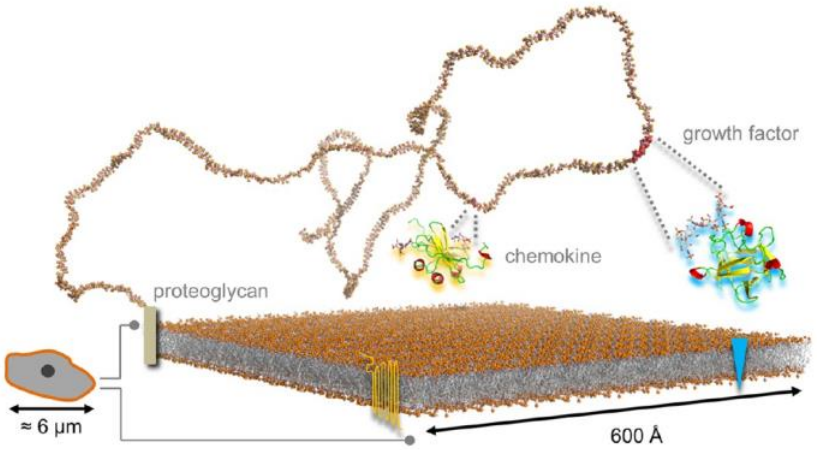

Figure 1-12 Schematic for a minuscule extracellular environment in mammalian. It includes a small patch of the lipid bilayer, proteins with an HS chain comprising 800 residues, basic fibroblast growth factor and a chemokine. The snapshot is rendered from coarse-grained simulation at a time scale of microsecond. [78]

1.2.2.3 Atomistic Models and Beyond

Due to comprehensive reasons, such as high computation expense and the lack of detailed structural information of glycocalyx, a plethora of atomistic models involving glycocalyx only focus on the

behaviour of sugar chains with simplified models [79-81]. For example, Eriksson *et al*. [79] conducted classical molecular dynamics simulations to investigate properties of simple cations solvated in water based on explicit-solvent models surrounded by sole and manifold oligosaccharides (in Figure 1-13), as a simplification of the glycocalyx. They found that the oligosaccharides of their interest tent to contact K^+ more frequently than Na^+ but the contact with Na^+ lasts longer. These interactions, in the meantime, result in strong but short-instant conformational changes of oligosaccharides. These findings may contribute to the current understandings in glycocalyx functions as molecular sieves.

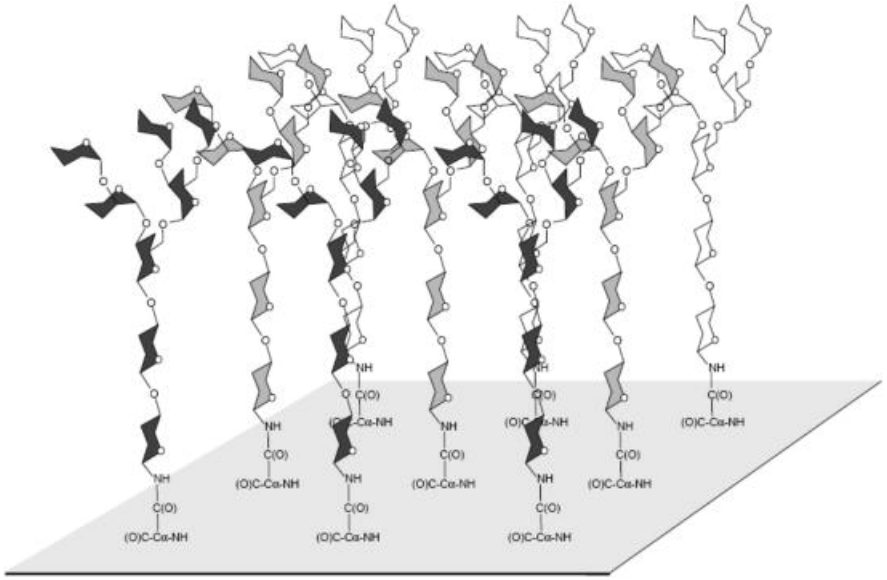

Figure 1-13 Schematic of oligosaccharide array investigated in a previous study [79].

With the development of force field parameters, a growing number of studies are zooming in the fine components of the sugar chains (e.g. liner, residue and binding site) [82-85], providing implications for

material or artificial synthesis [86, 87]. Ng *et al.*, studied the conformational preferences of the tetrasaccharide linker (i.e. GlcAb1-3Galb1-3Galb1-4Xylb1-O-Ser) between the core protein and glycosaminoglycans (HS chains in this study) using all-atom molecular dynamics and the application of adaptive biasing force sampling with water molecules simulated by the explicit-solvent model. Results indicate that the tetrasaccharide acts as a relatively rigid unit whereas significant conformational heterogeneity exists with respect to rotation about bonds connecting Xyl to Ser [85].

The pursuit of minuscule and subtle events inside the EGL promotes the application of the hybrid method of quantum mechanics and molecular modelling to glycocalyx related research. Sousa *et al*. [88] presented the reaction mechanism of HS and a special enzyme through quantum mechanics/molecular mechanics calculations, and this study provides novel insights into the inhibition of the specific enzyme.

The first most detailed atomic model of glycocalyx was published in 2014 by Cruz-Chu [89]. In the model, an updated fully atomistic model of the EG, alongside dimers of proteoglycan, a lipid bilayer patch, and HS chains arranged in realistic sequences was constructed (as shown in Figure 1-14). The authors also studied glycocalyx behaviour under flow shear stress and concluded that the glycocalyx transfers mechanical stimulus into endothelial cell cytoplasm in the manner of a lever. However, the flow regime implemented in this research is highly unrealistic with bulk flow velocity being 10 m/s (Detailed analysis are mentioned in Appendix A), therefore, their

conclusion about the role of the glycocalyx as lever in mechanotransduction is questionable.

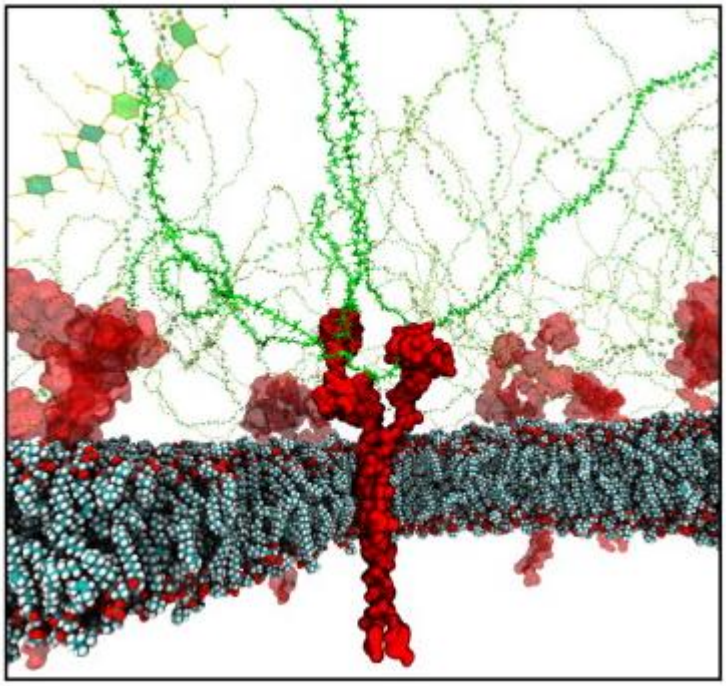

Figure 1-14 A to-date atomistic glycocalyx model [89]. Sugar chains are represented by green licorice. Transmembrane protein represented by red beads; Lipid bilayer is interspersed with white, cyen and red small beads. Ions and water molecules are not shown.

To mimic a physiological flow, an oligosaccharide model of the vascular EG was used with external forces imposed on the water oxygens [90]. The interplay between the flow and glycan has been spotted. As shown in Figure 1-15, along the length of the glycan's range of movement, the velocity begins to drop, particularly as the shape of the molecule becomes increasingly dendritic. In the meantime, the glycan has also been stretched by the flow, resulting in a length increase of the glycan.

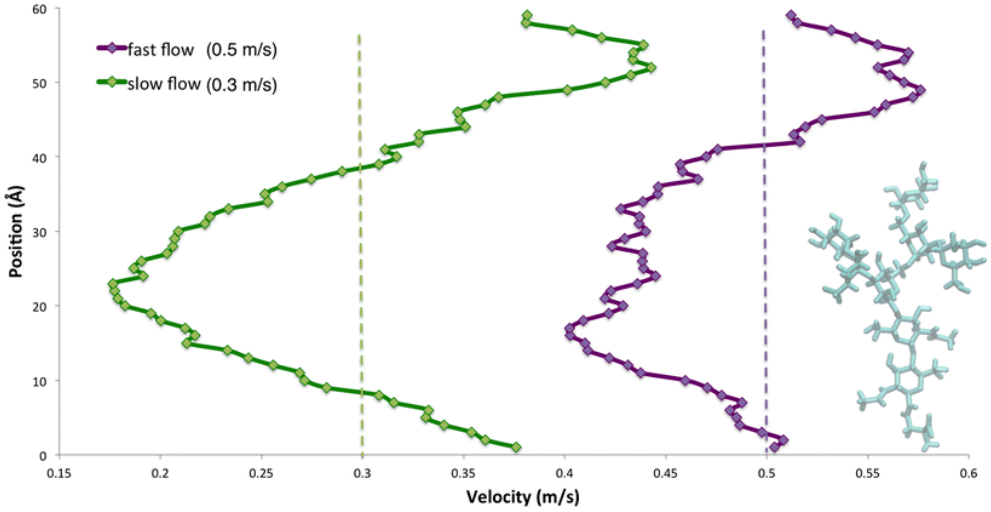

Figure 1-15 Velocity profiles across the height direction of the oligosaccharide. [90] Along the length of the glycan's range of movement, the velocity begins to drop, particularly as the shape of the molecule becomes increasingly dendritic. The length of the glycan, in the meantime, has been stretched as the flow passes by.

1.2.3 Molecular Dynamics Simulation

1.2.3.1 The Idea of Molecular Dynamics

Molecular Dynamics (MD) simulation is a method to calculate an equilibrium state and physical properties of a system with many-body features. In classic many-body system, the motion of the constituent particle nuclear follows classical mechanics laws. MD simulations are in many respects like wet experiments in the real world. A sample of the material, in a real experiment, is related to a measuring instrument, and property that the researchers are interested in is measured during a certain period. Usually, statistical noises are generated in the measurement. To diminish the effects of noises, averaging of the quantity over time is conducted. Generally, a longer-time averaging

will benefit the generation of more accurate results. In a MD simulation, the same approach is used. At the very beginning, a system to be modelled comprising a certain number of particles is selected, and solutions to Newton's equations of motion specifically for the designed system are being undertaken till some indexes representing the system properties go to stable. After equilibration, the actual measurement is performed. To quantify an observable parameter in an MD simulation, statistical mechanics is needed to establish relation between the microscopic and macroscopic worlds. Fundamentals about MD simulation can be referred to books [91, 92] and a review for the application of MD simulations to biomolecules in the first 25 years was conducted by Karplus *et al*. [93].

1.2.3.2 Classical Molecular Dynamics

In MD simulations, the atomic and molecular trajectories are solved by Newton's equations of motion for individual particles in a specific system. The force term of Newton's equation is usually solved by calculating the potential energies between particles. In the computation of the potential energies, molecular mechanics force fields or interatomic potentials are used. The basic form of potential energy in MD simulations is composed of two parts: bonded terms, which describes the interactions of linked atoms via covalent bonds; and nonbonded terms describing van der Waals (vdW) and electrostatic forces featuring a long range. Accordingly, the potential energy of a particle can be expressed as

$$E_{total} = E_{bond} + E_{angle} + E_{dihedral} + E_{vdW} + E_{electrostatic} \quad (1\text{-}5)$$

In Eq. (1-5), the first three right-hand side terms are the three components of the interactions regarding bonds, and the long-range interactions are calculated by the last two terms.

To calculate individual terms of the right-hand side, models have been developed. Quadratic energy functions are usually used to model the bond and angle terms. For example, in the calculation of bond length, the most simplified model is to use a Hooke's law in the form of Eq. (1-6).

$$v(l) = \frac{1}{2} k(l - l_0)^2 \tag{1-6}$$

In which k represents the force constant, l is the length of bond and l_0 is the bond length at a special situation where the remaining terms are set to 0 in the force field.

For the nonbonded terms, a Lennard-Jones potential is widely applied to calculate the vdW term, and Coulomb's law is used to compute the electrostatic term.

Figure 1-16 summarises the typical examples for potential terms as used in common force fields.

6-9 van der Waals 6-12 van der Waals Electrostatic	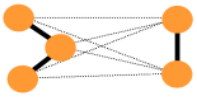	$u_{ij}(r_{ij}) = 4\varepsilon_{ij}\left(\left(\frac{\sigma_{ij}}{r_{ij}}\right)^{9} - \left(\frac{\sigma_{ij}}{r_{ij}}\right)^{6}\right)$ $u_{ij}(r_{ij}) = 4\varepsilon_{ij}\left(\left(\frac{\sigma_{ij}}{r_{ij}}\right)^{12} - \left(\frac{\sigma_{ij}}{r_{ij}}\right)^{6}\right)$ $u_{ij}(r_{ij}) = \frac{q_i q_j}{r_{ij}}$
Quadratic bond-stretching Morse bond-stretching	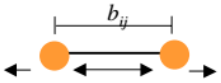	$u_{ij}^{s}(r_{ij}) = \frac{1}{2}k_{ij}(r_{ij} - b_{ij})^2$ $u_{ij}(r_{ij}) = k\left(1 - e^{-a(r_{ij} - r_0)}\right)^2$
Bond-bending		$u_{ij}^{b}(\vartheta_{ijk}) = \frac{1}{2}k_{ijk}(\vartheta_{ijk} - \vartheta_{ijk}^{0})^2$
Improper dihedrals		$u_{ij}^{id}(\xi_{ijkl}) = \frac{1}{2}k_{ijkl}(\xi_{ijkl} - \xi_0)^2$
Proper dihedrals	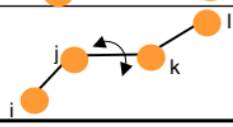	$u_{ij}^{pd}(\varphi_{ijkl}) = k_{\varphi}\left(1 + \cos(n\varphi_{ijkl} - \varphi_0)\right)$

Figure 1-16 Typical examples for potential terms as used in common force-fields. [94]

Particularly, a general form of the force field applied in this study—the CHARMM force field [95] is written as

$$E_{\text{total}} = \sum_{\text{bonds}} k_b\left(b - b_0\right)^2 + \sum_{\text{angles}} k_\theta\left(\theta - \theta_0\right)^2 + \sum_{\text{dihedrals}} k_\phi\left[1 + \cos\left(n\phi - \delta\right)\right]$$
$$+ \sum_{\text{impropers}} k_w\left(w - w_0\right)^2 + \sum_{\text{Urey-Bradley}} k_u\left(u - u_0\right)^2$$
$$+ \sum_{\text{nonbonded}} \varepsilon\left[\left(\frac{R_{\min_{i,j}}}{r_{i,j}}\right)^{12} - \left(\frac{R_{\min_{i,j}}}{r_{i,j}}\right)^{6}\right] + \frac{q_i q_j}{\sigma r_{i,j}} \tag{1-7}$$

In Eq. (1-7), the first two terms account for the bond stretches and bond angles. In the dihedral term, k_Φ is the constant for dihedral force, n is the function multiplicity, and δ represents the phase shift with Φ for the dihedral angle. The improper term calculates the out of plane bending with a force constant k_w and an out of plane angle (w - w_0). The Urey-Brandley term is introduced to circumvent the difficult

situations where force constants prevail over the observed normal vibrations in quantities, especially in the calculations of complex molecules. The Urey-Bradley force field includes force constants for stretching and bending, alongside constants for repulsive forces between nonbonded atoms [96]. Normally, the generalized valence force has greater force constants than that of the Urey-Bradley force field [96]. For an atom pair (i, j) with a distance of $r_{i,j}$, nonbonded (i.e. long-range) interactions between both atoms are calculated by the last two terms. A 12-6 Lennard-Jones potential is adopted to work out the vdW energy; and Coulomb's potential is used to solve the electrostatic term. $R_{\min i,j}$ is the position of the x-axis intercept of the Lennard-Jones potential (i.e. zero-potential).

Ensembles, artificial constructs in MD simulations, generate averages that are in consistency with one another when representing one identical state of a system. For example, in the canonical ensemble, also referred to as the constant-temperature, constant-volume ensemble (NVT), constant temperature is accomplished by the following two procedures. In the initialization stage, the temperature is controlled via direct scaling; and in the data collection stage, the temperature is maintained via temperature-bath coupling. The number of atoms and the system volume are kept constant throughout the run. Other ensembles include the constant-energy, constant-volume ensemble (NVE) and the constant-temperature, constant-pressure ensemble (NPT), and so on. The relation between different ensembles and their transformation has been deeply discussed by Allen and Tildesley [97].

1.2.3.3 Computational Considerations

In the construction of MD simulations, some critical factors need to be considered. Among them, a proper algorithm of realizing an ensemble is an essential part for a successful MD simulation.

As described previously, a “thermostat” coupling the system to an external heat bath is required to maintain a specific temperature in MD simulations [98]. The problem — how much does an algorithm for thermostat affect the MD outputs — remains unanswered [98]. However, there are evidences indicating that the system performs distinguished dynamics when the thermostat algorithm changes. The conclusion is valid for the microcanonical ensemble [98]. And the main differences of the algorithms reside in the way how they deal with molecule diffusion and rotational motions [99, 100]. Generally, dynamic properties generated from one algorithm is distinguished from those from anther algorithm [100, 101], as every algorithm deals with velocities of particles in different ways [98]. Take a non-equilibrium MD situation (e.g. flow) as an example. The Berendsen thermostat [102] was prevailing in previous MD studies of non-equilibrium systems [103-105] (like flow). In Berendsen thermostat, to maintain the temperature of the system at a certain constant value, the particle velocities are re-scaled [98]. However, recent studies have reported that the application of the Berendsen thermostat would generate an article force to decelerate the flow velocity due to the re-scaling of velocities [98]. Instead, a Lowe-Anderson thermostat [106], a Galilean invariant thermostat to ensure the conservation of momentum, can generate more reliable results than the Berendsen method in

nonequilibrium simulations [107], particularly for simulations involving flow [98].

Periodic boundary conditions (PBCs) are practised in a wide range of MD simulations on the base that the quantity of molecules in the system is conserved. However, for most real situations, the system of interest is not isolated and must interact with external environment. In other words, exchanges of mass, momentum and energy between the system and its environment should be considered. In this circumstance, open boundary is needed and should be proposed. A detailed retrospect of the open boundary can be found in Ref. [108].

1.2.4 Summary of Literature Review

Significant contributions to the knowledge of glycocalyx and related pathologies have been made in the past decades with the aid of theoretic and experimental methods. However, successive efforts are still required for uncovering the mysteries inside the endothelial glycocalyx layer.

As reviewed previously, in the theoretical studies of mechanotransduction of the EG, the glycocalyx and membrane were assumed to be rigid and immobile, a hypothesis that is clearly too restrictive for this system. Follow-on studies improved the results by incorporating more complicated models concentrating on exploring the rheology of the network of cytoskeleton; however the glycocalyx was still treated as rigid especially for its transmembrane part. Theoretical analysis can, to some extent, predict force transmission pathways; however, the neglection of the detailed dynamics of the glycocalyx can also result in failure in revealing mechanisms in a comprehensive

manner. In experiments, enzyme degradation studies are efficient in recognising specific functions of biomolecules, but they also have limitations. For example, as stated in a previous review [109], in the study of EC surface functional proteoglycans, enzyme degradation studies may result in inaccurate estimation of contribution of individual glycocalyx constituents to mechanotransduction. Meanwhile, the highly dynamic and fragile structure of the glycocalyx can cause instability when endothelial cells are taken out of their *in vivo* environment [40], which may result in untrustworthy conclusions.

Because of the high computational expense, the current MD simulations in biophysics are mainly dealing with systems with less than 1 million atoms and length scale smaller than 1 nm. The endothelial glycocalyx layer, usually of 50 nm to 500 nm height, is undoubtedly a “monster” for current MD simulations. Even so, the arrival of the glycocalyx structural information still provides possibility to uncover the secrets behind the EGL. Indeed, the advent of exascale computing machines, together with molecular dynamics with detailed structural information will be a powerful tool to unveil the atomic events inside the EGL.

The Starling principle and its revision are effective in estimating the permeability of the EGL particularly for stationary states. However, they fail to clarify the response of ion transport to the changes in environmental factors, like the shedding of sugar chains and the varying blood flow velocities. In this regard, mechanism for the influence of flow and sugar chain configuration on the ion transport is

still worth exploration. Accordingly, an improved Starling principle is also expected.

1.3 Aims and Objectives

Based on the summary of literature review, this research aims at using molecular dynamics method to unveil the mechanisms for critical functions of the EG from the atomic perspective and to provide new insights into the pathologies. After a proactive investigation, the focus of this study will be a small patch from the endothelial cell surface but with essential elements of the EG. Figure 1-17 provides an overview of the length scale of the patch which will be investigated in this study.

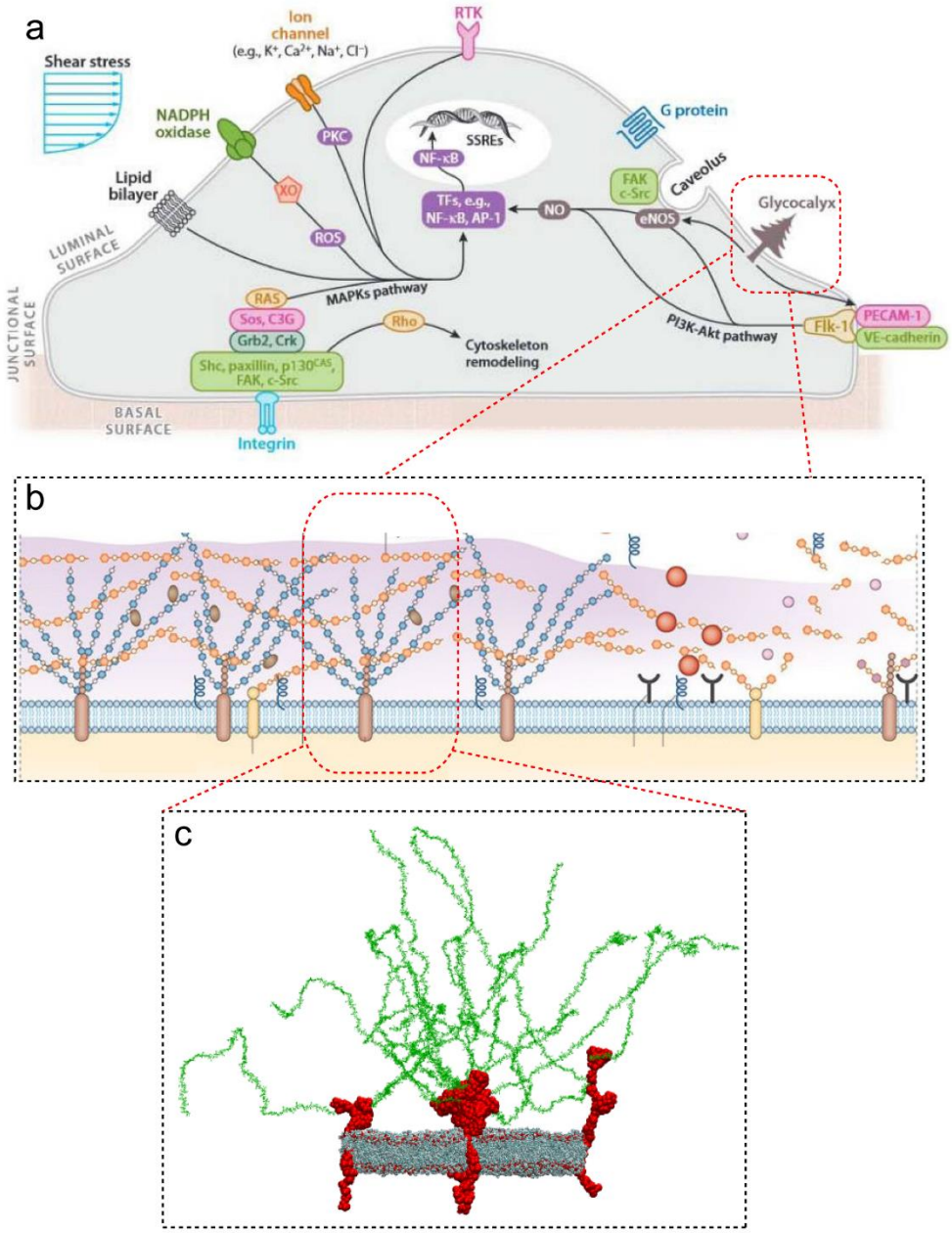

Figure 1-17 An overview of the length scale of the glycocalyx system in this study. a. Mechanosensory pathways utilizing surface mechanoreceptors [109]. b. Characteristic structures of the endothelial glycocalyx. Figure from [10]. c. The focus of this research is a small patch from the endothelial cell surface.

To reach the aims, the following questions are proposed and will be solved in this study.

- How to adopt the molecular dynamics method to mimic the EG exposed to the physiological flow? (Chapter 2)
- What is flow like (e.g. velocity and shear stress) in the presence of the complex EG structure? In turn, how does the EG behave when flow passes by? (Chapter 3)
- What is the mechanism for mechanotransduction of the EG under flow shear stress? (Chapter 4)
- Will flow affect the ion transport of EG? If at all, what is the mechanism? (Chapter 5)

Chapter 2

2 Methodology

2.1 System Construction

The up-to-date structure of glycocalyx with the finest resolution [89] has been used to construct the flow/glycocalyx system [98, 110]. In the system, one glycocalyx element is modelled by the combination of Syndecan-4 proteoglycan and HS sugar chains [98]. The glycocalyx element can be separated into three parts in accordance to the positions to the lipid membrane: Syn-4 ectodomain connected with sugar chains; Syn-4 transmembrane dimer implanted into a lipid bilayer; and cytoplasmic part of the Syn-4 dimer [98].

Figure 2-1 illustrates an overview of the flow/glycocalyx system with its initial configuration [98]. The lipid bilayer separates the simulation space into two regions [98]. Ectodomain, mimicking the travelling space of the blood flow in the lumen, is over the lipid bilayer [98]. The ectodomain is filled with the ectodomain part of the Syn-4 core protein, HS sugar chains connected to the protein, ions and water molecules [98]. The cytoplasm, namely the inner space of the cell, is below the lipid bilayer. Cytoplasmic part of the Syn-4 protein, ions and water molecules are the main components of this region [98]. A NaCl aqueous solution with a concentration of 0.1 M was used to neutralize and solvate the biomolecules. For the three directions (i.e. *x*-, *y*- and *z*-directions), PBCs are applied [98]. Propagation of water molecules between the basal boundary of the cytoplasm and the apical boundary of the ectodomain would be generated as a result of the application of PBCs [98]. Consequently, the micro environments of the cytoplasm

and the ectodomain would be disturbed [98]. Thus, to eliminate the disturbance, a thin layer of graphene is added and fixed on the ectodomain top surface [98]. A previous study [89, 98] have demonstrated the feasibility of such practice. It is noteworthy that the applied graphene layer may cause an artificial boundary layer when the flow velocity is high. In the present study, the flow regime implemented is of low bulk flow velocity and regions far away from the graphene layer are selected for post-processing, so the influence of the artificial boundary layer can be neglected.

In the flow/glycocalyx model, three glycocalyx elements are constructed and planted on the lipid bilayer. Each glycocalyx element (i.e. proteoglycan) bears six HS chains glued to the ectodomain of the Syn-4 core protein dimer. The blood flow is simulated by driving the ectodomain water molecules via external forces on water oxygens [110]. The dimension of the space simulated is a hexagonal area of 820 nm^2 by 72 nm in height [110]. About 5,800,000 atoms are contained in the entire flow/glycocalyx system [110].

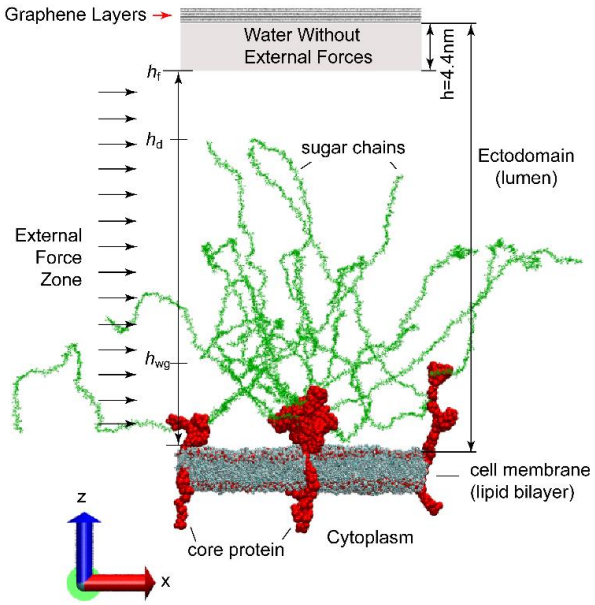

Figure 2-1 An overview of the flow/glycocalyx system with its initial configuration [111]. In the flow/glycocalyx model, three glycocalyx elements are constructed and planted on the lipid bilayer. Each glycocalyx element (i.e. proteoglycan) bears six HS chains glued to the ectodomain of the Syn-4 core protein dimer. The blood flow is simulated by driving the ectodomain water molecules via external forces on water oxygens. Ions and water molecules are not shown. A thin layer of graphene is added and fixed on the ectodomain top surface to eliminate the potential disturbance of water molecules due to the application of PBCs.

2.2 Work Flow Diagram

A diagram describing the work flow of this study is illustrate in Figure 2-2. As shown in Figure 2-2, to investigate the flow/glycocalyx system using the MD method, three procedures are required [98]. The first stage is to establish an equilibrium system with stable structures

of the biomolecules of interest [98]. Only when the system is equilibrated can the flow simulations be undertaken. In the flow simulations, to simulate the flow with different bulk velocities, external forces with varying strengths are exerted on oxygen atoms of water molecules [98]. A physiological flow velocity is supposed to have an order of magnitude of mm/s to cm/s [112-114]. To reach the reasonable range, force iterations are necessary. [98]. Post-processing can be conducted when the bulk flow velocity values in the physiological range [98]. In the post-processing, velocity and shear stress are two fundamental fluid dynamics parameters this study focused on. The essential packages or platforms related to the three procedures are summarised in the diagram as well. [98].

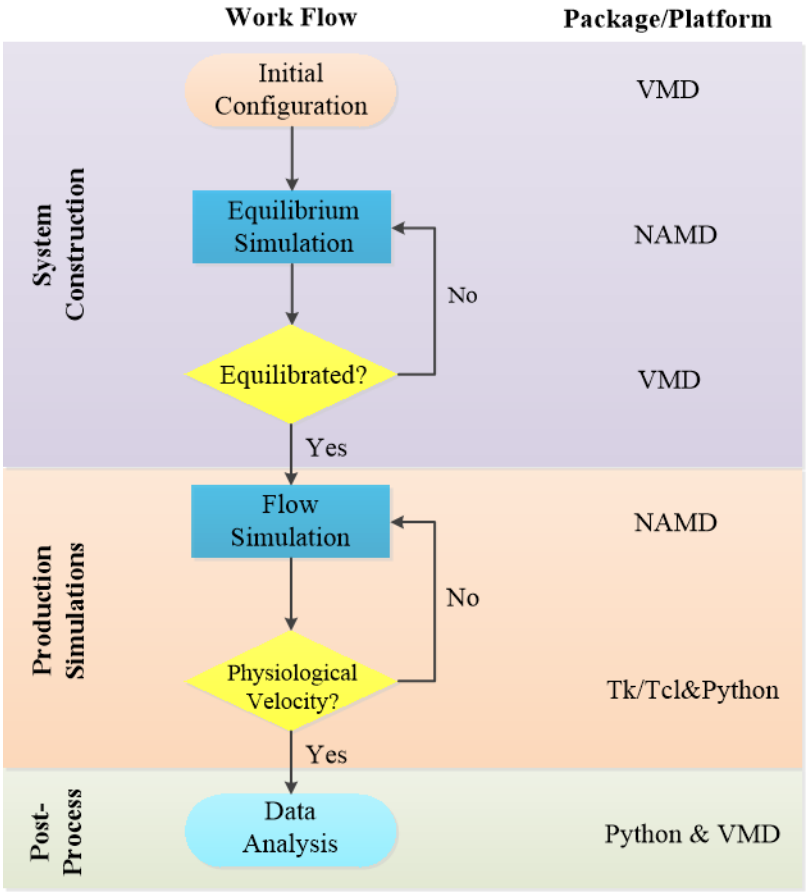

Figure 2-2 Diagram indicating the work flow to conduct large-scale MD simulations for the flow/glycocalyx system and package/platform involved [98]. The main computing package of this research is NAMD 2.9 [115] and vasulisation is realised by VMD [116].

2.3 Protocols

To simulate water molecules, a variety of models can be the candidates, and detailed reviews can be referred to in Refs. [117, 118]. In this study, the TIP3P non-polarizable model [119] was selected to simulate water molecules due to its simplicity as well as good performance in reproducing the properties of H_2O over a range of physical conditions [120, 121]. To calculate the forces conveyed by the

proteins and lipid bilayer, a CHARMM force field for biomolecules [95] was incorporated. Force field parameters from a previous study [89] were adopted to computer the potential energies of graphene layers and sugar chains.

According to the work flow diagram (Figure 2-2), an equilibrium was conducted as an initial step. In the simulation, equilibrium was firstly undertaken in an NPT ensemble with a constant temperature of 310K and a constant pressure of 1 atm for 2 ns. A Langevin thermostat was selected to keep the temperature with a Nosé-Hoover Langevin piston to maintain the pressure were used. Afterwards, another simulation in an NVT ensemble under the Langevin thermostat was undertaken for 0.5 ns to keep the 310K temperature [98]. The initial configuration of the flow simulations was then derived from the last frame of the equilibrium simulation in the NVT ensemble, as illustrated in Figure 2-1 [98]. Due to the advantage in simulating flow situations, the Lowe-Andersen thermostat was adopted in the flow cases to maintain the constant temperature of 310K [111].

To advance the timely atomic positions and velocities, the velocity Verlet integration method [97] was used in all simulations. A timestep of 2 fs was selected to update the positions and velocities of atoms. In the calculation of electrostatics, a particle mesh Ewald [122] method with a grid density of $1/Å^3$ was used [111]. To accelerate calculation, rigid bonds among specific atoms were always assumed. In this study, bond linked to hydrogen atoms were assumed rigid, and a SETTLE algorithm [123] for this practice is implemented. In the computation of

vdW interactions, a cutoff of 12 Å was selected, and a switching function was set to start at 10 Å [111].

The platform where all the large-scale MD simulations were conducted is NAMD 2.9 [115]. With the aid of the VMD [116] package, the molecular structures can be visualised. Self-developed scripts in the language of PYTHON (Python Software Foundation, Wilmington, De) were composed in the post-processing of data [110]. The large-scale MD computations and post-processing irrelevant to visualisation were realised on the national supercomputing service of the UK — ARCHER [98]. Our statistics show that a two-hour parallel computation of 9,000 compute cores can provide all the information of the atomic positions and velocities in 1-ns physical time [110].

2.4 Summary of Cases

In this study, varying situations including the changing blood flow velocity and the shedding of sugar chains will be discussed. Table 2-1 summaries the situations simulated and their principal parameters.

Table 2-1 Principal parameters for in silico experiments.

case	external force (*f*)/ fN	number of sugar chains (*N*)	physical time / ns
a	0.003	18	30
b	0.002	18	21
c	0.001	18	21
d	0	18	8
e	0.01	18	15
f	0.003	15	15
g	0.003	9	15
h	0.003	6 (one dimer)	15
i	0.003 (6 ns) / 0 (6~24 ns)	18	24

For cases f and g, the strategy for removing sugar chains are illustrated in Figure 2-3 (only sugar chain layouts are illustrated here). Panel a is top view of the intact sugar chains (18 sugar chains). After removing the highlighted three chains from the central glycocalyx element in Panel a, 15 sugar chains remain (Case f) as shown in Panel b; by removing the highlighted sugar chains in Panel b, 9 sugar chains remain (Case g) as shown in Panel c. In Case h, only the central glycocalyx element is retained, as will be illustrated in Figure 3-3. In Case i, the external is imposed for the first 6 ns, and afterwards is removed.

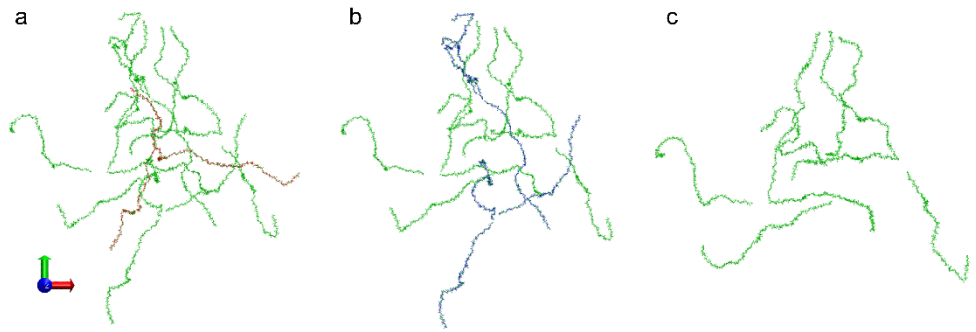

Figure 2-3 Strategy for removing sugar chains in this research (Top views only with sugar chains). a. Sugar chain layout for Cases a to e in Table 2-1 [111]. In these cases, all the sugar chains are retained from the initial configuration. b. Sugar chain layout for Case f in Table 2-1. Three sugar chains (highlighted red in Panel a) are removed from the glycocalyx element in the centre [111]. c. Sugar chain layout for Case g in Table 2-1. Nine sugar chains (highlighted in Panels a and b) are removed [111].

2.5 Post-processing

2.5.1 Averaging Methods

The focus of this study are parameters regarding the ectodomain, such as velocity, flow shear stress and ion molarity. To investigate spatial distributions of these parameters, the ectodomain space is divided into sub-layers individually with height of 2 nm. Within each sub-layer, the parameter of interest is then averaged. Figure 2-4 illustrates two averaging methods used in this research. Panel a illustrates a general sub-layer for averaging parameters; panel b is used for calculating the velocity distribution along the x direction (will

be mentioned in Section 3.1.1). Detailed calculation of each parameter will also be mentioned in corresponding sections.

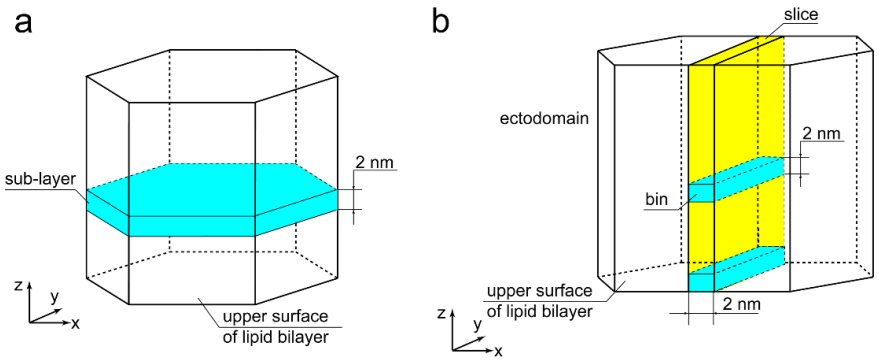

Figure 2-4 Schematic of binning methods used in this research

2.5.2 Geometric Division

To study the influence of biomolecules on flow, the ectodomain region, along the height of EGL (*z* direction), is separated into three sub-regions in accordance to the hallmark biomolecules [98]: flow region (f), dendritic region (d) and near wall region (wg) [98]. The flow region, the upmost and also the simplest sub-region, only contains ions and water molecules [98]. The dendritic region, as self-explanatory, is named for its featured tree-like structure, starts from the apex of ectodomain part of the Syn-4 core protein and ends at the furthest residue of the HS chains. The region is rich in biomolecules, as it includes the majority of HS sugar chains, ions and water molecules [98]. The near wall region, as self-explained by the name, originating from the upper surface of the lipid bilayer to the apex of ectodomain part of the Syn-4 core protein, comprises Syn-4 ectodomain, a few sugar chains, ions and water molecules [98]. To

measure the individual sub-region dimensions, the height origin of the ectodomain space (h_0 in Figure 2-1) should be determined first. The origin is decided by the average positions of heavy atoms (i.e. carbon, phosphor, and nitrogen atoms) of the upper lipid heads (the average z coordinate is 23 Å) [98], as shown in Figure 2-5a. The boundaries of individual sub-regions are then decided by the positions of featuring biomolecules based on the steric information from the 30-ns simulation [98]. The boundaries of the near wall sub-region (h_{wg} in Figure 2-1) and the dendritic sub-region (h_d in Figure 2-1) are 12 nm (Figure 2-5b) and 36 nm (Figure 2-5c) in height, together with h_f equalling 50 nm as designated.

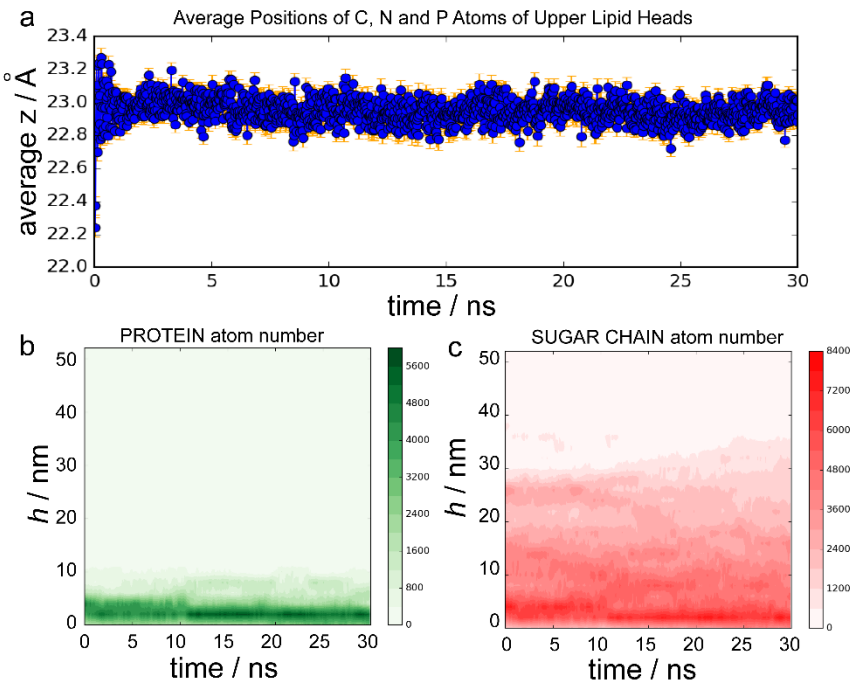

Figure 2-5 Positions of key biomolecules throughout the 30-ns simulation. a. Average heavy atom positions of the upper lipid heads of the bilayer membrane [98]. The average z coordinate is 23 Å, and this position is assigned as the origin of the height. b. Average positions of protein atoms, and 12 nm above the height origin is assigned as the upper boundary of the near-wall region. c. Average positions of sugar chain atoms, and 36 nm above the height origin is assigned as the upper boundary of the dendritic region.[110]

Chapter 3

3 Coupled Dynamics of Flow and EG

3.1 Flow Velocity Distributions

The external force of 0.003fN on the water oxygens provides a laminar flow for the system (The derivation can be found in Appendix A) [110]. To explore the pattern in which the glycocalyx constituents affect the resulting flow, flow profiles including the temporal and spatial velocity distributions of water molecules in the ectodomain are to be discussed [110].

3.1.1 Spatial Distributions of Velocities

The spatial *x*-direction velocity distribution of water molecules in the ectodomain along the EG height was first investigated [110]. The blood flows in the *x*-direction. Following the flow, five slices have been selected near the centreline $x = 0$ [110]. The widths, in the *x* direction, of slices are 2 nm, with centrelines of the individual slices being -8 nm, -4 nm, 0, 4 nm and 8 nm, respectively (Figure 3-1a) [110]. Within individual slices, 25 equal vertical bins along the height were further generated as illustrated in Figure 2-4b [110]. Average velocities of the *x*-direction velocities of water molecules were calculated in these bins [110]. From the time scale, averaging was conducted for the time interval from 27 to 30 ns. As illustrated in Figure 3-1, all of the five selected slices present us with oscillating velocity distributions along the height [110], which is distinguished from the smooth velocity distribution on bare surface under laminar flow conditions [124]. The discrepancy suggests that as an obstacle to the flow, the glycocalyx

disturbs the blood flow by modifying the flow velocity distributions [110]. In addtion, the velocity curves at x = 0 and x = - 4 nm regions, where more glycocalyx atoms gather (The numbers of glycocalyx atoms in the x = 0 and x = - 4 nm slices are 11368 ± 707 and 6214 ± 404, respectively.), are smoother than those at x = -8 nm (P < 0.05) with fewer glycocalyx atoms (with number of glycocalyx atom being 4521 ± 278) [110], which indicates the glycocalyx constituents can modulate the velocity (P-values for the comparisons can be found in Appendix B) [110]. A supplementary *in silico* experiment has been undertaken for comparison to validate the conclusion that the oscillating velocity distributions are mainly attributed to the disturbance of the EG instead of computational noises (Details can be referred to Appendix C).

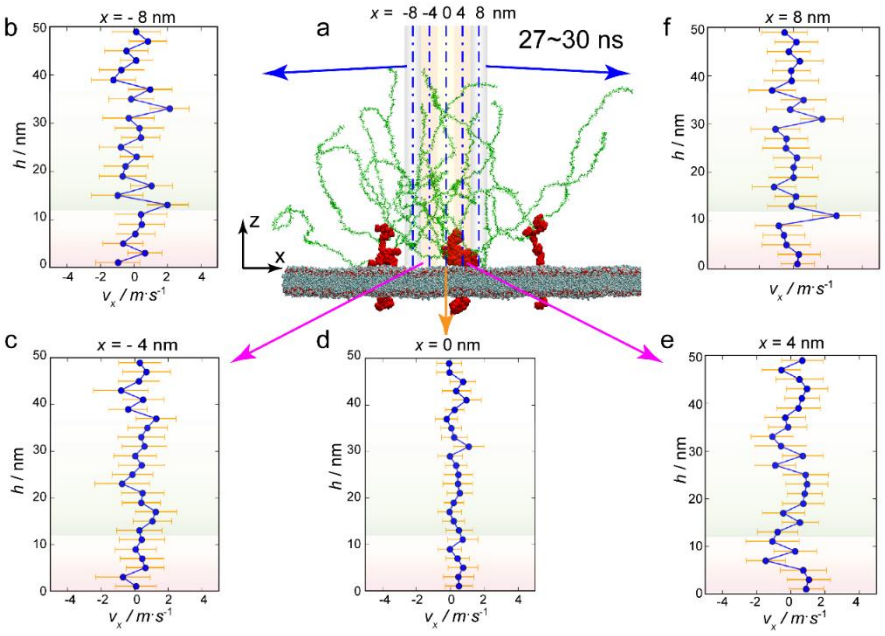

Figure 3-1 Spatial velocity distributions based on the averaging from 27 to 30 ns [110]. a. Snapshot of the system configuration at the instant of 30 ns, and illustrations of the five selected slice positions along the x direction [110]. Ions and water molecules are not shown. b.- f. Velocity distributions along the height of five selected slices with centreline positions being x = -8 nm, -4 nm, 0, 4 nm and 8 nm, respectively [110].

3.1.2 Temporal Distributions of Velocities

By equally slicing the whole ectodomain into 25 sub-layers (as illustrated in Figure 2-4a), the velocity distributions with time throughout the 30-ns simulation was then investigated [110]. For the time-evolution, the *x*-direction velocities were averaged every 10 ns [110]. Each sub-layer in this section includes more water molecules than those in the spatial distribution study (Section 3.1.1), and more frames were involved [110]. The oscillating velocity distributions can

still be witnessed, as expected, at consecutive time intervals (in Figure 3-2a) [110]. The oscillating velocity distributions, thus, further demonstrated the previous conclusion that the glycocalyx constituents interrupt blood flow by modifying the velocity curves [110].

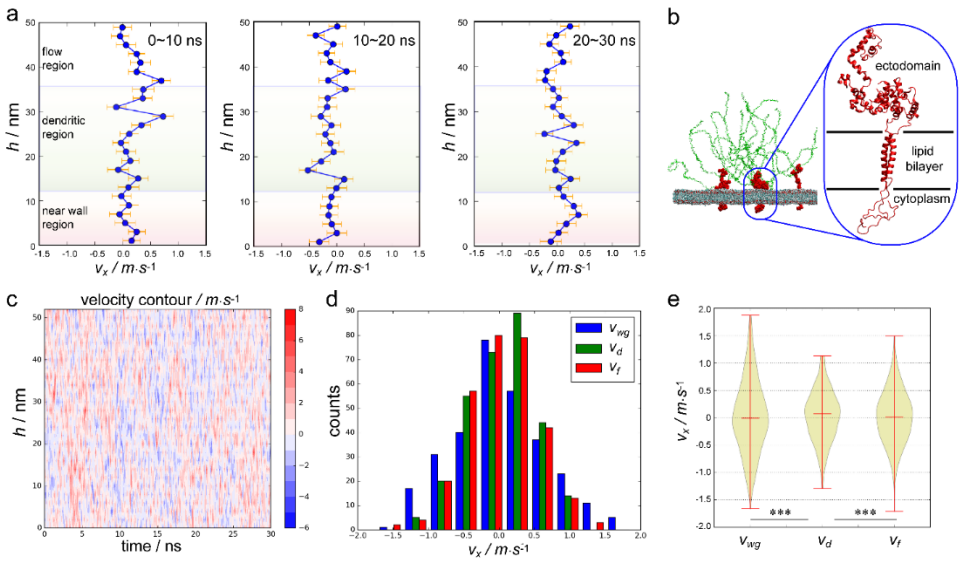

Figure 3-2 Temporal velocity distributions at consecutive time intervals and hierarchical velocity distributions of sub-regions [110]. a. Velocity distributions averaged in three consecutive time intervals of 0~10 ns, 10~20 ns and 20~30 ns [110]. b. The secondary structures of ectodomain core protein are mainly α-helixes [110]. c. Instantaneous spatial velocity distributions for all recorded frames of the 30-ns simulation [110]. d. Statistical distributions of average velocities of the three sub-regions for all recorded frames of the 30-ns simulation [110]. e. Violin plot showing the variations of velocities of the three sub-regions [110]. Statistical significance is given by: *P<0.05; **P<0.01; and ***P<0.001, and detailed P-values can be found in Appendix B.

3.1.3 Hierarchical Velocity Distributions

Hierarchical velocity distributions of the ectodomain are spotted among the three sub-regions (i.e. flow, dendritic and near-wall regions) [110] as well, as shown in Figure 3-2a. In the near wall region, despite some turns, the velocity curve, in general, has a smooth and uniform

trend, particularly from 10 to 20 ns [110]. In contrast, corners, some of which are significant, frequently appear in the dendritic region [110]. The different structural features of hallmark biomolecules within the sub-regions can account for the velocity curve differences [110]. In the near wall region, the ectodomain parts of the core protein owning secondary structures of "stubborn" α-helixes (Figure 3-2b) govern the flow [110]. A scrutiny of the dynamics of the core protein ectodomain part (will be mentioned in Section 3.3) indicates that the motion of the stable α-helixes in the flow direction is confined in a limited area due to its lump-like conformation [110]. In sharp contrast, in the dendritic region, flexible sugar chains "swim" easily and randomly in the flow and dissipate the momentum of the flow [110]. Hence, the ectodomain core protein sterically hinders flow mainly via its lump-like conformation, whereas flexible sugar chains modify the velocity profiles via their free motion [110].

To gain extra insights into the hierarchical distributions of flow velocities, the spatial velocity distributions were calculated every 0.1 ns throughout the 30-ns simulation, generating a velocity contour as illustrated in Figure 3-2c [110]. The interweaving distributions of velocities with positive and negative signs spatially and temporally, as expected, validate that the flow is remarkably distorted by the glycocalyx constituents [110].

For all the recorded frames of the 30-ns simulation, the instantaneous velocities in the flow direction within the three sub-regions were also averaged [110]. The distributions are shown in Figure 3-2d and e. In Panels d and e, v_f, v_d and v_{wg} are the represent

bulk flow velocities in the flow, dendritic and near wall regions, respectively [110]. Statistics do not show significant difference in the velocity distributions among the three sub-regions (P-values between any two distributions in Figure 3-2d are larger than our defined significance level). However, in the violin plot (Figure 3-2e), a small velocity variation is illustrated in the dendritic region [110]. (Detailed statistical information of Figure 3-2 d and e can be found in Appendix B.) The small velocity variation implies that the flexibly moving sugar chains can mediate the flow with reduction in the flow fluctuations via frequent interplays with surrounding water molecules [110].

3.2 Flow Shear Stress Distributions

The shear stress distributions of the glycocalyx layer and its ectodomain surroundings were then studied [110]. One component of the stress tensor — the shear stress on the plane normal to *x*-axis in the *z* direction- τ, is used to represent the shear stress [110], which is calculated by Eq.(3-1)

$$\tau = \mu \frac{\partial v_x}{\partial z} \qquad (3\text{-}1),$$

where μ is the viscosity of the water from the TIP3P model with a value of 0.321 mPa·s [125]; and $\partial v_x/\partial z$ is the gradient of the *x*-direction velocity along the *z* axis.

The shear stress within each layer was calculated by the forward difference method. Instantaneous shear stresses were averaged within the three individual sub-regions on a 0.1-ns basis. The corresponding counts were investigated [110]. As shown in Figure 3-3a, Kolmogorov-Smirnov (K-S) tests have statistically confirmed that

hierarchical distributions also exist in shear stresses of the three sub-regions [110]. Apart from the shear stress, the pertinent magnitude distributions (Figure 3-3b) are studied. Results show that the weakest shear stress appear in the dendritic region with the relatively small magnitude of shear stress [110]; on the other hand, the strong shear stresses are more likely to appear in the near-wall and flow regions [110]. Accordingly, the strength order of the shear stresses from strong to weak gives: $|\tau_{wg}| > |\tau_f| > |\tau_d|$ (P-values can be found in Appendix B) [110].

The hierarchical distributions of shear stresses can be explained by the sophisticated glycocalyx configuration [110]. The highly dynamic sugar chains in the dendritic region consume the fluid momentum via frequent interplay with the neighbouring water molecules, reducing the *x*-direction velocity gradient along the *z* axis [110]. Whereas, the intensive interactions between the lipid bilayer and the neighbouring water molecules in the near-wall region will act through a friction-like effect to the flow. These interactions contribute to a significant *x* velocity gradient along the *z* axis [110].

An additional *in silico* experiment (Case h in Table 2-1) containing only one glycocalyx element with six HS sugar chains attached to the core protein dimer was conducted for comparison (Figure 3-3c) [110]. The additional simulation lasts for a physical time of 15 ns, and the external forces on water oxygens remain 0.003 fN [110]. The probabilities of obtaining $|\tau_{wg}| > |\tau_f|$ in both cases were computed [110]. As shown in Figure 3-3d, the three-dimer case prevails over its one-dimer counterpart in the probability of having enhanced near-wall

shear stress ($|\tau_{wg}|/|\tau_f|>1$ in Figure 3-3d), particularly for extra strong shear stress ($|\tau_{wg}|/|\tau_f|>1.5$, 2, 2.5 and 3 in Figure 3-3d) [110]. Thus, it can be concluded that the lump structure of the ectodomain part of core protein facilitates the formation of strong shear stress, in particular, for the formation extra strong shear stress [110].

On the contrary, weakened shear stress can be observed in both cases in the dendritic region [110]. Furthermore, weak shear stress ($|\tau_d|/|\tau_f| < 1$ in Figure 3-3d), particularly extra weak shear stress ($|\tau_d|/|\tau_f| < 0.75$, 0.5, 0.25, and 0.1 in Figure 3-3d), is less often detected in the three-dimer situation than in the one-dimer situation. The difference can be attributed to the extremely frequent interactions between sugar chains and the flow in the three-dimer case [110]. The excessive interplays disrupt the flow velocity profile, albeit regulating velocities [110].

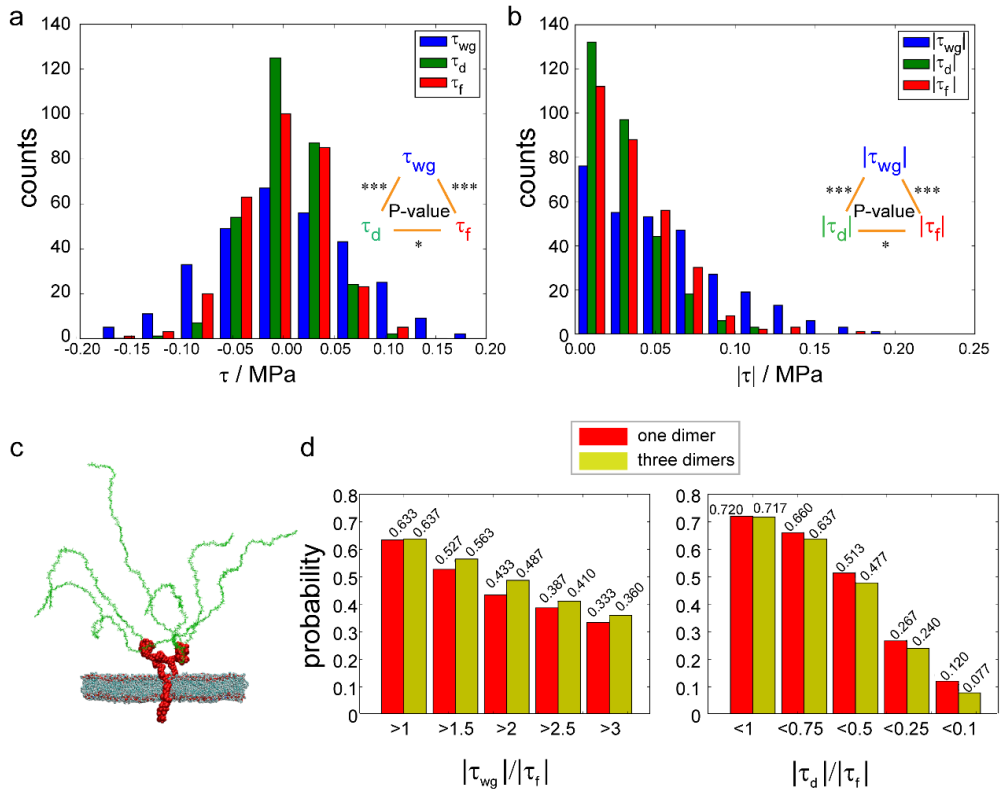

Figure 3-3 Shear stress distributions of the three sub-regions in the ectodomain [110]. a. Distributions of shear stresses with signs and statistical information [110]. b. Distributions of shear stress magnitudes and statistical information [110]. c. Snapshot of the one-dimer glycocalyx system [110]. Ions and water molecules are not shown. d. Comparisons of probabilities, between the three-dimer and one-dimer the cases, for strong shear stress in the near wall region and for weak shear stress in the dendritic region [110]. Statistical significance is given by *P<0.05; **P<0.01; ***P<0.001. Details can be referred to Appendix B.

3.3 Dynamics of EG

The dynamics of the glycocalyx element in the centre is further scrutinised to reveal additional implication to the interplay between the blood flow and the glycocalyx. Of the glycocalyx element, the

ectodomain part of the Syn-4 core protein and four segments, individually comprising five residues, from two HS sugar chains were examined with their motions, as shown in Figure 3-4a [110]. Segments P1 and P2 are extracted from Chain 1 and Chain 2 respectively, located at the 40% of the total length of each sugar chain with Segments P3 and P4 at the end of the two sugar chains. To describe the motions of these segments, polar coordination system was adopted, as illustrated Figure 3-4a. Meanwhile, to facilitate comparison, the coordinates of centre of mass of the transmembrane protein (COM_T) were aligned among all the recorded frames throughout the 30-ns simulations. In Figure 3-4a, R is the distance projection, on the XOY plane, between the centre of mass (COM) of the segment investigated and COM_T, and θ is the angle between the projection R and the positive x direction [110].

Motions in the swing form are revealed from the x-direction position fluctuations of these five segments of interest, as illustrated in Figure 3-4b [110]. Specially, the more fierce fluctuations of the four sugar chain segments than its ectodomain protein counterpart further corroborates the conclusion that stronger disturbance in water flow is generated by the free and dynamic sugar chains than by the ectodomain part of the Syn-4 core protein [110]. Motions in the swirling form were also observed in all the five segments in the 30-ns simulations as shown in Figure 3-4c [110].

An interesting behaviour about one sugar chain is noteworthy here. For Chain 1, its coiled initial configuration is gradually uncoiled by a wave generated from the swing motion of the connected core

protein as flow passes (Figure 3-4d) [110]. Such fascinating behaviour further demonstrates that interactive dynamics also prevail within glycocalyx constituents [110].

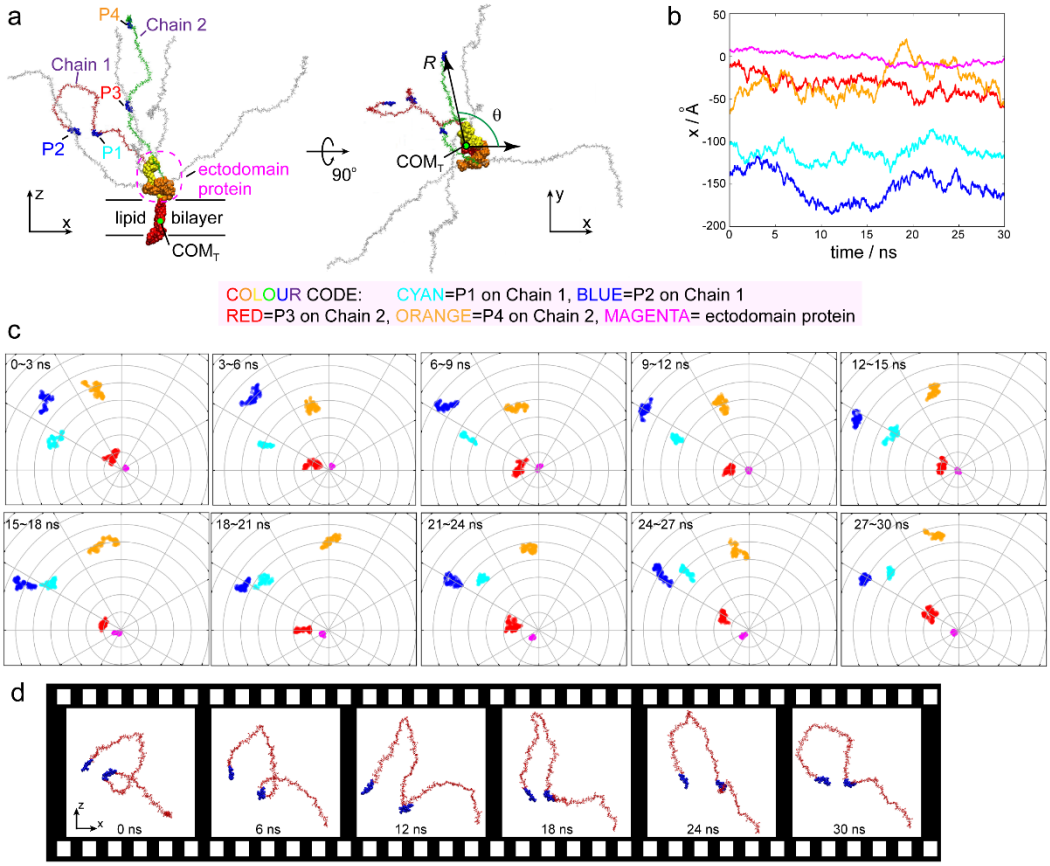

Figure 3-4 Dynamic motions of the glycocalyx constituents [110]. a. Illustration of five segments to be investigated and the polar coordinates. b. Motions in the swing form of the five segments investigated. c. Motions in a swirling form of the five segments investigated [110]. Panels b and c share the same colour code. d. Consecutive snapshots showing the uncoiling of a sugar chain with a coiled initial configuration [110].

3.4 Discussion

3.4.1 Flow and EG conformations

To explore the extent how biomolecular conformations influence flow structures, an additional case with a flow velocity larger than the physiological situation is conducted for a physical time of 15 ns. The external force in the fast flow case is 0.01 fN (Case e in Table 2-1) [98]. For comparison, data from the first 15-ns simulations were extracted from the physiological case (f = 0.003 fN). Velocity distributions were averaged very 5 ns for both cases [98]. As shown in Figure 3-5, oscillating velocity distributions, as expected, are observed for both flow cases, as a result of steric hindrance and disturbance from the glycocalyx constituents as described in Section 3.1.3 [98].

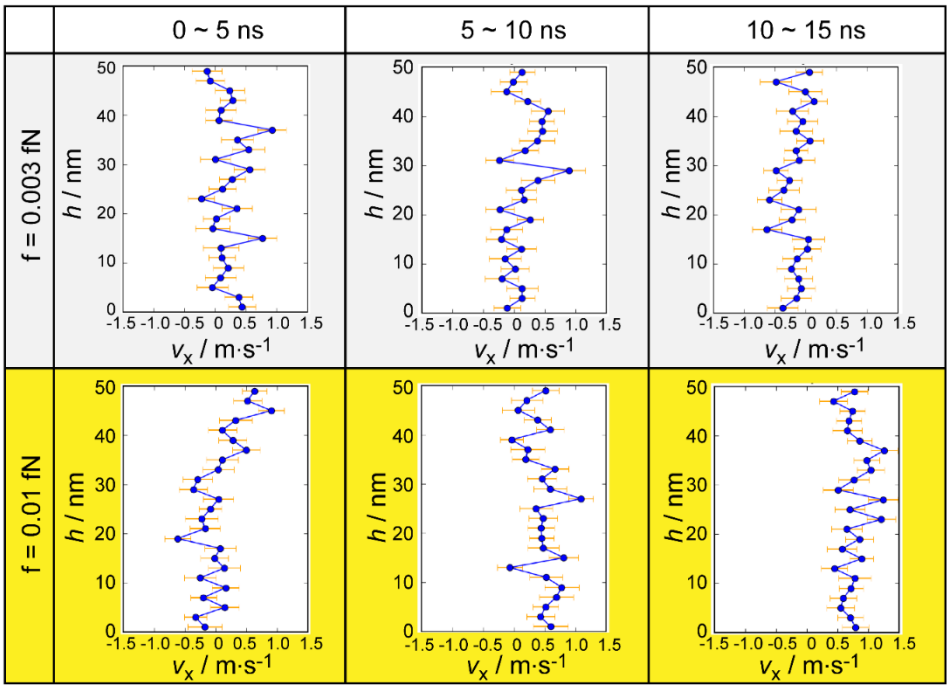

Figure 3-5 Oscillating distributions of *x*-direction velocities along the height at successive time internals for physiological and fast flow cases [98].

Comparisons in Figure 3-5 illustrate that a slight increase in the flow velocity merely results in a small bulk flow velocity increase with the oscillating feature of the velocity distributions unchanged [98]. Indeed, no significant differences are detected in biomolecular conformations of the glycocalyx constituents between the two cases with varying flow velocities, as illustrated in Figure 3-6 a and b [98]. The evenly distributed sugar chains impose steric disturbance on the movements of water molecules, resulting in the oscillations in velocity curves [98]. Nevertheless, if an excessively increased external force was imposed (say 0.001 pN), which was the practice reported in Ref. [89], the spatial distribution of sugar chains was changed and remarkable conformational changes of the glycocalyx constituents were caused (Figure 3-6c) [98]. The resulting velocity in a certain region (h > 25 nm) of ectodomain can be as high as 10 m/s (In Ref. [89] (the authors only exerted external forces on water oxygens in the upper half of the ectodomain). No obvious velocity oscillating was detected from their observations as illustrated in Figure 3-6d). Therefore, the premises of an oscillating velocity distribution are the evenly distributed layout of the glycocalyx and a moderate bulk flow velocity.

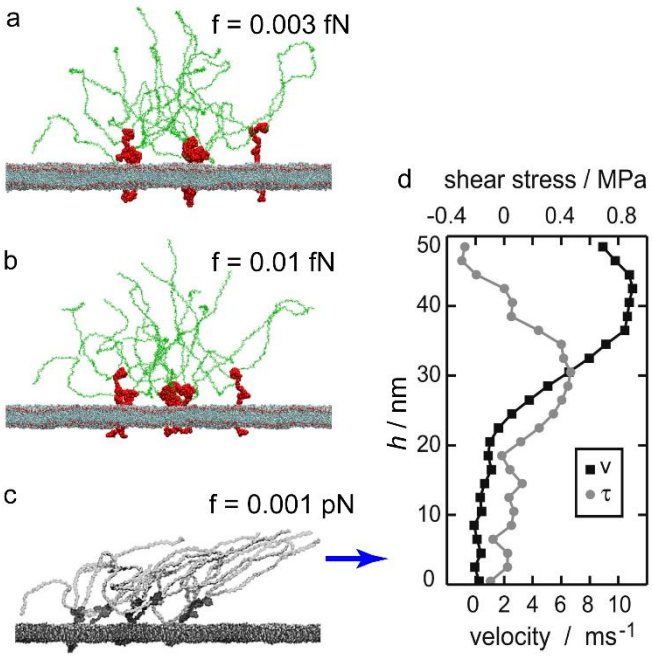

Figure 3-6 Conformations of the endothelial glycocalyx sugar chains under situations of varying velocities and a reported distribution of velocity from Ref. [89]. a. Snapshot of glycocalyx sugar chain conformations in the case with a physiological velocity (Case a) [98]. b. Snapshot of glycocalyx sugar chain conformations in the case with an slightly accelerating flow velocity (Case e) [98]. c. Snapshot of glycocalyx sugar chain conformations in the case with an extremely fast velocity. d. The *x*-direction velocity distribution which result in the deformation of sugar chains in c. from a previous study [89].

3.4.2 Flow Regime on Complex Surface

Section 3.4.1 suggests that patterns of flow over coarse surfaces grafted with flexible structures (e.g. glycocalyx) are determined by both the momentum conveyed by the flow itself and the spatial disturbance exerted by the obstruction [111]. To reveal the regimes of flow on

coarse surface grafted with dynamic structures, besides the physiological flow case (Case a), three additional cases were also included, i.e. Cases f, g and i in Table 2-1. In cases f and g, flow under varying sugar chain configurations were considered. In Case i, the external force of 0.003 fN was first imposed for 6 ns, and afterwards removed. The time-evolutions of the bulk flow velocities for the four cases are illustrated in Figure 3-7. In Case a (Figure 3-7a), velocity fluctuations around 0 were detected, indicating a force balance between force exerted on the water molecules and that generated by the interplays between the glycocalyx constituents and their surrounding water molecules [111]. It is noteworthy that, in Case i (Figure 3-7b), after the 6-ns load from the external forces, an increase in the bulk velocity the of the ectodomain, from 6 to 14 ns, was detected which can be attributed to inertia. Afterwards, the flow velocity experienced a significant decrease till 19 ns [111]. An equilibrium of velocity was then reached. As for Cases f and g (Figure 3-7c and Figure 3-7d, respectively), the velocities developed in a slightly increasing trend, which can be explained by the reduction in the spatial obstruction from the removal of glycocalyx sugar chains [111].

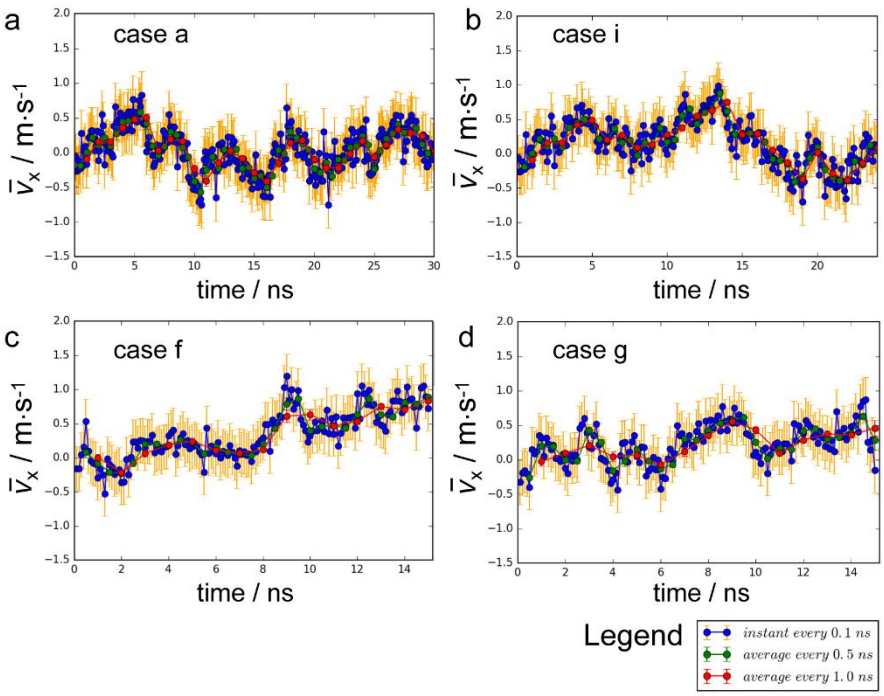

Figure 3-7 Time-evolutions of the Cases a, i, f and g [111].

Based on the velocity pattern illustrated in Figure 3-6 and time-evolutions in Figure 3-7, a diagram depicting the regimes of flow on coarse surface drafted with dynamic structures is proposed [111], as shown in Figure 3-8. In the diagram, the Reynolds Number (Re), is select to indirectly quantify the momentum conveyed by the fluid. Additional indicator representing geometry of the dynamic structures of the surface (Geo) is proposed to quantitively describe the spatial disturbance from the surface obstacles [111]. The Geo number is expected to incorporate all the geometric information about the obstacles, such as the quantity and the layout of the sugar chains in this study. A typical expression of the Geo number can be a linear combination of all the influencing parameters, as demonstrated in Eq. (3-2) [111].

$$\mathrm{Geo} = f\left(N, x_1, ..., x_i\right) = a_0 N + \sum_i a_i x_i \qquad (3\text{-}2)$$

In Eq. (3-2), the quantity of sugar chains is expressed by N , and the geometric parameters from the obstacles are represented by x_1 to x_i [111]. Contributions of individual geometric parameters are quantified by coefficients a_0 to a_i [111]. When the momentum conveyed by the flow is balanced by the spatial disturbance, the pertinent state can be represented in terms of Geo and Re numbers. A set of Geo and Re numbers from numerous balanced situations then forms the balance curve in Figure 3-8. The diagram of the flow regimes is then separated into two regions by the balance curve: a region where velocity dominates and the other obstruction dominates [111]. The naming of both regions is self-explanatory, in the velocity-dominant region, the momentum dissipated by the spatial obstacles is smaller than that carried by the fluid, and the extra momentum from the fluid can change the conformations of dynamic structures to a preferable state (usually with deformations parallel to the flow direction) [111] as illustrated in Figure 3-6. Whereas, in the other situation, which the obstacle-dominant region mainly refers to, the interplays between the obstacles and the fluid consume the energy of flow, finally resulting in a stationary state featuring equilibrium [111].

Figure 3-8 involves three flow regimes: balanced, velocity-dominant and obstacle-dominant. The four flow scenarios discussed in the section can be categorised by the three regimes. For the sake of simplification, in the expression of the Geo number, only the quantity of sugar chains (N) is considered in the following discussion. The four flow scenarios are then marked in the flow regime diagram. Case a is a balanced state for the velocity oscillates around a certain value. The

Geo number of Case i is identical to Case a, but no external forces are imposed to the system of Case i. Therefore, Case i should be marked to the left of Case a [111]. The number of sugar chains in Case f (or g) is reduced, leading to a declined Geo number. The removal of the sugar chains on the other hand decreases the spatial disturbance to the flow, thereby increasing the Re number. As a result, Case f (or g) is expected to be on the lower-right side of Case a [111].

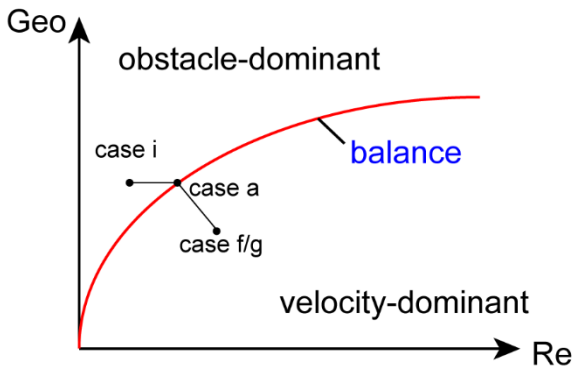

Figure 3-8 Diagram of flow regimes on coarse surface grafted with dynamics obstacles [111]. The four flow scenarios (Cases a, f, g and i) discussed in this sections are marked based on corresponding Re and Geo numbers [111]. For simplification, only the quantity of sugar chains is incorporated in the Geo number[111].

3.4.3 Biological Significance— Alternative Force Transmission Pathway

The question — via which route does the glycocalyx transmit the flow shear stress into the cytoskeleton? — is among the changing issues in the hypotheses regarding the mechanisms for mechanotransduction of the endothelial glycocalyx [110]. A popular

idea from previous studies [46, 47] proposed that the force from the flow shear stress load is transmitted into the cytoskeleton following the "flow – sugar chains – core protein – cytoskeleton" sequence [110]. In the present study, in accordance to the dynamics of the ectodomain part of the core protein and the flexible sugar chains (as shown in Figure 3-4), an alternative pathway can be proposed that forces from the flow shear stress load can be transmitted straightforwardly to the core protein, without passing the dynamic sugar chains, as the correlation between movements of the ectodomain part of the core protein and the sugar chains is weak [110]. Both routes proposed from previous and present studies are potential and reasonable pathways of force transmission via the endothelial glycocalyx [110]. The following chapter will discuss in detail about the force transmission mode via transmembrane core protein to the cytoskeleton.

Chapter 4

4 Mechanism for Mechanotransduction via EG

4.1 EG as Soft Matter

The dynamics of the glycocalyx sugar chains revealed in Section 3.3 imply that the glycocalyx is not rigid body in reality. By accessing the structures of the glycocalyx, we find the glycocalyx with tender sugar chains is soft matter rather than rigid in previous studies [46, 47]. Even for the core protein of the glycocalyx, secondary structures (Figure 4-1a) show that flexible linkages between subdomains of ectodomain Syn-4 (EA1 and EA2 from Chain A, and EB1 and EB2 from Chain B) as well as Syn-4 ectodomain and transmembrane parts (TA1 and EA1 for Chain A, and TB1 and EB1 for Chain B) encourage the glycocalyx to perform like a soft matter. To study the dynamics of the soft matter, three angles (θ_T, θ_{E1} and θ_{E2} in Figure 4-1) were employed to record positions of the ectodomain and transmembrane Syn-4. Also, a control case with no flow (i.e. Case d) was incorporated for comparison. As shown in Figure 4-1b and c, significant increases in θ_{E1} and θ_{E2} can be observed when flow passes by, whereas θ_T remains stable regardless of whether there is flow or not. The inconsistent and unsynchronised movements of the core protein subdomains can also be found in the distances between subdomains as shown in Figure 4-1d. Therefore, previous models deeming the glycocalyx as rigid body to transmit force are limited and insufficient. Instead, forces are likely to be transmitted by the dynamics of glycocalyx as a soft matter. The changes in the lengths of the transmembrane helixes were examined as shown in Figure 4-1e. Each

helix can be individually regarded as inextensible, as the changes are so insignificant. It can also be concluded that force is not transmitted via the stretching of transmembrane helixes.

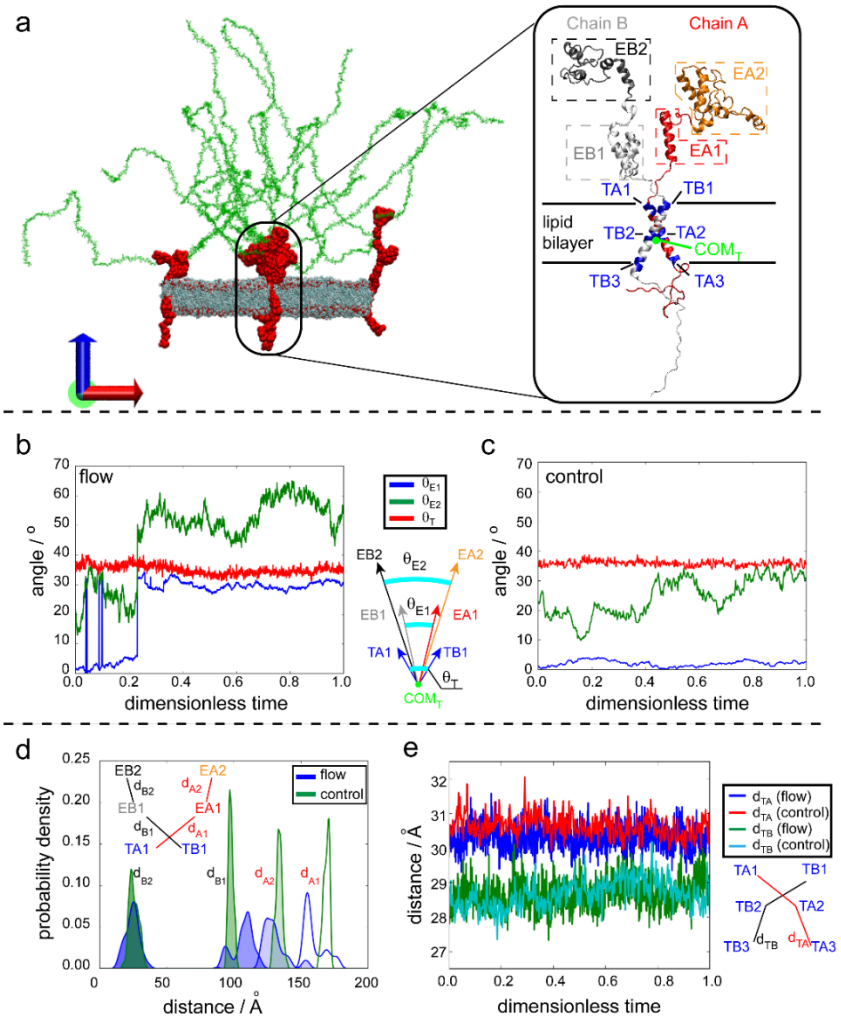

Figure 4-1 Movements of ectodomain and transmembrane Syn-4.

(a) Secondary structure of the Syn-4 core protein. (b) and (c): Three angles with joints at the centre of mass of the transmembrane dimer (COM_T) are used to gauge the motions of ectodomain and transmembrane Syn-4 proteins in the flow (b) and the control (c) cases. The flow causes fierce angular motions of ectodomain Syn-4 protein, but exerts slight effects on the angle change of the transmembrane dimer. (d) Distance changes in the core protein subdomains. (e) Distances (d_{TA} and d_{TB}) representing the lengths of two transmembrane helixes in the flow case and in the control case. The changes in helix lengths are so insignificant that each helix can be individually regarded as inextensible.

4.2 Force Transmission Mode and Order of Magnitude

To explore potential motion modes in which forces are transmitted via the soft glycocalyx, we further examined both the motion and the conformational changes of the transmembrane Syn-4 via three angles (Figure 4-2): θ_{AB} (Figure 4-2a) to quantify the relevant positions of the two chains of the dimer; and θ_A and θ_B (Figure 4-2b) to measure deformation of each chain. Figure 4-2a reveals a "scissor-like" motion of the dimer chains in the presence of flow, due to the significant variations of the angle θ_{AB} in the flow case ($p < 0.001$). Meanwhile, the declining median value (Figure 4-2b) of θ_{AB} from 55.6º in the control group to 52.5º in the flow case indicates that the blood flow can cause the closure of the transmembrane dimer chains. The flow also stretches Chain A with the median value of θ_A increasing from 158.6º in the control group to 161.5º, but exerts insignificant effects on the bending of Chain B. Since both the scissor motion of the two chains and the deformation of Chain A can contribute to the changes of θ_{AB}, we then postulate that force is mainly transmitted by this particular scissor motion of the dimer, alongside the stretching of one chain of transmembrane dimer. Furthermore, a 2D geometric derivation (in Appendix D) predicts that the scissor motion of the two dimer chains accounts for 53% of the change in θ_{AB}.

To test our postulation of the force transmission mode, principal component analysis (PCA) [126] was conducted to thoroughly assess the dynamics of the transmembrane Syn-4. PCA results in Figure 4-2c show that the scissor motion of the two chains is the first principle motion mode of the transmembrane protein, followed by two bending

modes of the dimer in two planes. These three modes constitute 97% of the transmembrane dimer motion, which corroborates our postulation that the forces are transmitted via the scissor motion and the bending of the glycocalyx transmembrane dimer. It is also worth noting that scissor motion of the transmembrane dimer occupies about 55% of all the XOZ plane modes, which validates our estimation of the 53% contribution rate to θ_{AB} change.

The core proteins of the glycocalyx are usually linked with actin filaments of the cytoskeleton [20, 109]. The angle changes of the transmembrane proteins under the flow shear stress will result in deformations of the filaments or even rupture of the linkage between the protein and the cytoskeleton. To gain additional insight regarding the order of magnitude of the force transmitted into the cytoplasm, a steered molecular dynamics (SMD) simulation was conducted. The key point of an SMD method is to impose an external force to certain atom(s) and explore biological processes under this force [127-129], like those explored using atomic force microscopy. The probability density function (PDF) of the force (Figure 4-2d) from our SMD results indicates that forces with an order of magnitude of 10~100 pN were required for angle change of the presumed range. Due to the rigidity of the α-helix structure of each transmembrane dimer chain (the lengths of both α-helix chains remain stable as shown in Figure 4-1e), the lever principle was then used to estimate the force transmitted into the cytoplasm. The force transmitted to the cytoplasm end of the dimer exhibits an order of magnitude of 10~100 pN. This order of magnitude is also in good agreement with atomic force microscopy [130-132]

results in other biomolecular studies, such as titin unfolding [133], RNA stretching [134], and protein conformation changing [48, 135, 136]. Therefore, the force transmitted from the ectodomain flow to the cytoplasm by the glycocalyx with an order of 10~100pN can also be used to estimate the force transmitted into the cytoskeleton via the core protein.

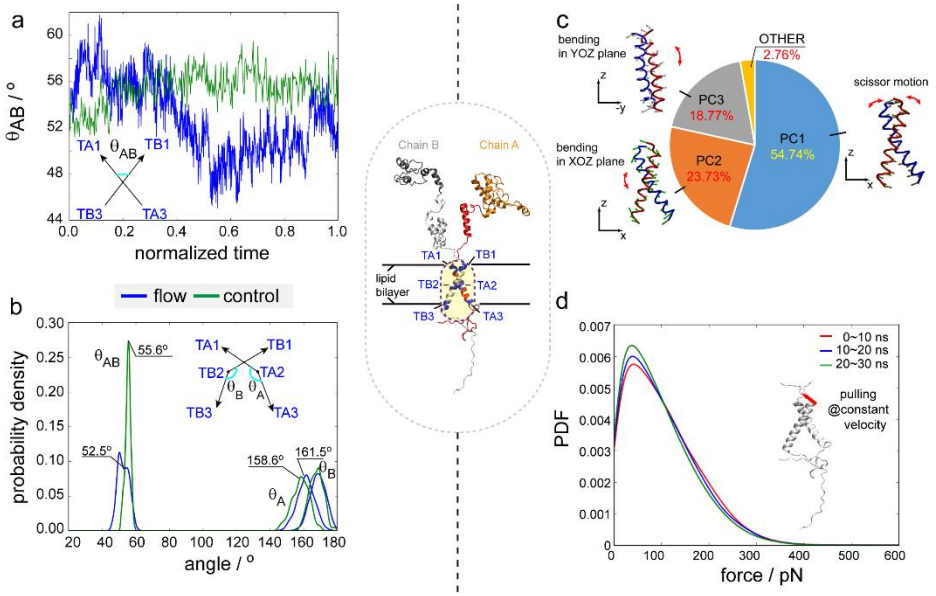

Figure 4-2 Force transmission mode via the transmembrane part of the core protein and its order of magnitude. a. Large angle variations of θ_{AB} in the flow group ($p < 0.001$ by Fligner-Killeen Test). b. Typical angle changes of the transmembrane dimer. Flow closes the angle of θ_{AB} by 3.1 degrees, and θ_A indicating the stretching of Chain A increases by about 3 degrees. c. PCA analysis of the motions of transmembrane protein. Scissor motion of the two chains is the first principle motion mode of the transmembrane protein, followed by two bending modes of the dimer in two planes. d. PDF for forces generated by flow shear stress using SMD simulations. A constant velocity of 0.0018 m/s was imposed on the end of one chain of the transmembrane dimer. To maintain the constant pulling velocity, forces with order of magnitude of 10~100 pN were required.

4.3 Role of Sugar Chains

The potential influence factors associated with the mechanotransduction — the blood velocity and the reduced number of sugar chains which are two critical factors related to cardiovascular diseases [109, 137] were then explored. Three flow cases, i.e. Cases a to c, were studied here to investigate the effects of flow velocities on mechanotransduction. The angle distributions of the transmembrane dimer chains under varying external forces are shown in Figure 4-3a. The decrease in the median value of θ_{AB} with the ascending external forces indicates that the strong impulse by the external force favours the closure of the scissor motion. Meanwhile, the impulse by the external force intensifies the scissor motion, as the variations of θ_{AB} increase as the external force increases.

To unveil the functionality of the sugar chains, two scenarios with reduced number of sugar chains were constructed, i.e. Cases f and g in Table 2-1. As illustrated in Figure 4-3b, the decline in the median value of θ_{AB} suggests that one principal function of the sugar chains is to resist the flow and to prevent severe conformational changes of the transmembrane dimer. The decrease in the variation of θ_{AB} after the removal of the central sugar chains (Cases a and f) indicates that the removed sugar chains per se of the central glycocalyx element could intensify the scissor motion if they were preserved. By contrast, the increase in the variation of θ_{AB} with the removal of the surrounding sugar chains (Cases f and g) reveals that the presence of the surrounding sugar chains impedes the scissor motion of the central glycocalyx element by confining the movement of the central sugar

chains connected to the core protein. This can also be validated by the comparisons of root mean square deviation (RMSD) values of three sugar chains from the central glycocalyx element (Figure 4-4a) under different removal scenarios. As illustrated in Figure 4-4b, the three sugar chains individually have increasing RMSDs as the surrounding sugar chains shed from the glycocalyx, which means the surrounding cohorts hinder their motions.

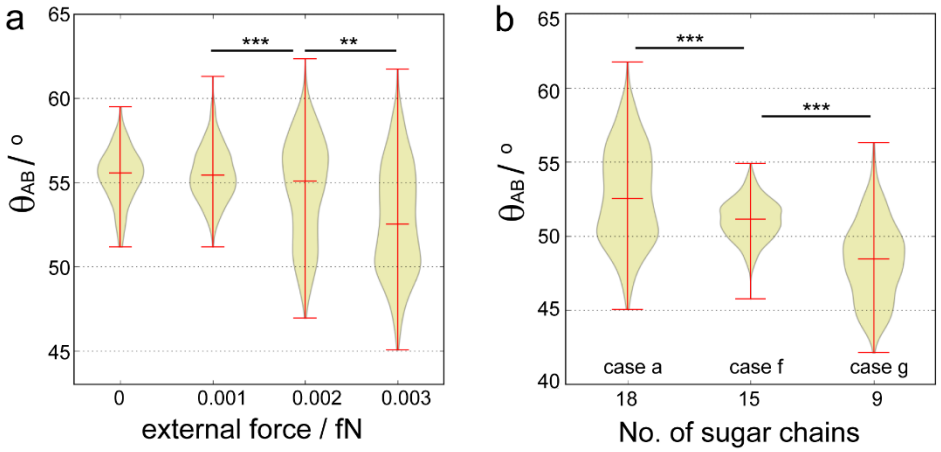

Figure 4-3 Changes of the transmembrane dimer chain under varying influence parameters. a. θ_{AB} changes under varying blood velocities in terms of external force. b. θ_{AB} changes under scenarios with the removed sugar chains. (**$p < 0.01$; ***$p < 0.001$)

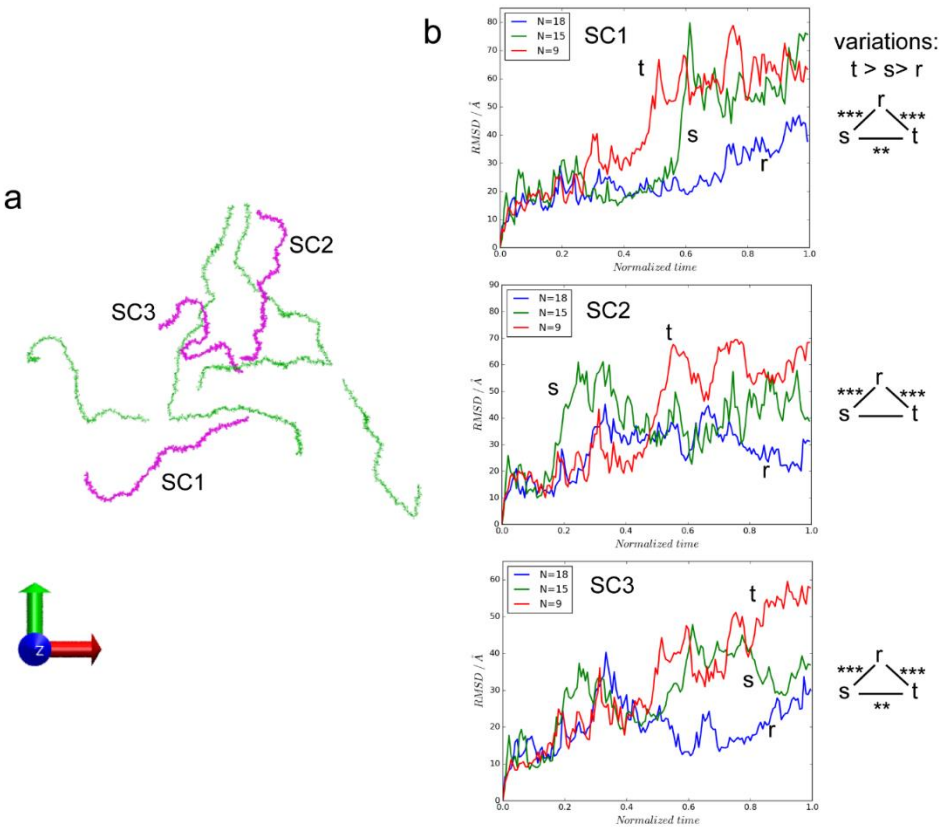

Figure 4-4 The root-mean-square-deviations (RMSDs) of the intact sugar chains of the central glycocalyx element. a. The intact sugar chains are marked in magenta. b. The RMSDs of the three sugar chains in three sugar-chain removed scenarios. N=18 (Case a) means no sugar chains removed, N=15 (Case f) refers to the scenario with the removal of the three sugar chains of the central glycocalyx element, and N=9 (Case g) represents the scenario with the removal of half number of the sugar chains. Generally, the surrounding sugar chains impede the movement of the central sugar chains, due to the small variations in the N=18 case. (*p < 0.05; **p < 0.01; ***p < 0.001 by F-test)

4.4 Mechanotransduction Pathway

Summarising the pathway gives that flow shear stress near the lipid bilayer wall is enhanced as flow passes through the soft and dendritic glycocalyx structures as discussed previously in Section 3.2. Under the enhanced shear stress, the two α-helix chains of the transmembrane dimer transmit the shear stress by scissor motion as well as via their bending. By closing the angle between the two transmembrane chains, forces with an order of magnitude of 10~100 pN are transmitted into the cytoplasm. The main function of the sugar chains is to protect the core protein from severe conformational changes by acting as resistance to flow and by confining the motions of the surrounding sugar chains. This process illustrates a typical mechanotransduction pathway via the glycocalyx in our body and is summarised in Figure 4-5.

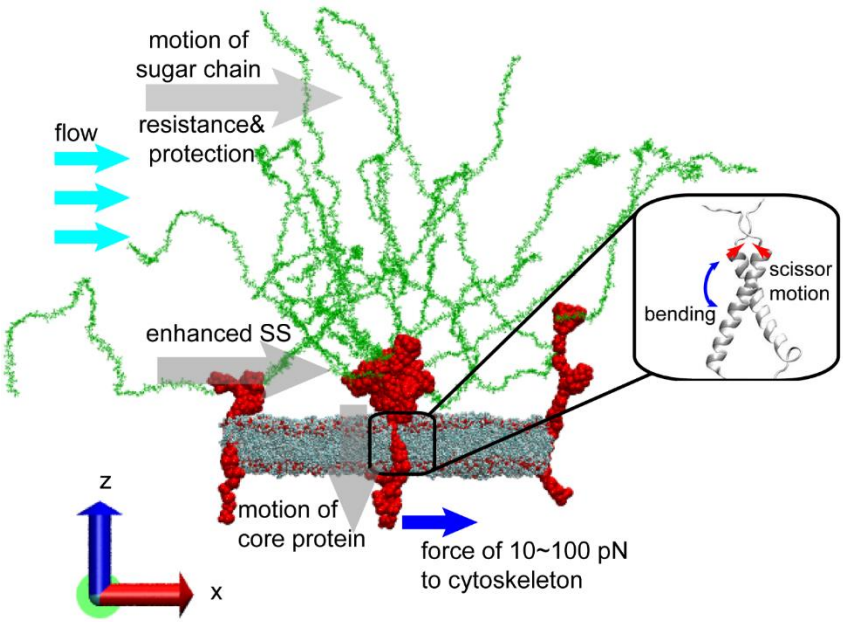

Figure 4-5 A typical mechanotransduction pathway via the glycocalyx in human body. Flow shear stress (SS) near the lipid bilayer wall is enhanced as flow passes through the soft and dendritic glycocalyx structures. Under the enhanced shear stress, the two α-helix chains of the transmembrane dimer transmit the shear stress by scissor motion as well as via their bending. By closing the angle between the two transmembrane chains, forces with an order of magnitude of 10~100 pN are transmitted into the cytoplasm. The main function of the sugar chains is to refrain the core protein from severe conformational changes by acting as resistance to flow and by confining the motions of the surrounding sugar chains.

4.5 Discussion

It is important to put these findings in context by discussing how they fit and elucidate the existing literature: The question of whether glycocalyx transmits force via the core proteins has long been

debatable. Weinbaum *et al*. [46] assumed the endothelial glycocalyx as a rigid body and predicted that torque would be generated on the cell membrane when flow passed the glycocalyx, and the torque can produce forces, thereby deforming the cytoskeleton. In accordance to this theory, the cytoskeletal deformation would be inhibited only when all the sugar chains of the glycocalyx were removed. However, experiments [47] suggested there was a threshold for the torque: 30% ~ 45% reduction of the glycocalyx sugar chains would inhibit cytoskeletal reorganisation. It would be difficult to clarify the existence of threshold if the glycocalyx were assumed as a rigid body, so experimental researchers postulated that transmission of forces might not occur through the rigid glycocalyx core protein. Actually, this discrepancy can be reconciled by the soft matter model proposed in this study. The ecto- and transmembrane subdomains of the core protein are physically connected by flexible coils. The flexibility of the linkage, on the other hand, can mediate forces from the ectodomain, which means forces can only be partially transmitted into the cytoskeleton. The mediation of the linkage explains the threshold discovered by the experiments. According to the *in silico* experiments, only by removing 16.7% of the sugar chains (3 out of 18 sugar chains are removed in Case f), the mechanotransduction in terms of scissor angular variations has been dramatically reduced by 55% (Figure 4-3b), which validated the existence of the proposed threshold. It is noteworthy that Case g indeed indicates an alternative force transmission pathway that flow shear stress is directly transmitted via

the core protein in the situation with a bulk of sugar chains removed, which has been mentioned in Section 3.4.3.

Previous theories usually linked the force transmission by glycocalyx with deformation of cell membranes [46, 47, 138]. However, the mechanism uncovered by this research implies that glycocalyx can alter the cytoskeleton via a scissor-like motion, without causing membrane deformation. Since membrane deformation normally affects membrane channel behaviour, the independence of force transmission by glycocalyx provides a therapeutic strategy for cardiovascular or renal diseases without causing side-effects from membrane channel malfunctions. The glycocalyx core protein dimer is therefore a promising avenue/target for treating cardiovascular diseases.

Chapter 5

5 Ion Transport through EG Layer and Improved Starling Principle

The objective of this chapter is to explore the response of the endothelial ion distribution to modification of two principal environmental parameters associated with cardiovascular diseases (i.e. change of blood velocity [109] and shedding of glycocalyx sugar chains [137]). Dynamics of the biomolecules and the surrounding ions (e.g. Na^+) are to be scrutinised. Based on the response, a further revision of the Starling principle considering changing blood flow velocity and glycocalyx configuration is to be proposed. In the discussion, the findings will be applied to predict the behaviour of other critical blood components, like red blood cells (RBCs).

To study the impact of blood flow velocity and shedding of sugar chains on ion transport, Cases a to d, f and g will be considered in this chapter.

5.1 Distribution of Na^+ molarity around the EG Layer

To investigate the Na^+ transport through the EGL, the spatial distribution of ions is a prerequisite. The glycocalyx features its negatively charged sugar chains in the ectodomain, and the charge distribution of the sugar chain residues in the intact system (Figure 5-1a) is illustrated in Figure 5-1b. To maintain a neutral system, in the region with rich sugar chains (below 42 nm in height), the initial Na^+ distribution along height (Figure 5-1c) is similar to its sugar residue charge counterpart but with positive charge. Figure 5-1c also indicates

that the Na^+ molarity (c_{wg}) near the lipid membrane region (e.g. h = 6 nm) prevails over that (c_f) above the sugar chain rich region (e.g. h = 46 nm). The prevalence continues further throughout the simulation as shown in Figure 5-2a.

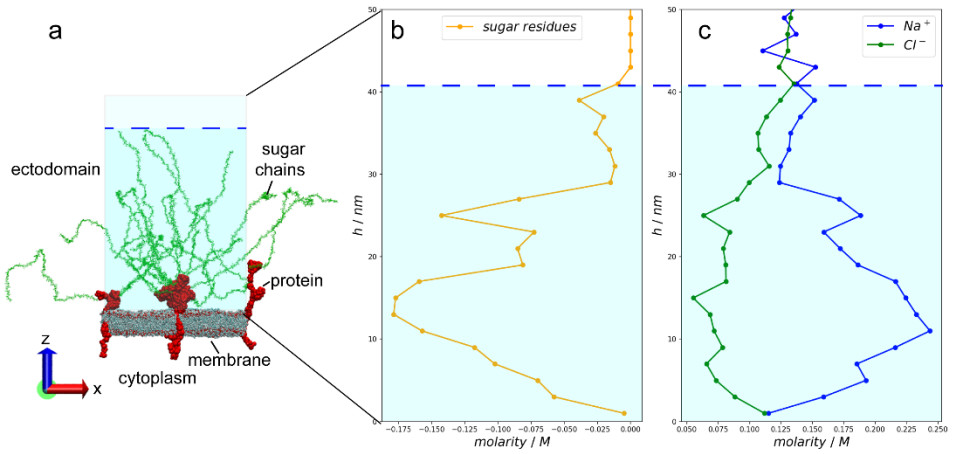

Figure 5-1 Initial configuration and charge distributions. a) Initial configuration of the intact glycocalyx system. b) and c) are initial charge distributions of the sugar chains and ions, respectively.

Figure 5-2b illustrates the Na^+ molarity differences ($\Delta c = c_{wg} - c_f$) in the two regions beneath and above the sugar chain rich area with normalized time (defined as the ratio of instantaneous time over the total time involved) under changing flow velocities via varying the values of external forces. The mean molarity difference value of the time series in the equilibrium (no flow) case is greater than its flow counterparts (p(0.003fN, no flow) < 0.005 and p(0.002fN, no flow) < 0.005). (Statistical details are provided in Appendix B) This phenomenon indicates that the flow facilitates the diffusion of Na^+ across the dendritic sugar chain area, and the facilitation is consistent

with the convection-diffusion transport phenomenon at macroscales [139].

The shedding of sugar chains is accomplished via reducing the number of sugar chains (i.e. Cases f and g). Due to the removal of the negatively charged sugar chains, the initial Na^+ distribution has been modified to maintain a neutral system. To facilitate comparison, a relative molarity difference is adopted to study the effects of sugar chain numbers on the ion transport. The relative molarity difference, $\underline{c}$, is defined as in Eq. (5-1).

$$\underline{c} = \frac{\Delta c - \Delta c_0}{\Delta c_0} = \frac{\Delta c}{\Delta c_0} - 1 \tag{5-1}$$

where Δc is the molarity difference as defined previously, and Δc_0 is the molarity difference at the start of every simulation. Figure 5-2c illustrates the relative molarity differences under situations with various numbers of sugar chains. The Na^+ molarity gradient orients from the lipid membrane to the flow regardless of whether the sugar chains are partially removed or not, for the value of relative molarity difference is greater than -1 for all the three situations. Furthermore, dramatic decreases in the molarity differences are also observed in the sugar chain reduced cases, for negative values of $\underline{c}$ are frequently observed during the time series (Distributions of signs for $\underline{c}$ values can be found in Appendix E). The negativity of $\underline{c}$ values implies an impairment in the functionality of the glycocalyx as a filter or buffer for Na^+ ions. Actually, the role of sugar chains in regulating the Na^+ motion is very reasonable if one could relate to an extreme scenario with the removal of all the sugar chains. If all the sugar chains were removed, the endogenous

molarity differences stemming from the inhomogeneous charge distributions of the sugar chains would disappear. Consequently, $\underline{c}$ would be a constant of -1 with no sugar chains.

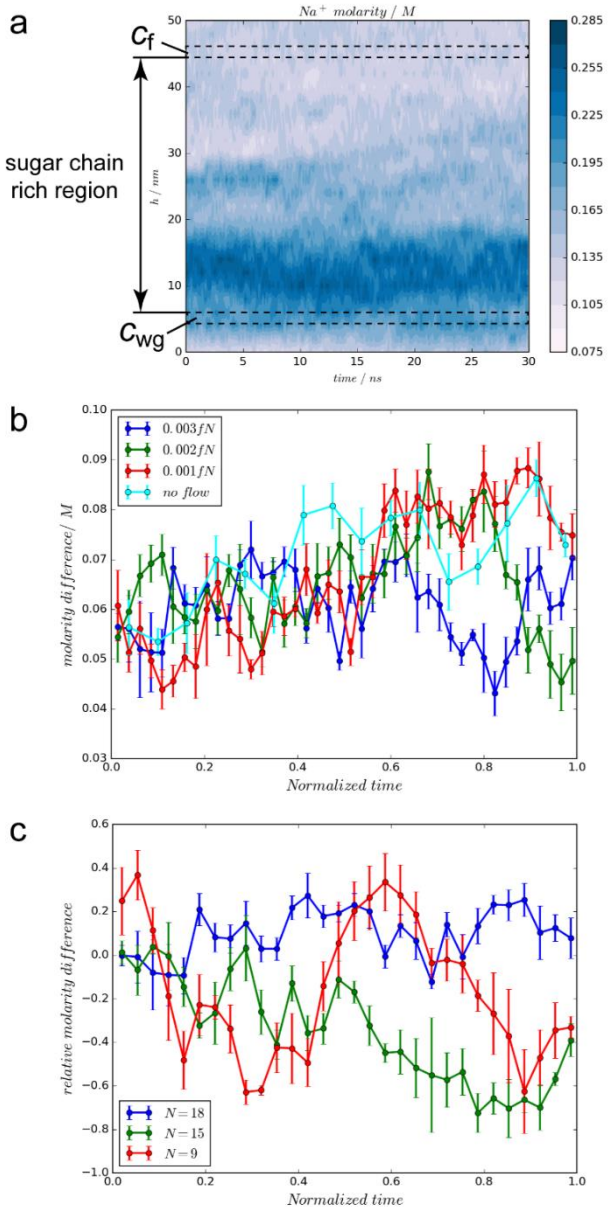

Figure 5-2 Distributions of Na^+ molarity and time-evolutions under different situations. a. Na^+ molarity distribution and evolution in the case with intact glycocalyx bearing 18 sugar chains under the external force of 0.003 fN for a physical time of 30 ns. b. Molarity differences, $\Delta c = c_{wg} - c_f$, under varying blood velocities resulting from varying external forces. c. Relative molarity differences in the scenario with reduced numbers of sugar chains.

5.2 Mechanism for flow impact on Na^+ transport

Figure 5-2b shows that the blood flow velocity affects the Na^+ ion transport. In Figure 5-2c, the influence on transport from the geometric configuration of sugar chains can also be partially attributed to the velocity change due to the reduction of sugar chains. Therefore, to reveal the mechanism of flow impact on Na^+ ion transport is to find out the manner via which flow affects the Na^+ behaviour.

5.2.1 Conformations and Interactions

Previous studies [90] and Section 3.3 suggest that flow modifies conformations of biomolecules (e.g. sugar chains). To elucidate whether the conformational changes influence Na^+ behaviour, two sugar chains with different initial conformations (Figure 5-3a) are selected from the no-flow case (Case d) and their interactions in terms of the coordination numbers (CNs) of surrounding Na^+ ions are examined. The CNs of the surrounding Na^+ ions are quantified by the numbers of heavy atoms (i.e. nitrogen, oxygen and phosphorous atoms) of the sugar chain residues within a cut-off distance of 2.5 Å around the Na^+ ions (The value of the cut-off distance is based on the radial distribution result shown in Appendix F). Time-evolutions of the average CNs of Na^+ are illustrated in Figure 5-3b, together with the probability density distributions in Figure 5-3c. The conformations of sugar chains are measured via a centre-to-centre vector ($\boldsymbol{R}_{\mathbf{ctc}}$) connecting the two centres of mass of a bisected sugar chain, which is reported effective in describing polymer rotational dynamics[140]. Three geometric parameters related to the vector $\boldsymbol{R}_{\mathbf{ctc}}$, as illustrated in Figure 5-3d, are used to depict the conformations of the two sugar

chains with their time-evolutions shown in Figure 5-3 e to g. As illustrated in Figure 5-3 e to g, the conformations of the two sugar chains vary in dissimilar patterns. Thus, it can be concluded that the sugar chain conformations affect the interactions between the Na^+ ions and sugar chains.

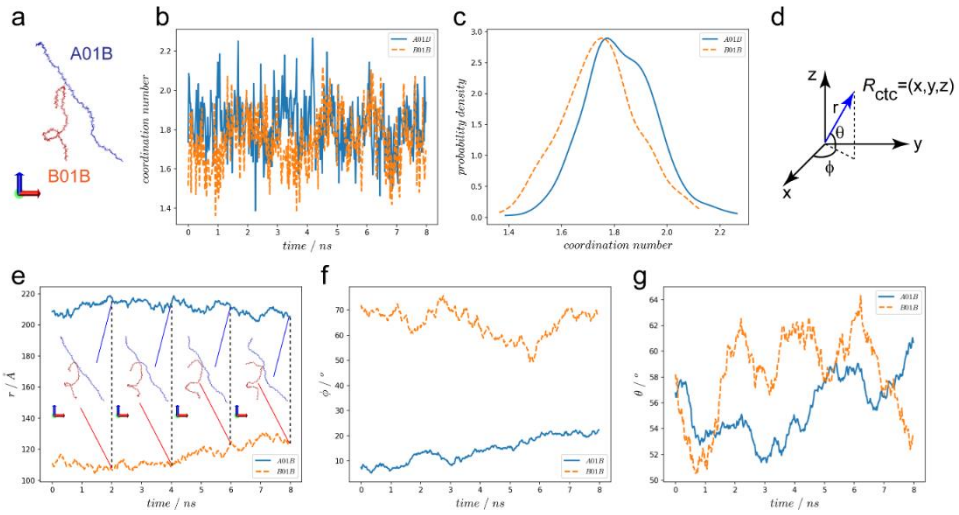

Figure 5-3 Coordination numbers of Na^+ and conformations of two sugar chains. a. Two sugar chains with different initial conformations. b. & c. Time-evolution and probability density distribution of the coordination numbers of Na^+ around the two sugar chains. d. Geometric parameters to depict the conformation of a sugar chain. e. to f. Time-evolutions of the two sugar chains in terms of the three geometric parameters.

The major conformational difference of the two sugar chains of interest (Figure 5-3a) resides in segments with corner shapes. To reveal how the corner shape affects the interaction between Na^+ and sugar chains, two segments with identical residue sequence but one featuring a corner shape and the other with a stretching shape are

selected as labelled in the inner panel of Figure 5-4a. The numbers of Na^+ around both segments throughout the no-flow simulation are recorded. The probability density distributions of the surrounding Na^+ numbers in Figure 5-4a suggest that the corner conformation of the sugar chain favours the accumulation of Na^+; by contrast, its stretching counterpart facilitates the movement of the Na^+. To further explore how the corner conformation accumulates Na^+, the residence rates of initial Na^+ ions around the corner and stretching conformations are calculated. The residence rate is calculated as

$$\text{residence rate} = \frac{n_{Na,j}}{n_{Na,0}} \tag{5-2}$$

In Eq. (5-2), $n_{Na,j}$ is the number of Na^+ ions retained from the initial frame of the simulation at the instant j, and $n_{Na,0}$ is the number of Na^+ ions at the initial frame of the simulation. As shown in Figure 5-4b, the higher residence rate of Na^+ in the corner case indicates that more ions stay around the corner sugar chain; therefore, the corner conformation accumulates Na^+ by confining the ions within its “realm”.

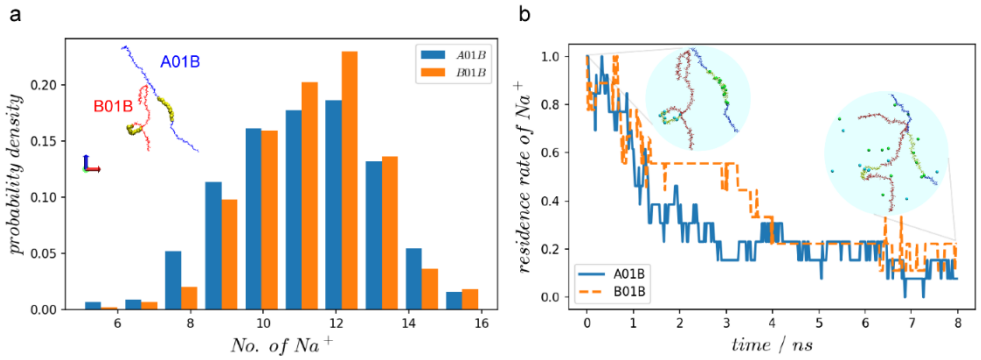

Figure 5-4 Probability density distributions of numbers of Na^+ around two segments, and residence rates of Na^+ around both segments. a. Probability density distributions of numbers of Na^+ around two segments with identical residue sequence but different conformations (highlighted yellow in the inner panel). b. Comparisons of residence rates of Na^+. The higher residence rate of Na^+ in the corner case suggests ions are confined by the corner conformation.

5.2.2 Flow and Na^+/Sugar-chain Interactions

As mentioned in Section 3.3, flow can stretch coils of sugar chains. Consequently, fewer corner structures are expected in flow cases. To further quantify the corner structures, an index— solvent accessible surface area (SASA) [141] — is calculated in individual cases. A larger value of average SASA per residue implies fewer corner structures within the sugar chains. As illustrated in Figure 5-5a, comparison of the average SASA values among the flow and the no-flow cases suggests a decreasing number of corners when flow passes by, as expected. Accordingly, fewer ions in the sugar-chain-rich region are observed in flow cases. In other words, more Na^+ ions are carried out

of the sugar-chain-rich region in the flow cases, which explains the smaller concentration differences of the flow cases (Figure 5-2b) from the perspective of the geometry.

Flow causes conformational changes of sugar chains thereby affecting the Na^+/sugar-chain interactions; on the other hand, it also breaks the equilibrium between Na^+ ions and sugar chains via transferring momentum to ions. Figure 5-5b displays two snapshots of the sugar chain conformations and velocity fields of the surrounding Na^+ ions in a fixed region of the simulation domain of Case a. As illustrated in Figure 5-5b, flow modifies the velocity fields of ions as it changes the conformations of sugar chains. As flow accelerates, the average SASA decreases (Figure 5-5a) which benefits the residence of Na^+ ions in the sugar-chain-rich region; however, the large impulse from water molecules on Na^+ can also facilitate the movement of ions resulting in the reduced residence rate of Na^+ around residues, thereby promoting the ion transport. (For example, in Figure 5-5 c and d the residence rates of Na^+ around sugar chain residues with different initial configurations decrease in the flow cases, which indicates that flow facilitates the motions of ions.) Therefore, the impact of flow velocity on ion transport is non-linear. A rough estimation shows that the order of magnitude of Na^+ hydration energy (~100 kcal/mol) is 100 times larger than the electrostatic interactions between Na^+ and sugar chains (~ kcal/mol). Thus, when flow accelerates, the impulse from water molecules dominates the ionic movements: water molecules collide and transfer momentum to ions, which encourages the *z*-direction motion of Na^+ thereby promoting the Na^+ transport.

Particularly, a negative correlation between the Na^+ molarity difference and flow velocity can be expected.

Indeed, the large impulse case (Case a) also geometrically primes the Na^+ transport. A scrutiny of three components of the vector $\boldsymbol{R}_{ctc}$ indicates that a large θ value is observed in the 0.003fN case (Figure 5-5e), and the large θ value can geometrically facilitate the ion transport out of the sugar-chain-region. Consequently, a declining number of Na^+ ions are observed in the sugar-chain-rich region as the external force increases (Figure 5-5f).

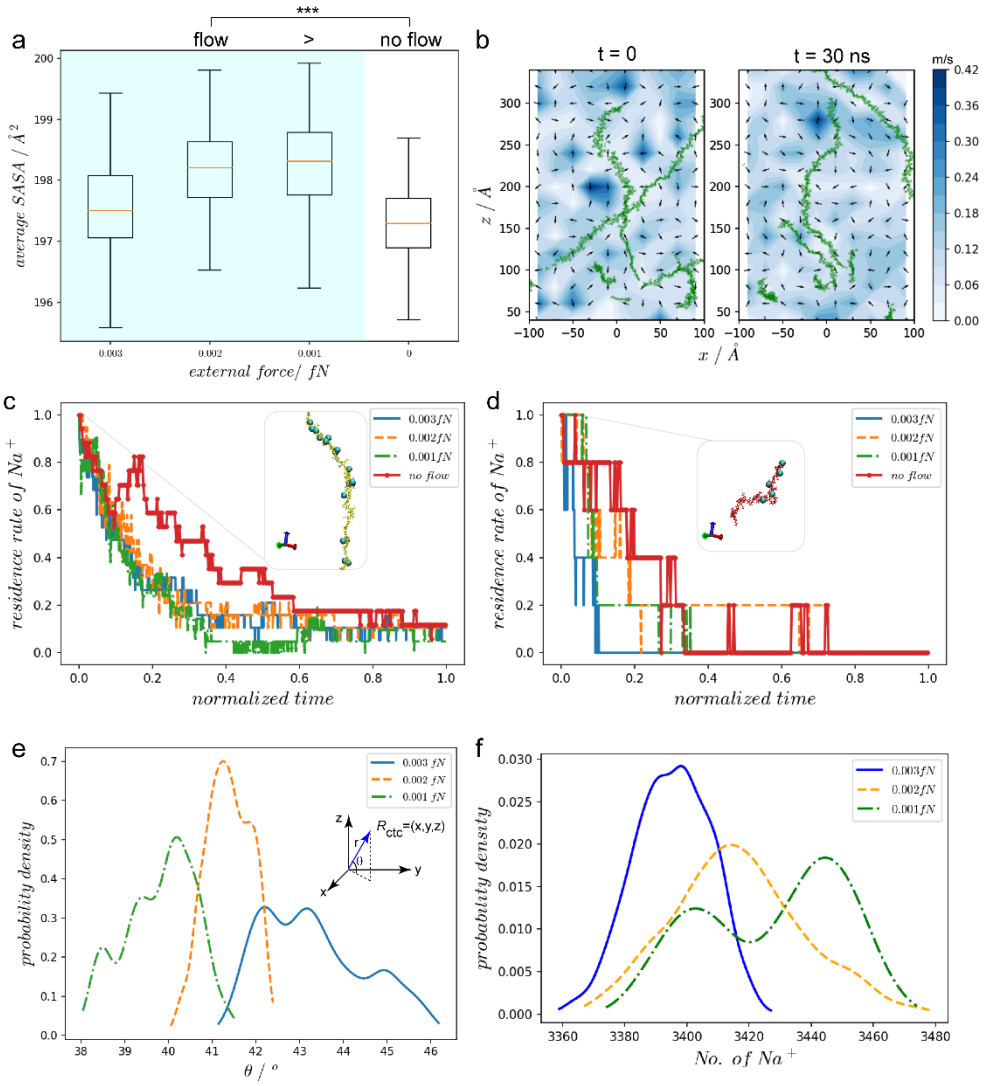

Figure 5-5 Flow impact on Na^+ ion transport. a. Average SASA values under varying flow conditions (*** P<0.001, and P-values can be found in Appendix B.); b. Snapshots of sugar chain conformations and Na^+ velocity fields at two different instants of Case a. c. θ value changes with the external forces. d. Number of Na^+ ions remaining in the sugar-chain-rich region under varying flow situations.

Summarizing the mechanism gives that flow velocity influences the ion transport via modifying sugar chain conformations as well as transferring momentum to ions. The conformational changes of sugar chains then affect the Na^+/sugar-chain interactions. The effects of flow

velocity on the interactions are non-linear. A schematic elucidating the mechanism is shown in Figure 5-6.

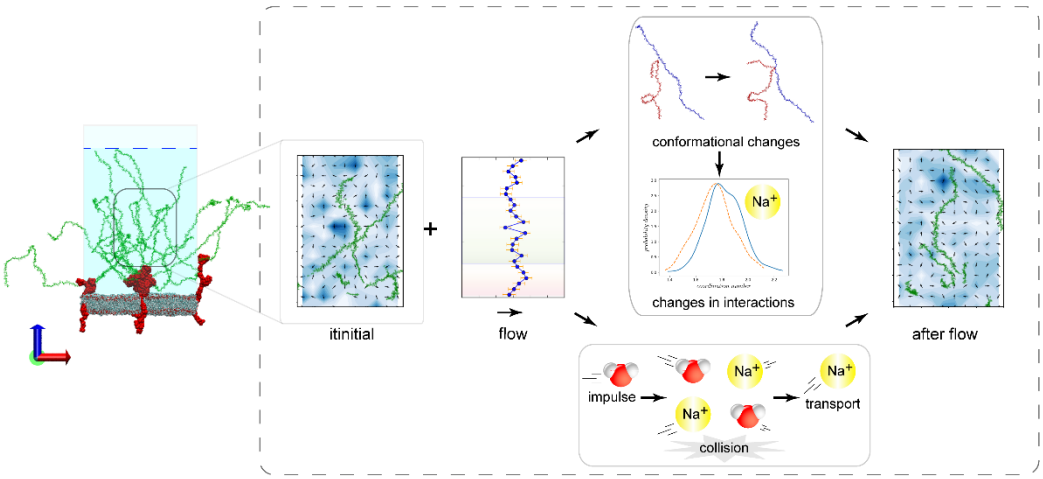

Figure 5-6 Schematic of the mechanism for flow impact on Na^+ transport. Flow influences the Na^+ transport via the conformational changes of sugar chains and transferring momentum to Na^+.

5.3 Improved Starling Principle

Considering the gradient of Na^+ ions around the EGL and the influence of flow velocities and sugar chain configurations, the filtration force in the revised Starling principle, as expressed by Eq. (1-4), for Na^+ ions is proposed to be in the form

$$\mathrm{FF} = \Delta P + \sigma(\Pi_g - \Pi_p)\gamma \tag{5-3}$$

In Eq. (5-3), γ is the revising coefficient for including the effects of flow velocity and sugar chain configuration, and is expected to be determined by

$$\gamma = \frac{\Delta c\left(\bar{v}_x, \rho_N\right)}{\Delta c\left(\bar{v}_x = 0, \rho_{N,\mathrm{intact}}\right)} \tag{5-4}$$

In Eq. (5-4), $\overline{v}_x$ is the bulk flow velocity of the blood, and ρ_N is the geometric density of sugar chains. For example, in this research, ρ_N is the ratio of the number of sugar chains to the area of lipid bilayer patch. In the equation, the numerator is the molarity difference under a certain flow velocity and a certain sugar chain configuration; the denominator is the molarity difference in equilibrium system with intact sugar chains.

To determine γ, the relation between the molarity difference and the blood flow velocity together with the geometric density of sugar chains needs to be established. Although Section 5.2 suggests a complicated effect of flow velocity on the sugar chain conformational changes, for simplification, linear relation is still assumed here. Indeed, raw data of Table 5-1 implies that linear relation is capable of describing the trend of the changing molarity differences with flow velocity and geometric density of sugar chains. Therefore, the molarity difference is expressed as:

$$\Delta c\left(\bar{v}_x, \rho_N\right) = a_0 + a_1 \bar{v}_x + a_2 \rho_N \tag{5-5}$$

In Eq. (5-5), a_0 is the intercept of the linear regression, and a_1 and a_2 are the coefficients for velocity and geometric configuration of sugar chains, respectively. For demonstration, the intercept and coefficients are calculated based on the raw data of the cases as listed in Table 5-1.

Table 5-1 Raw data of cases involved

case	Δc / M	v_x / m s^{-1}	ρ_N / nm^2
a	0.062	0.05555	18/820
b	0.065	0.09534	18/820
c	0.067	0.01530	18/820
d	0.071	-0.0035	18/820
f	0.026	0.3411	15/820
g	0.028	0.2240	9/820

Note: Δc is the average molarity difference in the time-evolution.

For linear regression of multiple variables, the intercept and coefficients are a_0 = 0.0336, a_1 = -0.1091 and a_2 = 1.6802, respectively. Incorporating these values into Eq. (5-4) and also assuming ρ_N being 18/820 nm^{-2} in this research is the normal physiological situation without the removal of any sugar chains give $\gamma = \frac{0.0336 - 0.1091\bar{v}_x + 1.6802\rho_N}{0.0705}$. As a rough estimation, the coefficient γ in Case a is 0.92, which means a physiological flow changes the Na^+ osmotic transport by 8% compared with a stationary Na^+ transport.

5.4 Discussion

The findings in this chapter indeed provide an alternative answer to the open-ended question “Why do we need to reduce salt intake and exercise regularly”.

Before answering the question, a phenomenon regarding the EGL and RBCs is worthy to elucidate: when RBCs flow through our vessels, an exclusion layer between the RBCs and EGL forms; the layer

thickness increases as RBCs accelerate [142]. The formation of the repulsive layer can be attributed to the repulsive interactions between RBCs and the EGL, as the surfaces of the RBCs are coated with negative charges. If extra salt, than suggested, is taken in, Na^+ may gather around the EGL and neutralise some of negative charges of the EGL, resulting in a decrease in repulsive interactions between RBCs and EGL and a decline in the thickness of the exclusion layer. In other words, sodium renders the endothelial cells “sticky” for RBCs, as observed in a recent experiment [143]. Therefore, to keep a low level of salt intake can benefit the smooth movement of the RBCs.

In accordance to the present results, a slightly faster blood velocity assists the transport of Na^+ ions to the outside of the EGL. Particularly, the number of Na^+ ions remaining in the EGL decreases, and the net negative charges in the EGL increase. Consequently, the repulsive interaction between RBCs and EGL is strengthened, leading to the thickness growth of the exclusion layer. The thickness increase then facilitates the smooth flowing of the RBCs which are closely bound with metabolism as is well known. Thus, regular exercise is beneficial for maintaining the normal operation of the body, as the blood velocity will slightly increase during exercise [144].

Chapter 6

6 Conclusions and Future Direction

6.1 Conclusions

In the present study, atomic events of the EG layers interacting with flow were investigated via a series of large-scale molecular dynamics simulations. This research is a pioneer study in which flow in the physiologically relevant range was accomplished based on an atomistic model of the glycocalyx with the to-date and detailed structural information. To reveal the mechanisms for the critical functions of the EG — mechanotransduction and ion transport buffer, the interacting dynamics of endothelial glycocalyx and flow was studied. Flow regime on complex surface was proposed based on results from a series of cases with varying surface configurations and flow velocities. Based on the dynamics of flow and biomolecules, an alternative force transmission pathway and mechanism for mechanotransduction of the endothelial glycocalyx were then established. Finally, the mechanism of flow impact on ion transport was investigated and improved Starling principle was proposed. The principal conclusions are as follows.

6.1.1 Coupled Dynamics of Flow and EG

The coupled dynamics of flow and endothelial glycocalyx show that the glycocalyx constituents swing and swirl when the flow passes by. The active motion of the glycocalyx, as a result, disturbs the flow by modifying the velocity distributions. By comparing the shear stress distributions in two cases with different glycocalyx configurations, the

research suggests that the glycocalyx controls the emergence of strong shear stresses.

Furthermore, the unsynchronised motion between the glycocalyx molecular constituents suggests an alternative force transmission pathway, i.e. force from the flow shear stress can be transmitted straightforwardly to the core protein and then to the cytoplasm without going to the sugar chains. The proposed force transmission pathway contributes to the understandings of mechanism for mechanotransduction of EG.

6.1.2 Mechanism for Mechanotransduction of EG

The dynamics of the glycocalyx constituents have proved that EG behaves in a soft-matter way, therefore a soft-matter model is proposed for studying the mechanotransduction via the EG. A scrutiny of the dynamics of the core protein indicates that the force from blood flow shear stress is transmitted via a scissor-like motion alongside the bending of the core protein. The force transmitted by the core protein has an order of magnitude of 10~ 100 pN. The function of EG sugar chains is to prevent severe conformational changes of the core protein by acting as resistance to flow and by confining the motions of the surrounding sugar chains. A complete pathway for mechanotransduction via the EG core protein is provided.

6.1.3 Ion Transport through EG Layer and Improved Starling Principle

Ion transport is affected by the changing velocities. Particularly, flow facilitates the diffusion of Na^+ across the dendritic sugar chain area. The mechanism for the effect is that flow modifies sugar chain

conformations and transfers momentum to ions. The conformational changes of sugar chains then affect the Na^+/sugar-chain interactions. The effects of flow velocity on the interactions are non-linear. Results show that the large impulse case has fewest Na^+ remained in the sugar-chain-rich region. Based on the mechanism, improved Starling principle has been established. An estimation in accordance to the further revised Starling principle suggests that a physiological flow changes the osmotic part of Na^+ transport by 8% compared with stationary transport.

6.2 Future Direction

In future work, the following aspects can be improved and extended.

6.2.1 Improvement on methodologies

6.2.1.1 Boundary Conditions

In the *in silico* setup, a fixed graphene layer was appended on the top of the system to eliminate the potential disturbance in micro-environment by water molecules as a result of the implementation of periodic boundary conditions. To give accurate analysis, the ectodomain in this study is carefully selected to ensure that it is far from the fixed graphene layer, because the fixed graphene layer may cause an artificial flow boundary layer which does not exist in reality. In further research, a velocity, consistent to that of the top region of the ectodomain, can be imposed to the graphene in order to diminish the influence of introducing the graphene layer. An open boundary can also be an alternative for this situation.

6.2.1.2 Advanced post-processing methods

The large system simulated have resulted in a colossal amount of data. Apart from the relationships or mechanisms reported in this research, many implicit relationships/mechanisms are still to be explored. To unveil these mechanisms, advanced data analysis methods, like machine learning or neutral network can be used in the future for deep exploration of the results. For example, by deploying machine learning or neutral network, the relation between the external force and the resulting bulk flow velocity may be clarified, which facilitates the establishment of an accurate flow regime diagram.

6.2.2 Extended work on the mechanotransduction

When blood flows on the endothelial cell surface, local deformation of lipid bilayer may also occur. Whether the deformation of lipid bilayer contributes to mechanotransduction and how it affects the functionality of EG are still unclear. Thus, attention can be paid to the behaviour of lipid bilayer, and the quantification of its contribution to mechanotransduction still needs further exploration.

6.2.3 Extended work on the research scales

Despite significant advances in computing capabilities on high-end computing, our MD simulations, though unprecedented, are still at nanoscales, leaving many questions concerning the multiscale multiphysics facets of the EGL unanswered. Based on the findings from this study, a Dissipate Particle Dynamics method or a coarse-grained MD can be used to cope with more complicated situations.

Appendices

Appendix A Velocity Estimation and Flow Type in EG Layer

The thickness of an endothelial glycocalyx layer is usually 50 to 500 nm, and in our cases the EGL is 50 nm high. Poiseuille's law is used to estimate the order of magnitude of the velocity for the EGL, and schematic for estimating the velocity is shown Figure A 1. For a pipe flow, the velocity (u) at a certain radius and the maximum velocity (u_{max}) follows $u / u_{max}=(R^2-r^2) / R^2$. Capillaries are taken as instance here. The radius of a capillary, R, is assumed to be 5 μm, and the average velocity in vessels u_{max} has an order of cm/s [112]. The EGL is assembled on the inner surface of the pipe with the radius of the apex to be 4.95 μm, so the orders of the velocities for EGLs in our cases are (0.01~0.1) cm/s.

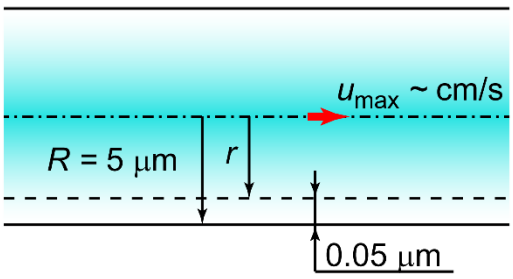

Figure A 1 Schematic for estimating the order of magnitude of velocities in the glycocalyx layer.

Reynolds number, Re, is defined as

$$\mathrm{Re}=\frac{\rho u l}{\mu} \qquad \text{(A1)}.$$

In Eq. (A1), ρ represents the fluid density, u represents the flow velocity, l represents the characteristic length and μ represents viscosity.

In this research, water density is 10^3 kg/m^3, the characteristic length is 50 nm, and viscosity of TIP3P water model is 0.321 mPa·s [125]. If the maximum flow velocity is smaller than 1 m/s under the external force of 0.003fN, incorporating these values then gives the estimation of Re to be far less than 100 (<< 10,000), so the flow is classified as laminar flow.

Appendix B Statistics of this Research

Table A 1 Tests and P-values used in this research

Figure	Samples	Tests	P-value
Figure 3-1	Var(x = 0, x = -8)	Bartlett	0.038
	Var(x = -4, x = -8)		0.030
Figure 3-2d	(v_{wg}, v_d)	K-S	0.06
	(v_d, v_f)		0.84
	(v_{wg}, v_f)		0.14
Figure 3-2e	Var(v_{wg}, v_d)	Fligner-Killeen (F-K)	1×10^{-6}
	Var(v_d, v_f)		2.9×10^{-5}
	Var(v_{wg}, v_f)		0.28
Figure 3-3a	(τ_{wg}, τ_d)	K-S	7×10^{-5}
	(τ_d, τ_f)		0.049
	(τ_{wg}, τ_f)		7×10^{-5}
Figure 3-3b	($\lvert\tau_{wg}\rvert$, $\lvert\tau_d\rvert$)	K-S	2×10^{-16}
	($\lvert\tau_d\rvert$, $\lvert\tau_f\rvert$)		0.0390
	($\lvert\tau_{wg}\rvert$, $\lvert\tau_f\rvert$)		5×10^{-9}
Figure 3-3d	one-dimer ($\lvert\tau_{wg}\rvert$, $\lvert\tau_f\rvert$)	K-S	2×10^{-5}
	one-dimer ($\lvert\tau_d\rvert$, $\lvert\tau_f\rvert$)		0.13
	one-dimer ($\lvert\tau_{wg}\rvert$, $\lvert\tau_d\rvert$)		8×10^{-9}
	$\lvert\tau_{wg}\rvert/\lvert\tau_f\rvert$ (1-dimer,3-dimer)	Chi-square	0.61
	$\lvert\tau_d\rvert/\lvert\tau_f\rvert$ (1-dimer,3-dimer)		0.71
Figure 4-2a	var(flow, control)	F-K	5×10^{-52}
Figure 4-3a	(0, 0.001)	F-K	0.1519
	(0.001, 0.002)		2.36×10^{-70}
	(0.002, 0.003)		0.0045
Figure 4-3b	(Case a, Case f)	F-K	1.65×10^{-103}
	(Case a, Case g)		5.72×10^{-14}
	(Case f, Case g)		1.72×10^{-52}
Figure 4-4b SC1	(r, s)	F-test (one-side)	1.64×10^{-11}
	(r, t)		1.51×10^{-22}
	(s, t)		0.09
Figure 4-4b SC2	(r, s)	F-test (one-side)	4.16×10^{-46}
	(r, t)		4.44×10^{-32}
	(s, t)		0.002
Figure 4-4b SC3	(r, s)	F-test (one-side)	1.05×10^{-40}
	(r, t)		0.98×10^{-33}
	(s, t)		0.009
Figure 5-2b	(0.003, 0)	T-test	0.17×10^{-9}
	(0.002, 0)		0.00023
	(0.001, 0)		0.0141
Figure 5-2c	(18, 15)	T-test	10^{-46}
	(18, 9)		10^{-16}
Figure 5-5a	(0.003, 0)	T-test	1.08×10^{-8}
	(0.002, 0)		1.23×10^{-63}
	(0.001, 0)		2.11×10^{-59}

Appendix C Still Water *In Silico* Experiment for Comparison

To verify whether the oscillating velocity profiles (Figure 3-1) stem from the presence of the glycocalyx or they are consequences of noises from the MD methods, a supplementary *in silico* experiment was conducted (referred to as a control) for comparison. In this experiment, an equilibrated system with only water molecules, ions and lipid membrane was selected as initial configuration (Figure A 2). All the water molecules are located above the lipid membrane. The dimension of the system is $135 \times 140 \times 375$ Å^3 with the height of water being 330 Å. The whole system comprises about 391,000 atoms. We conducted equilibrium simulations for 1 ns in NVT ensemble with the Lowe-Andersen thermostat as used in the flow simulation.

In the post-processing of the flow simulation, when the ectodomain was divided into 25 sub-layers (as shown in Figure 2-4a), each layer contains 40,000 to 50,000 water molecules. To be consistent with the flow simulation, we divided the water region of the control group into two layers each of which contains 38,000 to 43,000 water molecules. We then calculated the average *x*-direction velocities of both layers for each frame, followed by calculating the average velocity differences between the layers every 5 frames. Then, we obtained a distribution of the velocity differences of the control case.

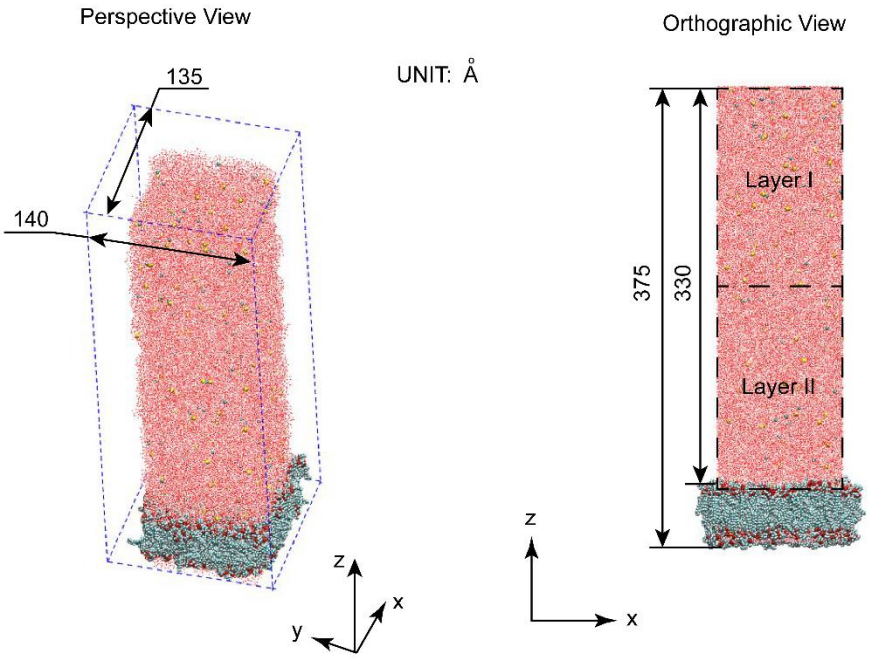

Figure A 2 Initial configuration of the control group and division of the water box.

Similarly, we calculated the velocity differences between two adjacent sub-layers in each sub-region of the flow system in the main cases, and averaged the velocity differences every 5 frames. Also, we obtained three distributions of the velocity differences for the three sub-regions.

Finally, we compare the distributions of velocity differences between the control group and every sub-region using Kolmogorov-Smirnov test, and the P-values are listed in Table A 2. The null hypothesis of the Kolmogorov-Smirnov test indicates that the two samples are drawn from the same distribution, so we can conclude that the oscillating velocity profile is not from MD noises, but mainly stems from the disturbance of the glycocalyx constituents.

Table A 2 P-values of Kolmogorov-Smirnov tests for the control and the flow simulations

Samples	P-values
(near wall, control)	0.004
(flow, control)	0.007
(dendritc, control)	0.004

Appendix D Geometric Derivation of the Changes between θ_A and θ_{AB}

Assuming the two chains of the dimer have the same length in the transmembrane region, and overlapping the centre of each chain then gives a circle with four ending points on its periphery, TA1, TA3, TB1 and TB3 (as shown in Figure A 3). The centre of the circle is TA2(TB2) and the radius is the distance between TA1 and TA2. The scissor angle between the two transmembrane chains, θ_{AB}, can be calculated by the angle $\angle$TA1_TA3_M as illustrated in Figure A 3, after line TB1-TB3 being parallelly moved from TB3 to TA3. When θ_A increases to θ_A' as flow passes by (the changes in θ_B can be neglected), θ_{AB} correspondingly changes to θ_{AB}'.

The difference between θ_{AB} and θ_{AB}' can be calculated by Eq. (D1).

$$\begin{aligned}\theta_{AB}-\theta_{AB}' &= \angle\text{TA1\_TA3\_M}-\angle\text{TA1}'\text{\_TA3\_M}\\ &= \angle\text{TA1\_TA3\_TA2}-\angle\text{TA1}'\text{\_TA3\_TA2}\end{aligned} \tag{D1}$$

By incorporating angle relations of triangles, Eq. (D1) can be rewritten as

$$\theta_{AB}-\theta_{AB}' = \frac{1}{2}\left(180^\circ-\theta_A\right)-\frac{1}{2}\left(180^\circ-\theta_A'\right)=\frac{1}{2}\left(\theta_A'-\theta_A\right) \tag{D2}$$

According to the simulation, θ_A increases by 2.9º, thus, the angle change of θ_A contributes 1.45º to the total angle change of θ_{AB}. The contribution rate of bending to the changes of θ_{AB} (3.1º) is 1.45/3.1=46.8%, thus, the scissor motion contributes 1-46.8%=53.2% to the change of θ_{AB}.

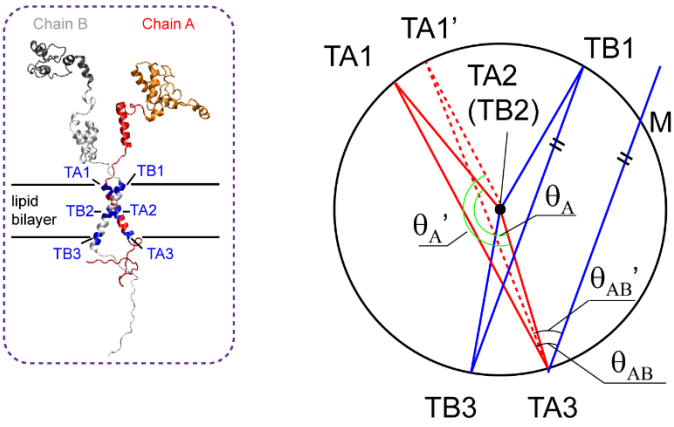

Figure A 3 Geometric relation of key transmembrane angles.

Appendix E Sign of the c Values

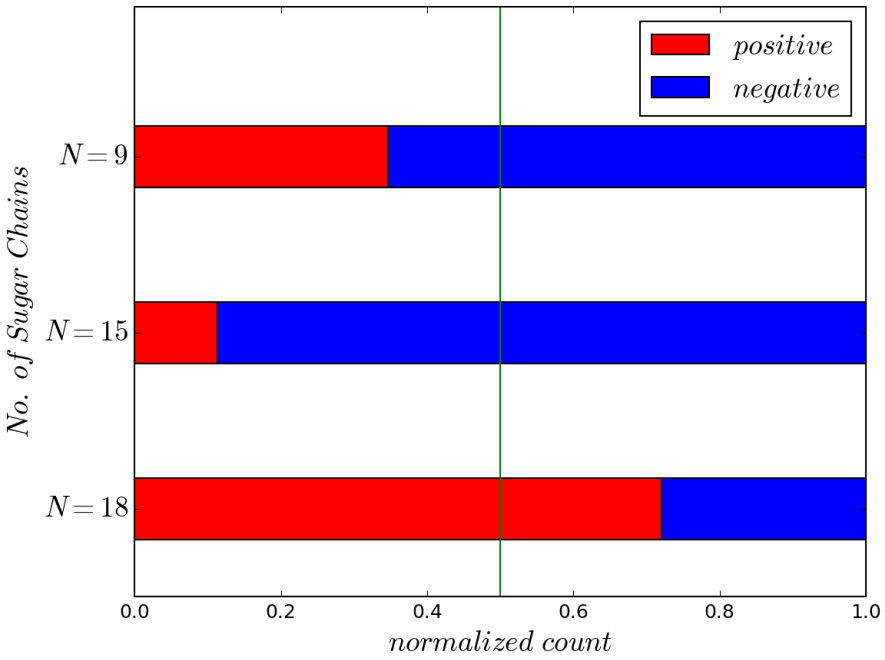

Figure A 4 Composition of the sign of c value in cases with various sugar chain numbers.

Appendix F Radial Distribution Function of Na^+ around Sugar Chains

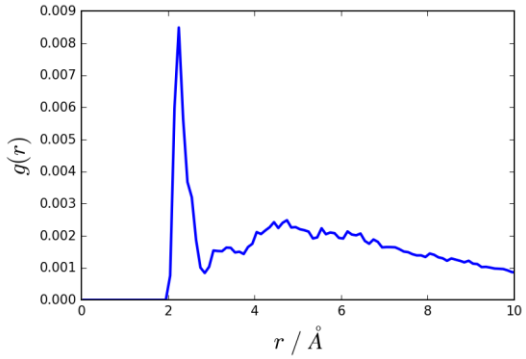

Figure A 5 Radial distribution function of Na^+ around sugar chains. The peaks value is reached around *r*=2.5 Å. Therefore, *r*=2.5 Å is selected as the cut-off distance to decide the coordination number of Na^+ as well as the neighbourhood of sugar chains.

References

1. Pries, A., T. Secomb, and P. Gaehtgens, *The endothelial surface layer.* Pflügers Arch, 2000. **440**(5): p. 653-666.
2. Nieuwdorp, M., et al., *The endothelial glycocalyx: a potential barrier between health and vascular disease.* Curr Opin Lipidol, 2005. **16**(5): p. 507-511.
3. Alphonsus, C. and R. Rodseth, *The endothelial glycocalyx: a review of the vascular barrier.* Anaesthesia, 2014. **69**(7): p. 777-784.
4. Reitsma, S., et al., *The endothelial glycocalyx: composition, functions, and visualization.* Pflugers Arch, 2007. **454**(3): p. 345-59.
5. Gouverneur, M., et al., *Vasculoprotective properties of the endothelial glycocalyx: effects of fluid shear stress.* J Intern Med, 2006. **259**(4): p. 393-400.
6. Schött, U., et al., *The endothelial glycocalyx and its disruption, protection and regeneration: a narrative review.* Scandinavian J Trauma, Resusc Emerg Med, 2016. **24**: p. 48.
7. Perrin, R.M., S.J. Harper, and D.O. Bates, *A Role for the Endothelial Glycocalyx in Regulating Microvascular Permeability in Diabetes Mellitus.* Cell Biochem Biophys, 2007. **49**(2): p. 65-72.
8. van den Berg, B.M., J.A. Spaan, and H. Vink, *Impaired glycocalyx barrier properties contribute to enhanced intimal low-density lipoprotein accumulation at the carotid artery bifurcation in mice.* Pflügers Arch, 2009. **457**(6): p. 1199-1206.
9. van den Berg, B.M., et al., *Atherogenic region and diet diminish glycocalyx dimension and increase intima-to-media ratios at murine carotid artery bifurcation.* Am J Physiol Heart Circ Physiol, 2006. **290**(2): p. H915-H920.
10. Rabelink, T.J. and D. de Zeeuw, *The glycocalyx—linking albuminuria with renal and cardiovascular disease.* Nat Rev Nephrol, 2015. **11**: p. 667.

11. Salmon, A.H. and S.C. Satchell, *Endothelial glycocalyx dysfunction in disease: albuminuria and increased microvascular permeability.* J Pathol, 2012. **226**(4): p. 562-74.
12. Satchell, S. and J. Tooke, *What is the mechanism of microalbuminuria in diabetes: a role for the glomerular endothelium?* Diabetologia, 2008. **51**(5): p. 714.
13. Singh, A., et al., *Glomerular endothelial glycocalyx constitutes a barrier to protein permeability.* J Am Soc Nephrol, 2007. **18**(11): p. 2885-2893.
14. Davies, P.F., *Flow-mediated endothelial mechanotransduction.* Physiol Rev, 1995. **75**(3): p. 519-560.
15. Tarbell, J.M. and M. Pahakis, *Mechanotransduction and the glycocalyx.* J Intern Med, 2006. **259**(4): p. 339-350.
16. Hahn, C. and M.A. Schwartz, *Mechanotransduction in vascular physiology and atherogenesis.* Nat Rev Mol Cell Biol, 2009. **10**(1): p. 53.
17. Desjardins, C. and B.R. Duling, *Heparinase treatment suggests a role for the endothelial cell glycocalyx in regulation of capillary hematocrit.* Am J Physiol Heart Circ Physiol, 1990. **258**(3): p. H647-H654.
18. VanTeeffelen, J.W., et al., *Endothelial glycocalyx: sweet shield of blood vessels.* Trends Cardiovasc Med, 2007. **17**(3): p. 101-105.
19. Belloni, P.N. and R.J. Tressler, *Microvascular endothelial cell heterogeneity: interactions with leukocytes and tumor cells.* Cancer Metastasis Rev, 1990. **8**(4): p. 353-389.
20. Weinbaum, S., J.M. Tarbell, and E.R. Damiano, *The Structure and Function of the Endothelial Glycocalyx Layer.* Ann Rev Biomed Eng, 2007. **9**(1): p. 121-167.
21. Rapraeger, A., *Transforming growth factor (type beta) promotes the addition of chondroitin sulfate chains to the cell surface proteoglycan (syndecan) of mouse mammary epithelia.* J Cell Biol, 1989. **109**(5): p. 2509-2518.

22. Mulivor, A.W. and H.H. Lipowsky, *Inflammation- and ischemia-induced shedding of venular glycocalyx.* Am J Physiol Heart Circ Physiol, 2004. **286**(5): p. H1672-H1680.
23. Esko, J.D. and S.B. Selleck, *Order out of chaos: assembly of ligand binding sites in heparan sulfate.* Annu Rev Biochem, 2002. **71**: p. 435-71.
24. Sugahara, K., et al., *Recent advances in the structural biology of chondroitin sulfate and dermatan sulfate.* Curr Opin Struct Biol, 2003. **13**(5): p. 612-620.
25. Pomin, V.H., *Keratan sulfate: An up-to-date review.* Int J Biol Macromol, 2015. **72**: p. 282-289.
26. Lee, J.Y. and A.P. Spicer, *Hyaluronan: a multifunctional, megaDalton, stealth molecule.* Curr Opin Cell Biol, 2000. **12**(5): p. 581-586.
27. Sarrazin, S., W.C. Lamanna, and J.D. Esko, *Heparan Sulfate Proteoglycans.* Cold Spring Harbor Perspectives in Biology, 2011. **3**(7): p. a004952.
28. Bishop, J.R., M. Schuksz, and J.D. Esko, *Heparan sulphate proteoglycans fine-tune mammalian physiology.* Nature, 2007. **446**(7139): p. 1030-1037.
29. Vuong, T.T., et al., *Syndecan-4 is a major syndecan in primary human endothelial cells in vitro, modulated by inflammatory stimuli and involved in wound healing.* J Histochem Cytochem, 2015. **63**(4): p. 280-92.
30. Teng, Y.H., R.S. Aquino, and P.W. Park, *Molecular functions of syndecan-1 in disease.* Matrix Biol, 2012. **31**(1): p. 3-16.
31. Elfenbein, A. and M. Simons, *Syndecan-4 signaling at a glance.* J Cell Sci, 2013. **126**(17): p. 3799-3804.
32. Baeyens, N., et al., *Syndecan 4 is required for endothelial alignment in flow and atheroprotective signaling.* Proc Natl Acad Sci U S A, 2014. **111**(48): p. 17308-17313.
33. Erlandsen, S.L., et al., *High-resolution visualization of the microbial glycocalyx with low-voltage scanning electron microscopy: dependence on cationic dyes.* J Histochem Cytochem, 2004. **52**(11): p. 1427-35.

34. Luft, J.H., *Fine Structure of Capillary and Endocapillary Layer as Revealed by Ruthenium Red.* Fed Proc, 1966. **25**(6p1): p. 1773-&.
35. Bruegger, D., et al., *Atrial natriuretic peptide induces shedding of endothelial glycocalyx in coronary vascular bed of guinea pig hearts.* Am J Physiol Heart Circ Physiol, 2005. **289**(5): p. H1993-9.
36. Chappell, D., et al., *The glycocalyx of the human umbilical vein endothelial cell: an impressive structure ex vivo but not in culture.* Circ Res, 2009. **104**(11): p. 1313-7.
37. Becker, B.F., D. Chappell, and M. Jacob, *Endothelial glycocalyx and coronary vascular permeability: the fringe benefit.* Basic Res Cardiol, 2010. **105**(6): p. 687-701.
38. van den Berg, B.M., H. Vink, and J.A. Spaan, *The endothelial glycocalyx protects against myocardial edema.* Circ Res, 2003. **92**(6): p. 592-4.
39. Dane, M.J.C., et al., *Glomerular Endothelial Surface Layer Acts as a Barrier against Albumin Filtration.* Am J Pathol, 2013. **182**(5): p. 1532-1540.
40. Dane, M.J., et al., *A microscopic view on the renal endothelial glycocalyx.* Am J Physiol Renal Physiol, 2015. **308**(9): p. F956-66.
41. Orr, A.W., et al., *Mechanisms of Mechanotransduction.* Dev Cell, 2006. **10**(1): p. 11-20.
42. Wang, N., J.D. Tytell, and D.E. Ingber, *Mechanotransduction at a distance: mechanically coupling the extracellular matrix with the nucleus.* Nat Rev Mol Cell Biol, 2009. **10**(1): p. 75-82.
43. Paluch, E.K., et al., *Mechanotransduction: use the force(s).* BMC Biology, 2015. **13**: p. 47.
44. Harris, A.R., P. Jreij, and D.A. Fletcher, *Mechanotransduction by the Actin Cytoskeleton: Converting Mechanical Stimuli into Biochemical Signals.* Ann Rev Biophys, 2018. **47**(1): p. 617-631.
45. Jaalouk, D.E. and J. Lammerding, *Mechanotransduction gone awry.* Nat Rev Mol Cell Biol, 2009. **10**(1): p. 63-73.

46. Weinbaum, S., et al., *Mechanotransduction and flow across the endothelial glycocalyx.* Proc Natl Acad Sci U S A, 2003. **100**(13): p. 7988-7995.
47. Thi, M.M., et al., *The role of the glycocalyx in reorganization of the actin cytoskeleton under fluid shear stress: a "bumper-car" model.* Proc Natl Acad Sci U S A, 2004. **101**(47): p. 16483-8.
48. Tarbell, J.M., S. Weinbaum, and R.D. Kamm, *Cellular fluid mechanics and mechanotransduction.* Ann Biomed Eng, 2005. **33**(12): p. 1719-23.
49. Pahakis, M.Y., et al., *The role of endothelial glycocalyx components in mechanotransduction of fluid shear stress.* Biochem Biophys Res Commun, 2007. **355**(1): p. 228-33.
50. Yao, Y., A. Rabodzey, and C.F. Dewey, Jr., *Glycocalyx modulates the motility and proliferative response of vascular endothelium to fluid shear stress.* Am J Physiol Heart Circ Physiol, 2007. **293**(2): p. H1023-30.
51. Tarbell, J.M. and E.E. Ebong, *The endothelial glycocalyx: a mechano-sensor and -transducer.* Sci Signal, 2008. **1**(40): p. pt8.
52. Dragovich, M.A., et al., *Mechanotransduction of the endothelial glycocalyx mediates nitric oxide production through activation of TRP channels.* Am J Physiol Cell Physiol, 2016. **311**(6): p. C846-C853.
53. Dragovich, M.A., et al., *Dual Regulation of L-Selectin-Mediated Leukocyte Adhesion by Endothelial Surface Glycocalyx.* Cell Mol Bioeng, 2016. **10**(1): p. 102-113.
54. McDonald, K.K., et al., *Glycocalyx Degradation Induces a Proinflammatory Phenotype and Increased Leukocyte Adhesion in Cultured Endothelial Cells under Flow.* PLoS One, 2016. **11**(12): p. e0167576.
55. Curry, F.R.E. and R.H. Adamson, *Vascular permeability modulation at the cell, microvessel, or whole organ level: towards closing gaps in our knowledge.* Cardiovasc Res, 2010. **87**(2): p. 218-229.

56. Tarbell, J.M., *Shear stress and the endothelial transport barrier.* Cardiovasc Res, 2010. **87**(2): p. 320-30.
57. Curry, F.E. and R.H. Adamson, *Endothelial glycocalyx: permeability barrier and mechanosensor.* Ann Biomed Eng, 2012. **40**(4): p. 828-39.
58. Levick, J.R. and C.C. Michel, *Microvascular fluid exchange and the revised Starling principle.* Cardiovasc Res, 2010. **87**(2): p. 198-210.
59. Hu, X. and S. Weinbaum, *A new view of Starling's hypothesis at the microstructural level.* Microvasc Research, 1999. **58**(3): p. 281-304.
60. Hu, X., et al., *Starling forces that oppose filtration after tissue oncotic pressure is increased.* Am J PhysiolHeart Circ Physiol, 2000. **279**(4): p. H1724-H1736.
61. Adamson, R., et al., *Oncotic pressures opposing filtration across non‐fenestrated rat microvessels.* J Physiol, 2004. **557**(3): p. 889-907.
62. Ogston, A.G., *The Spaces in a Uniform Random Suspension of Fibres.* Trans Faraday Soc, 1958. **54**(11): p. 1754-1757.
63. Peters, W., et al., *Nanomechanics and sodium permeability of endothelial surface layer modulated by hawthorn extract WS 1442.* PLoS One, 2012. **7**(1): p. e29972.
64. Lawrence, M.G., et al., *Permeation of macromolecules into the renal glomerular basement membrane and capture by the tubules.* Proc Natl Acad Sci U S A, 2017. **114**(11): p. 2958-2963.
65. Tarbell, J.M. and Z.D. Shi, *Effect of the glycocalyx layer on transmission of interstitial flow shear stress to embedded cells.* Biomech Model Mechanobiol, 2013. **12**(1): p. 111-21.
66. Dabagh, M., et al., *Shear-induced force transmission in a multicomponent, multicell model of the endothelium.* J R Soc Interface, 2014. **11**(98): p. 20140431.
67. Zeng, Y., et al., *A three-dimensional random network model of the cytoskeleton and its role in mechanotransduction and nucleus deformation.* Biomech Model Mechanobiol, 2012. **11**(1): p. 49-59.

68. Dabagh, M., et al., *Mechanotransmission in endothelial cells subjected to oscillatory and multi-directional shear flow.* J R Soc Interface, 2017. **14**(130).
69. Fedosov, D.A., et al., *Predicting human blood viscosity in silico.* Proc Natl Acad Sci U S A, 2011. **108**(29): p. 11772-7.
70. Li, X., A.S. Popel, and G.E. Karniadakis, *Blood–plasma separation in Y-shaped bifurcating microfluidic channels: a dissipative particle dynamics simulation study.* Phys Biol, 2012. **9**(2): p. 026010.
71. Fedosov, D.A., B. Caswell, and G.E. Karniadakis, *A multiscale red blood cell model with accurate mechanics, rheology, and dynamics.* Biophys J, 2010. **98**(10): p. 2215-2225.
72. Spenley, N., *Scaling laws for polymers in dissipative particle dynamics.* Europhys Lett, 2000. **49**(4): p. 534.
73. Gibson, J.B., et al., *Simulation of colloid-polymer systems using dissipative particle dynamics.* Mol Simulat, 1999. **23**(1): p. 1-41.
74. Jiang, W., et al., *Hydrodynamic interaction in polymer solutions simulated with dissipative particle dynamics.* J Chem Phys, 2007. **126**(4): p. 044901.
75. Kreer, T., *Polymer-brush lubrication: a review of recent theoretical advances.* Soft Matter, 2016. **12**(15): p. 3479-3501.
76. Español, P. and P.B. Warren, *Perspective: Dissipative particle dynamics.* J Chem Phys, 2017. **146**(15): p. 150901.
77. Deng, M., et al., *Simulation and modelling of slip flow over surfaces grafted with polymer brushes and glycocalyx fibres.* J Fluid Mech, 2012. **711**.
78. Sattelle, B.M., J. Shakeri, and A. Almond, *Does Microsecond Sugar Ring Flexing Encode 3D-Shape and Bioactivity in the Heparanome?* Biomacromolecules, 2013. **14**(4): p. 1149-1159.
79. Eriksson, M., T.K. Lindhorst, and B. Hartke, *Differential effects of oligosaccharides on the hydration of simple cations.* J Chem Phys, 2008. **128**(10): p. 105105.
80. Faller, C.E. and O. Guvench, *Sulfation and cation effects on the conformational properties of the glycan backbone of chondroitin*

sulfate disaccharides. J Phys Chem B, 2015. **119**(20): p. 6063-73.

81. Babik, S., S.A. Samsonov, and M.T. Pisabarro, *Computational drill down on FGF1-heparin interactions through methodological evaluation.* Glycoconj J, 2017. **34**(3): p. 427-440.
82. Huang, Y., et al., *Mechanistic study on electron capture dissociation of the oligosaccharide-Mg(2)(+) complex.* J Am Soc Mass Spectrom, 2014. **25**(8): p. 1451-60.
83. Gehrcke, J.-P. and M.T. Pisabarro, *Identification and characterization of a glycosaminoglycan binding site on interleukin-10 via molecular simulation methods.* J Mol Graph Model, 2015. **62**: p. 97-104.
84. Ruiz Hernandez, S.E., I. Streeter, and N.H. de Leeuw, *The effect of water on the binding of glycosaminoglycan saccharides to hydroxyapatite surfaces: a molecular dynamics study.* Phys Chem Chem Phys, 2015. **17**(34): p. 22377-88.
85. Ng, C., P. Nandha Premnath, and O. Guvench, *Rigidity and flexibility in the tetrasaccharide linker of proteoglycans from atomic-resolution molecular simulation.* J Comput Chem, 2017. **38**(16): p. 1438-1446.
86. Ham, H.O., et al., *Antifouling Glycocalyx-Mimetic Peptoids.* J Am Chem Soc, 2013. **135**(35): p. 13015-13022.
87. Huang, T.Y., et al., *Structure of the Complex between a Heparan Sulfate Octasaccharide and Mycobacterial Heparin-Binding Hemagglutinin.* Angew Chem Int Ed, 2017. **56**(15): p. 4192-4196.
88. Sousa, R.P., et al., *Insights into the reaction mechanism of 3-O-sulfotransferase through QM/MM calculations.* Phys Chem Chem Phys, 2016. **18**(16): p. 11488-11496.
89. Cruz-Chu, E.R., et al., *Structure and response to flow of the glycocalyx layer.* Biophys J, 2014. **106**(1): p. 232-43.
90. Pikoula, M., et al., *Oligosaccharide model of the vascular endothelial glycocalyx in physiological flow.* Microfluid Nanofluidics, 2018. **22**(2): p. 21.

91. Frenkel, D. and B. Smit, *Understanding Molecular Simulation: From Algorithms to Applications*. 2002: Academic Press, 2001.
92. Rapaport, D.C., *The Art of Molecular Dynamics Simulation*. 2004: Cambridge University Press. 564.
93. Karplus, M. and J.A. McCammon, *Molecular dynamics simulations of biomolecules.* Nat Struct Mol Biol, 2002. **9**(9): p. 646-652.
94. Grotendorst, J., D. Marx, and A. Muramatsu, *Quantum simulations of complex many-body systems: from theory to algorithms.* NIC series, 2002. **10**: p. 211-254.
95. MacKerell, A.D., et al., *All-atom empirical potential for molecular modeling and dynamics studies of proteins.* J Phys Chem B, 1998. **102**(18): p. 3586-3616.
96. Nakamoto, K., *The Urey—Bradley Force Field: Its Significance and Application*, in *Developments in Applied Spectroscopy*. 1964, Springer. p. 158-168.
97. Allen, M.P.A. and D.J. Tildesley, *Computer Simulation of Liquids*. 1987, New York: Oxford University Press.
98. Jiang, X.Z., et al., *Large-scale molecular dynamics simulation of flow under complex structure of endothelial glycocalyx.* Comput Fluids, 2018. **173**: p. 140-146.
99. Thomas, M. and B. Corry, *Thermostat choice significantly influences water flow rates in molecular dynamics studies of carbon nanotubes.* Microfluid Nanofluidics, 2015. **18**(1): p. 41-47.
100. Basconi, J.E. and M.R. Shirts, *Effects of Temperature Control Algorithms on Transport Properties and Kinetics in Molecular Dynamics Simulations.* J Chem Theory Comput, 2013. **9**(7): p. 2887-99.
101. Krishnan, T.V.S., J.S. Babu, and S.P. Sathian, *A molecular dynamics study on the effect of thermostat selection on the physical behavior of water molecules inside single walled carbon nanotubes.* J Mol Liquids, 2013. **188**: p. 42-48.
102. Berendsen, H.J.C., et al., *Molecular-Dynamics with Coupling to an External Bath.* J Chem Phys, 1984. **81**(8): p. 3684-3690.

103. Kotsalis, E.M., J.H. Walther, and P. Koumoutsakos, *Multiphase water flow inside carbon nanotubes.* Int J Multiphase Flow, 2004. **30**(7-8): p. 995-1010.
104. Nicholls, W.D., et al., *Water transport through (7,7) carbon nanotubes of different lengths using molecular dynamics.* Microfluid Nanofluidics, 2012. **12**(1-4): p. 257-264.
105. Hummer, G., J.C. Rasaiah, and J.P. Noworyta, *Water conduction through the hydrophobic channel of a carbon nanotube.* Nature, 2001. **414**(6860): p. 188-190.
106. Lowe, C.P., *An alternative approach to dissipative particle dynamics.* Europhys Lett, 1999. **47**(2): p. 145-151.
107. Koopman, E.A. and C.P. Lowe, *Advantages of a Lowe-Andersen thermostat in molecular dynamics simulations.* J Chem Phys, 2006. **124**(20): p. 204103.
108. Delle Site, L. and M. Praprotnik, *Molecular systems with open boundaries: Theory and simulation.* Phys Rep, 2017. **693**: p. 1-56.
109. Tarbell, J.M., S.I. Simon, and F.R.E. Curry, *Mechanosensing at the Vascular Interface.* Annu Rev Biomed Eng, Vol 16, 2014. **16**: p. 505-532.
110. Jiang, X.Z., et al., *Large-scale molecular dynamics simulation of coupled dynamics of flow and glycocalyx: towards understanding atomic events on an endothelial cell surface.* J R Soc Interface, 2017. **14**(137).
111. Jiang, X.Z., et al., *Regimes of Flow over Complex Structures of Endothelial Glycocalyx: A Molecular Dynamics Simulation Study.* Sci Rep, 2018. **8**(1): p. 5732.
112. Yamamoto, T., et al., *Blood velocity profiles in the human renal artery by Doppler ultrasound and their relationship to atherosclerosis.* Arter Thromb Vasc Biol, 1996. **16**(1): p. 172-177.
113. Gabe, I.T., et al., *Measurement of Instantaneous Blood Flow Velocity and Pressure in Conscious Man with a Catheter-Tip Velocity Probe.* Circulation, 1969. **40**(5): p. 603-614.

114. Hartley, C.J., et al., *Doppler velocity measurements from large and small arteries of mice.* Am J Physiol Heart Circ Physiol, 2011. **301**(2): p. H269-H278.
115. Phillips, J.C., et al., *Scalable molecular dynamics with NAMD.* J Computat Chem, 2005. **26**(16): p. 1781-1802.
116. Humphrey, W., A. Dalke, and K. Schulten, *VMD: Visual molecular dynamics.* J Mol Graph Model, 1996. **14**(1): p. 33-38.
117. Vega, C. and J.L.F. Abascal, *Simulating water with rigid non-polarizable models: a general perspective.* Phys Chem Chem Phys, 2011. **13**(44): p. 19663-19688.
118. Ouyang, J.F. and R.P. Bettens, *Modelling Water: A Lifetime Enigma.* Chimia (Aarau), 2015. **69**(3): p. 104-11.
119. Jorgensen, W.L., et al., *Comparison of simple potential functions for simulating liquid water.* J Chem Phys, 1983. **79**(2): p. 926-935.
120. Mark, P. and L. Nilsson, *Structure and Dynamics of the TIP3P, SPC, and SPC/E Water Models at 298 K.* J Phys Chem A, 2001. **105**(43): p. 9954-9960.
121. Vega, C. and E. de Miguel, *Surface tension of the most popular models of water by using the test-area simulation method.* J Chem Phys, 2007. **126**(15): p. 154707.
122. Darden, T., D. York, and L. Pedersen, *Particle mesh Ewald: An N·log(N) method for Ewald sums in large systems.* J Chem Phys, 1993. **98**(12): p. 10089-10092.
123. Miyamoto, S. and P.A. Kollman, *Settle - an Analytical Version of the Shake and Rattle Algorithm for Rigid Water Models.* J Comput Chem, 1992. **13**(8): p. 952-962.
124. Weyl, H., *On the differential equations of the simplest boundary-layer problems.* Ann Math, 1942. **43**: p. 381-407.
125. Angel Gonzalez, M. and J.L.F. Abascal, *The shear viscosity of rigid water models.* J Chem Phys, 2010. **132**(9).
126. Bakan, A., L.M. Meireles, and I. Bahar, *ProDy: protein dynamics inferred from theory and experiments.* Bioinformatics, 2011. **27**(11): p. 1575-7.

127. Izrailev, S., et al., *Steered molecular dynamics*, in *Computational molecular dynamics: challenges, methods, ideas*. 1999, Springer. p. 39-65.
128. Isralewitz, B., M. Gao, and K. Schulten, *Steered molecular dynamics and mechanical functions of proteins.* Curr Opin Struct Biol, 2001. **11**(2): p. 224-230.
129. Lu, H. and K. Schulten, *Steered molecular dynamics simulations of force-induced protein domain unfolding.* Protein Struct Funct Bioinformatics, 1999. **35**(4): p. 453-463.
130. del Rio, A., et al., *Stretching Single Talin Rod Molecules Activates Vinculin Binding.* Science, 2009. **323**(5914): p. 638-641.
131. Lara, C., et al., *Sub-Persistence-Length Complex Scaling Behavior in Lysozyme Amyloid Fibrils.* Phys Rev Lett, 2011. **107**(23): p. 238101.
132. Block, J., et al., *Nonlinear Loading-Rate-Dependent Force Response of Individual Vimentin Intermediate Filaments to Applied Strain.* Phys Rev Lett, 2017. **118**(4): p. 048101.
133. Rief, M., et al., *Reversible unfolding of individual titin immunoglobulin domains by AFM.* Science, 1997. **276**(5315): p. 1109-12.
134. Staple, D.B., et al., *Model for Stretching and Unfolding the Giant Multidomain Muscle Protein Using Single-Molecule Force Spectroscopy.* Phys Rev Lett, 2008. **101**(24).
135. Kamm, R.D. and M.R. Kaazempur-Mofrad, *On the molecular basis for mechanotransduction.* Mech Chem Biosyst, 2004. **1**(3): p. 201-9.
136. Oberhauser, A.F., et al., *Stepwise unfolding of titin under force-clamp atomic force microscopy.* Proc Natl Acad Sci U S A, 2001. **98**(2): p. 468-72.
137. Cruickshank, K., et al., *Aortic pulse-wave velocity and its relationship to mortality in diabetes and glucose intoleranc: an integrated index of vascular function?* Circulation, 2002. **106**(16): p. 2085-90.

138. Sabass, B. and H.A. Stone, *Role of the Membrane for Mechanosensing by Tethered Channels.* Phys Rev Lett, 2016. **116**(25): p. 258101.
139. Perl, W. and F.P. Chinard, *A Convection-Diffusion Model of Indicator Transport through an Organ.* Circ Res, 1968. **22**(2): p. 273-298.
140. Kim, J.M. and C. Baig, *Precise Analysis of Polymer Rotational Dynamics.* Sci Rep, 2016. **6**: p. 19127.
141. Marsh, J.A. and S.A. Teichmann, *Relative Solvent Accessible Surface Area Predicts Protein Conformational Changes upon Binding.* Structure(London, England:1993), 2011. **19**(6): p. 859-867.
142. Vink, H. and B.R. Duling, *Identification of distinct luminal domains for macromolecules, erythrocytes, and leukocytes within mammalian capillaries.* Circ Res, 1996. **79**(3): p. 581-589.
143. Oberleithner, H., M. Walte, and K. Kusche-Vihrog, *Sodium renders endothelial cells sticky for red blood cells.* Front Physiol, 2015. **6**: p. 188.
144. Lott, M.E., et al., *Effects of dynamic exercise on mean blood velocity and muscle interstitial metabolite responses in humans.* Am J Physiol Heart Circ Physiol, 2001. **281**(4): p. H1734-41.

Publications Derived from This Study

Journal papers

[1] **Xi Zhuo Jiang**, Haipeng Gong, Kai H. Luo, Yiannis Ventikos. Large -Scale Molecular *Dynamics Simulation of Coupled Dynamics of Flow and Glycocalyx: Towards Understanding Atomic Events on Endothelial Cell Surface.* Journal of the Royal Society Interface 2017; 14: 20170780. DOI: 10.1098/rsif.2017.0780

[2] **Xi Zhuo Jiang,** Muye Feng, Yiannis Ventikos, Kai H. Luo. *Large-Scale Molecular Dynamics Simulation of Flow Under Complex Structure of Endothelial Glycocalyx.* Computers and Fluids. DOI: 10.1016/j.compfluid.2018.03.014

[3] **Xi Zhuo Jiang,** Muye Feng, Yiannis Ventikos, Kai H. Luo. *Regimes of Flow Over Complex Structures of Endothelial Glycocalyx: A Molecular Dynamics Simulation Study.* Scientific Reports 2018; 8:5732. DOI: 10.1038/s41598-018-24041-7

Papers in progress

[4] **Xi Zhuo Jiang**, Haipeng Gong, Kai H. Luo, Yiannis Ventikos. *Scissor-like Motion as the Principal Mode of Mechanotransduction for the Endothelial Glycocalyx.* (submission in progress)

[5] **Xi Zhuo Jiang**, Yiannis Ventikos, Kai H. Luo. *Microvascular ion transport through endothelial glycocalyx layer: new mechanism and improved Starling principle.* Physical Chemistry Chemical Physics. (under review)

[6] **Xi Zhuo Jiang**, Kai H. Luo, Yiannis Ventikos. *Reducing Salt Intake and Exercising Regularly: Implications from Molecular Dynamics Simulations of Endothelial Glycocalyx.* Frontiers in Physiology (revision under review)

[7] **Xi Zhuo Jiang**, Yufang Lu, Kai H. Luo, Yiannis Ventikos. *Understanding Endothelial Glycocalyx Function Under Flow Shear Stress from a Molecular Perspective.* Biorheology. (submitted)

[8] **Xi Zhuo Jiang**, Liwei Guo, Kai H. Luo, Yiannis Ventikos. *Flow-Induced Membrane Deformation of Endothelial Glycocalyx Surface: A Molecular Dynamics Study*. (submission in progress)

Conferences

[1] **Xi Zhuo Jiang,** Yiannis Ventios, Kai H. Luo. Large-scale Molecular Dynamics Simulation of Flow and Glycocalyx Interactions. 29th International Conference on Parallel Computational Fluid Dynamics, Glasgow, Scotland, UK, 2017.

[2] Yiannis Ventikos*, Kai H. Luo*, **Xi Zhuo Jiang**. Large-Scale Molecular Dynamics Simulations of Flow and Glycocalyx: Towards Understanding Atomic Events on Endothelial Cell Surface. 68th Annual British Microcirculation Society meeting, April 2018, Nottingham, UK. (invited talk, presenting)

[3] **Xi Zhuo Jiang**, Kai H. Luo*, and Yiannis Ventikos*. Coupled dynamics of blood flow and endothelial glycocalyx: a large-scale molecular dynamics study. The Joint Conference of Three Societies: The European Society for Clinical Hemorheology and Microcirculation, The International Society of Clinical Hemorheology and The International Society of Biorheology(ESCHM-ISCH-ISB-2018), July 2-6, 2018, Krakow, Poland.

[4] **Xi Zhuo Jiang**, John C Vardakis, Yiannis Ventikos*, Kai H. Luo*. Exploring the Dynamics of Endothelial Glycocalyx Under Flow Shear Stress via Large-Scale Molecular Dynamics Simulations. 8th World Congress of Biomechanics, July 8-12, 2018, Dublin, Ireland.